Low-energy nuclear reactions with the radioactive isotope ^{9}Li at REX-ISOLDE

Henrik Bak Jeppesen

Experimental Nuclear Physics Group
Department of Physics and Astronomy
University of Aarhus, Denmark

PhD thesis
August 2004

This thesis has been submitted to the Faculty of Science at the University of Aarhus, Denmark, in order to fulfill the requirements for obtaining the PhD degree in Physics. The studies have been carried out under the supervision of Doctor Karsten Riisager, in the experimental nuclear physics group at the Department of Physics and Astronomy, from August 2000 to August 2004.

2nd edition 1st of September 2004.
This thesis has been typeset in LaTeX 2_ε.

Contents

List of Figures

Preface

This PhD thesis has been submitted to the Faculty of Science at the University of Aarhus in Denmark to fulfill the requirements for the degree of Doctor of Philosophy. During my work on this thesis on experimental nuclear physics I have participated in a large variety of experiments, mostly at ISOLDE (CERN, Switzerland) but also a few at JYFL (Jyväskylä, Finland). During these experiments I have had the pleasure to collaborate with groups from Göteborg, Madrid, Jyväskylä and of course CERN - which is our experimental stronghold. In the first two years of my PhD I worked with beta-dealyed particle emission (especially ^{14}Be) which was used for my Part-A exam (number 6 and 7 in the list of publications).

Since then I have concentrated on low energy reaction with radioactive nuclei. So far three experiments of this kind have been performed at the newly constructed REX-ISOLDE post-accelerator at ISOLDE. The first two experiments were neutron pickup reactions onto ^{9}Li (^{9}Li+^{2}H$\rightarrow^{10}$Li+p and ^{9}Li+^{9}Be $\rightarrow$ ^{10}Li+^{4}He+^{4}He) designed to probe the excited states in the particle unbound nucleus ^{10}Li. The analysis of these experiment has been the main part of my work during the last two years. The third experiment was a resconant elastic scattering experiment of ^{9}Li on protons. The aim of this experiment was to establish the Isobaric Analouge States (IAS) of ^{10}Li in ^{10}Be (resconances in ^{9}Li+p). These three experiments will be the foundation of this thesis.

For completion I will mention that I during my third year as a PhD student stayed 4 month at RIKEN in Tokyo, Japan where I analysed one- and two-neutron removal data for ^{15}O. This resulted in one publication (number 17 in the list of publications). During the stay I also participated in an experiment aimed at measuring the reaction cross-section for ^{17}B and $^{17-18}$C, so far resulting in one publication (number 20 in the list of publications). The work was performed in the group of Isao Tanihata under the supervision of Rituparna Kanungo.

Throughout this thesis several textbooks will be used as reference for general knowledge on nuclear physics. I will not cite the books unless they are used specificly, so here they are [Kra88, Hod97, Hey94].

List of Publications

Publications related to this thesis

1. *Low energy reactions with radioactive ions at REX-ISOLDE - the ^{9}Li+d case.*
   H. Jeppesen, F. Ames, P. van den Bergh, U.C. Bergmann, G. Bollen, M.J.G. Borge, J. Cederkäll, P. van Duppen, S. Emhofer, O. Forstner, L.M. Fraile, H.O.U. Fynbo, D. Habs, R. von Hahn, G. Huber, M. Huyse, H.T. Johansson, B. Jonson, O. Kester, H. Lenske, L. Liljeby, M. Meister, T. Nilsson, G. Nyman, M. Onionen, M. Pantea, H. Podlech, U. Ratzinger, K. Reisinger, K.G. Rensfelt, R. Repnow, K. Riisager, A. Richter, K. Rudolph, H. Scheit, A. Schempp, P. Schmidt, G. Schrieder, D. Schwalm, T. Siebert, H. Simon, O. Tengblad, E. Tengborn, M. Turrión, L. Weissmann, F. Wenander, B. Wolf and the ISOLDE and REX-ISOLDE collaborations. In preparation.

2. *Experimental investigation of the ^{9}Li+d reaction at REX-ISOLDE*
   H. Jeppesen, F. Ames, U.C. Bergmann, M.J.G. Borge, J. Cederkäll, S. Emhofer, L.M. Fraile, H.O.U. Fynbo, S. Henry, H.T. Johansson, B. Jonson, M. Meister, T. Nilsson, G. Nyman, M. Pantea, K. Riisager, A. Richter, K. Rudolph, G. Schrieder, T. Siebert, O. Tengblad, E. Tengborn, M. Turrión, R. von Hahn, F. Wenander, B. Wolf, the ISOLDE and REX-ISOLDE collaborations.(Cluster´03 conference 2003), Nucl. Phys. **A738** (2004) 511.

3. *The ^{9}Li+d reaction at REX-ISOLDE*
   H. Jeppesen for the ISOLDE and REX-ISOLDE collaborations, (NENS03 conference 2003) submitted to World Scientific Publication Company.

Other publications

4. *Analysis of decay data from neutron-rich nuclei*
U.C. Bergmann, M.J.G. Borge, J. Cederkäll, C. Forssén, E. Fumero, H.O.U. Fynbo, H. Gausemel, **H. Jeppesen**, B. Jonson, K. Markenroth, T. Nilsson, G. Nyman, K. Riisager, H. Simon, O. Tengblad, L. Weissman, F. Wenander, K. Wilhelmsen Rolander and the ISOLDE collaboration, Phys. J. **A11** (2001) 279.

5. *Correlated emission of three alpha-particles in the beta-decay of* ^{12}N,
H.O.U. Fynbo, Y. Prezado, J. Äysto, U.C. Bergmann, M.J.G. Borge, P. Dendooven, W.X. Huang, J. Huikari, **H. Jeppesen**, P. Jones, B. Jonson, M. Meister , G. Nyman, M. Oinonen, K. Riisager, O. Tengblad, I.S. Vogelius, Y. Wang, L. Weissman and K.W. Rolander (ENAM conference 2001), Eur. Phys. J. **A15** (2002) 135.

6. *Search for beta-delayed charged particles from the halo nucleus* ^{14}Be
H. Jeppesen, U.C. Bergmann, M.J.G. Borge, J. Cederkäll, V.N. Fedoseyev, H.O.U. Fynbo, V.Y. Hansper, B. Jonson, K. Markenroth, V.I. Mishin, T. Nilsson, G. Nyman, K. Riisager, O. Tengblad, K. Wilhelmsen Rolander and the ISOLDE collaboration, Nucl. Phys. **A709** (2002) 119.

7. *News on beta delayed particle emission from* ^{14}Be,
H. Jeppesen, U.C. Bergmann, M.J.G. Borge, J. Cederkäll, V.N. Fedoseyev, H.O.U. Fynbo, V.Y. Hansper, B. Jonson, K. Markenroth, V.I. Mishin, T. Nilsson, G. Nyman, K. Riisager, O. Tengblad, K. Wilhelmsen Rolander and the ISOLDE collaboration, (YKIS01 conference 2001) Prog. Theor. Phys. Supp. **146** (2002) 520.

8. *New information on alpha-cluster states in* ^{12}C *from the beta-decay of* ^{12}N,
H.O.U. Fynbo, **H. Jeppesen**, K. Riisager, I. Storgaard Vogelius, Y. Prezado, M.J.G. Borge, O. Tengblad, P. Dendooven, W. Huang, J. Huikari, P. Jones, Y. Wang. J. Äysto, B. Jonson, M. Meister, G. Nyman, U.C. Bergmann, L. Weissman and K. Wilhelmsen Rolander, (Post-symposium of YKIS01 2001) Nucl. Phys. **A718** (2003) 541c.

9. *Beta-decay in the A=9 isobar*,
O. Tengblad, U.C. Bergmann, M.J.G. Borge, R. Boutami, J. Cederkäll, L.M. Fraile, H.O.U. Fynbo, **H. Jeppesen**, B. Jonson, K. Markenroth, T. Nilsson, G. Nyman, Y. Prezado, K. Riisager, F. Wenander, K. Wilhelmsen Rolander and the ISOLDE collaboration, (ENAM conference 2001)

Proceedings of the Third International Conference on Exotic Nuclei and Atomic Masses ENAM 2001, Springer (2003) 142.

10. *Decay characteristics of neutron-rich nuclei - new results for* ^{14}*Be*, U.C. Bergmann, M.J.G. Borge, J. Cederkäll, H.O.U. Fynbo, **H. Jeppesen**, B. Jonson, K. Markenroth, T. Nilsson, G. Nyman, K. Riisager, H. Simon, O. Tengblad, K. Wilhelmsen Rolander and the ISOLDE collaboration, (ENAM conference 2001) Proceedings of the Third International Conference on Exotic Nuclei and Atomic Masses ENAM 2001, Springer (2003) 223.

11. *Beta-decay properties of the neutron-rich* $^{94-99}$*Kr and* $^{142-147}$*Xe isotopes* U.C. Bergmann , C.Aa. Diget, K. Riisager, L. Weissman, G. Auböck, J. Cederkäll, L.M. Fraile, H.O.U. Fynbo, H. Gausemel, **H. Jeppesen**, U. Köster, K.-L. Kratz, P. Möller, T. Nilsson, B. Pfeiffer, H. Simon, K. Van de Vel, J Äysto and the ISOLDE collaboration, Nucl Phys. **A714** (2003) 21.

12. *Production yields of noble-gas isotopes from ISOLDE UCx/graphite targets*, U.C. Bergmann , G. Auböck, R. Catherall, J. Cederkäll, C.Aa. Diget, L.M. Fraile, S. Franchoo, H.O.U. Fynbo, H. Gausemel, U. Georg, T. Giles, **H. Jeppesen**, O.C. Jonsson, U. Köster, J. Lettry, T. Nilsson, K. Peräjärvi, H. Ravn, K. Riisager, L. Weissman, J Äysto and the ISOLDE collaboration, (EMIS conference 2002) NIM **B204** (2003) 220.

13. *Beta decay of* $^{49-50}$*Ar* L. Weissman, U.C. Bergmann , J. Cederkäll, L.M. Fraile, S. Franchoo H.O.U. Fynbo, H. Gausemel, **H. Jeppesen**, U. Köster, K.-L. Kratz, T. Nilsson, B. Pfeiffer, K. Van de Vel, J. Äysto and the ISOLDE collaboration, Phys. Rev. **C67** (2003) 54314-1.

14. *New information on* ^{12}*C from the beta-decays of* ^{12}*N and* ^{12}*B*, H.O.U. Fynbo, U.C. Bergmann, M.J.G. Borge, P. Dendooven, C.Aa. Diget, W.X. Huang, J. Huikari, **H. Jeppesen**, P. Jones, B. Jonson, M. Meister , G. Nyman, Y. Prezado, K. Riisager, I. Storgaard Vogelius, O. Tengblad, Y. Wang, L. Weissman, K. Wilhelmsen Rolander and J. Äysto, (7th Nuclei in the Cosmos conference 2002) Nucl. Phys. **A718** (2003) 541.

15. *Clarification of the threebody decay of* ^{12}*C(12.71 MeV)* H.O.U. Fynbo, Y. Prezado, U.C. Bergmann, M.J.G. Borge, P. Dendooven, W.X. Huang, J. Huikari, **H. Jeppesen**, P. Jones, B. Jonson, M. Meister , G.

Nyman, K. Riisager, O. Tengblad, I.S. Vogelius, Y. Wang, L. Weissman, K. Wilhelmsen Rolander and J. Äysto, Phys. Rev. Lett. **91** (2003) 82502-1.

16. *Largest asymmetry in the strongest beta-transition for A=9*
Y. Prezado, U.C. Bergmann, M.J.G. Borge, J. Cederkäll, C. Aa. Diget, L.M. Fraile, H.O.U. Fynbo, **H. Jeppesen**, B. Jonson, M. Meister , T. Nilsson, G. Nyman, K. Riisager, O. Tengblad, L. Weissman, K. Wilhelmsen Rolander and the ISOLDE collaboration, Phys. Lett. **B576** (2003) 55.

17. *One- and two-proton removal from* ^{15}O
H. Jeppesen, R. Kanungo, B. Abu-Ibrahim, S. Adhikari, M. Chiba, D. Fang, N. Iwasa, K. Kimura, K. Maeda, S. Nishimura, T. Ohnishi, A. Osawa, C. Samanta, T. Suda, T. Suzuki, I. Tanihata, Q. Wang, C. Wu, Y. Yamaguchi, K. Yamada, A. Yoshida and T. Zheng, Nucl. Phys. **A739** (2004) 57.

18. *Asymmetry in the super-allowed beta-transition of the A=9*
M.J.G. Borge, Y. Prezado, U.C. Bergmann, R. Boutami, J. Cederkäll, C. Aa. Diget, L.M. Fraile, H.O.U. Fynbo, Y. Jading, **H. Jeppesen**, B. Jonson, I. Martel, M. Meister , T. Nilsson, G. Nyman, K. Riisager, H. Simon, O. Tengblad, L. Weissman, F. Wenander, K. Wilhelmsen Rolander and the ISOLDE collaboration, (Cluster´03 conference 2003) Nucl. Phys. **A738** (2004) 206.

19. *News on 12C from beta-decay studies*
H.O.U. Fynbo,C. Aa. Diget, Y. Prezado, J. Äysto, U.C. Bergmann, J. Cederkäll,P. Dendooven, L.M. Fraile, S. Franchoo, B.R. Fulton, W. Huang, J. Huikari, **H. Jeppesen**, A. Jokinen, B. Jonson, P. Jones, U. Köster, M. Meister, T. Nilsson G. Nyman, M.J.G. Borge, K. Riisager, S. Rinta-Antila, I. Storgaard Vogelius, O. Tengblad, M. Turrión, Y. Wang, L. Weissman, K. Wilhelmsen and the ISOLDE collaboration, (Cluster´03 conference 2003) Nucl. Phys. **A328** (2004) 59.

20. *Halo structure of* ^{17}B *studied via its reaction cross section*
Y. Yamaguchi, C. Wu, D.Q. Fang, M. Fukuda, N. Iwasa, T. Izumikawa, **H. Jeppesen**, R. Kanungo, R. Koyama, T. Ohnishi, T. Othsubo, A. Ozawa, W. Shinozaki, T. Suda, T. Suzuki, M. Takahashi, I. Tanihata and S. Watanabe, (NENS03 conference 2003) submitted to World Scientific Publication Company.

CHAPTER 1

Introduction

In this chapter I will motivate why we still do nuclear physics in an era where many scientists think that nuclear physics is a solved problem.
Then I will breifly review the topics of modern nuclear physics.

1.1 Introduction

The atomic nucleus was discovered almost a hundred years ago by Geiger and Marsden (1909) when they irradiated gold and silver foils by alpha-particles from a radioactive source and observed many back scattered alpha-particles which led Rutherford (1911) to postulate that the atomic nucleus was very small and dense and not a dilute gas as believed before. This discovery paved the way, at least partly, for Bohrs model for the hydrogen atom (1913) and further on to the development of quantum mechanics.

During the following years the atomic nucleus was studied extensively through low energy reactions starting with Rutherford (1919) making the first nuclear reaction (^{4}He+^{14}N$\rightarrow ^1$H+^{17}O) with alpha-particles from radioactive decay. Many people followed in the footsteps of Rutherford and used particles from radioactive decay to study nuclei until Cockcroft and Walton invented the electrostatic accelerator. This started a race for higher and higher reaction energies which is still running at full pace (eg LHC at CERN). In 1932 Chadwick solved the puzzle about the constituents in the atomic nucleus when he discovered the neutron and thereby removed the problem of having electrons present inside the atomic nucleus.

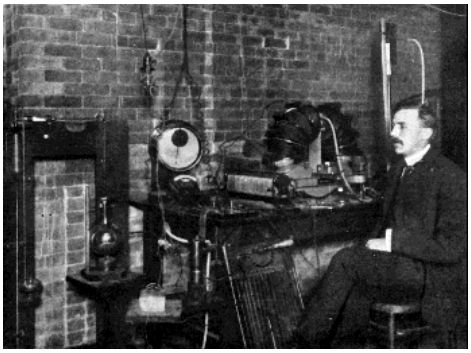

FIGURE 1.1: Photograph of Ernest Rutherford in his laboratory around 1911.

With these progresses in nuclear physics the constituents, protons and neutrons, were found and a more firm theory could be developed on the framework of quantum mechanics. The first application of quantum mechanics to nuclear physics was when Gamow in 1928 explained the very different half-lifes observed in alpha-decay by quantum mechanical tunneling effects. One great challenge of nuclear physics is the poor knowledge of the nuclear potential with which the nucleons interact. The problem with the nuclear force is its great complexity, that is, it falls off very fast, is very attractive at a shorter range (within a few fm) but has a repulsive core. Many attempts to describe the nuclear force has been tried but they all lack the simplicity that would make them applicable in realistic many nucleon calculations.

One of the most successful models is the shell-model which beautifully describes the magic numbers and opens a possibility for making approximate cal-

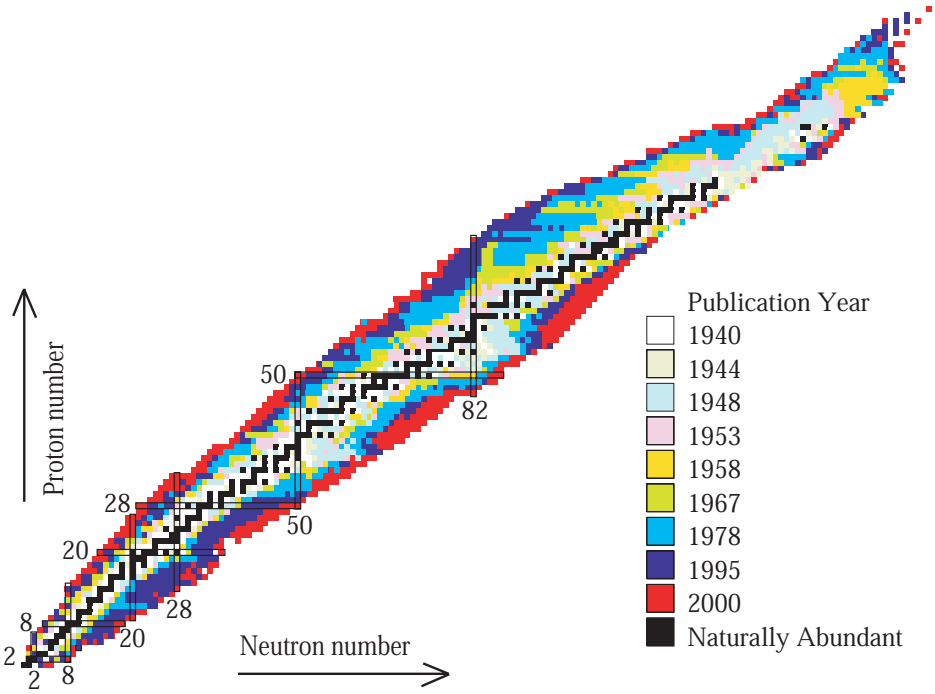

FIGURE 1.2: Historic nuclear chart with color indications of year of discovery. Note the many nuclei discovered since 1978.

culations by leaving closed shells as inert when making calculations and hence reducing the complexity of the calculations considerably. For a short and very nice review on the historical development of nuclear physics see Bethe [Bet99].

The work of all of these men and women, founders of nuclear physics, was due to technical incapability forced to settle with only studying the nuclei close to the valley of stability. Today that technical knowledge is at our hands and leaves us with no choice than to explore the unknown and unstable.

1.2 Nuclear physics far from stability

The massive work done on nuclear physics in the 1950s, 60s and 70s was mainly focused on nuclei close to stability, due to the limited ability to produce unstable nuclei. Thus the knowledge on nuclear physics extracted in that period was mostly based on the about 300 stable nuclei (compare to the about 6000 nuclei that has been predicted by theory to be particle bound). This knowledge was in the 80s found to be incomplete when it became possible to study unstable nuclei

at facilities such as ISOLDE at CERN, RIKEN in Japan, MSU in USA, GANIL in France and several other places. One of the first discoveries that changed the traditional view of nuclear physics was that of a neutron halo structure observed by Tanihata *et al* in ^{6,8}He [Tan85a] and ^{11}Li [Tan85b].

To explore nuclei further and further away from stability is not an easy task and demands an ongoing development of production and detection techniques. The evolution of the nuclear chart is shown in figure 1.2 where the development from about 800 isotopes in the 40s to about 3000 isotopes today is visualized. Within the last 20 years about 1/3 of all known isotopes has been discovered and hence the basis for extending nuclear theories to unstable nuclei has been greatly improved.

When investigating nuclei far from stability one meets the problems of low production yield and very short half life (down to a few ms at ISOLDE) thus the time between production and measurement has to be very short.

1.3 Modern nuclear physics

The world of today is a place where scientists are constantly asked if their research is relevant and can benefit society. Nuclear physics is not an exception to this rule which is clearly seen in the many different ways in which nuclear physics is used in every day life - though it may not always be visible (just think of how NMR became MR to get rid of the word *Nuclear*). I will here try briefly to list a few of the fields in which nuclear physics is still alive and kicking:

1.3.1 Nuclear structure physics

Today nuclear structure physics is concentrated on the nuclei far from stability where many new phenomena have been discovered during the last two decades, although well known nuclei such as ^{12}C are still being investigated (eg work on the three-alpha particles states above the Hoyle state [Fyn03]). One of the new phenomena in nuclear structure discovered within the last 10 years is the changing, or vanishing, of magic numbers which has been confirmed for the N=20 to N=16 case [Kan02]. Many of these new structures discovered have puzzled the nuclear physics society and forced the scientists to rethink many old assumptions.

The light nuclei have been specially interesting since the driplines can be reached on both sides whereas it is very difficult to reach the neutron dripline for heavier nuclei. Furthermore the light nuclei are less complicated and can at the moment be treated in *ab initio* Quantum Monte Carlo Calculations [Pie01] with

realistic models of the nuclear forces (A=9,10 see [Pie02]) making comparison between theory and experiment very fruitful. A review on the investigation of light dripline nuclei has recently been written [Jon04].

The many new facilities being built or proposed at the moment is a clear sign that nuclear structure physics is an expanding field and indicates that it might regain some of its lost glory.

1.3.2 Nuclear astro-physics

All nuclei, surrounding and inside of us, are created somewhere in the universe and most of these through the nuclear synthesis which connects astrophysics to nuclear physics.

According to the Big Bang model the first nuclei where created only 3 minutes after the Big Bang and at that time the early universe was composed of about 3/4 of ^{1}H and 1/4 of ^{4}He and minute amounts of a few other light nuclei. After another 200 million years (according to new measurements from WMAP [Wmap]) stars start to form by gravitational collapse of huge gas clouds containing H and He. Through the collapse the cloud heats up and eventually the temperature is high enough for nuclear burning to set in. In this nuclear fusion process H is first burned to He and, if the star is massive enough, the He is then burned to heavier nuclei. This repetitive process continues, if the star is massive enough, until the burning reaches Ni ($A \simeq 60$) which has the largest binding energy per nucleon and thus fusion is no longer energetically favorable.

The elements heavier than $A \simeq 60$ are formed by bombarding the $A \simeq 60$ nuclei by a neutron flux. This process is a balance between neutron capture and beta-decay but it eventually leads to heavier nuclei. There are two scenarios for this process either the s-process (s for slow) where the neutron flux is moderate and thus all the nuclei along the path are very close to stability, or the r-process (r for rapid) where the neutron flux is high and the path lies far from stability. The r-process requires a very high neutron flux and most likely takes place in super novae explosions which can occur when an old star dies.

To be able to reproduce the abundance of nuclei in the universe, as it is observed today, it is crucial to know many different properties, such as cross-sections, half-lifes, decay channels etc, for a great variety of nuclei.

Today, many people are trying to measure the properties for the nuclei involved in the r-process but unfortunately many of these nuclei are very far from stability and beyond our reach today. Many of these still unknown nuclei will be possible to produce in the near future at the next generation of facilities producing radioactive isotopes.

For more information on nuclear astro-physics see for example parts of these two standard textbooks [Hod97,Kra88] on nuclear physics and references therein.

1.3.3 Nuclear medicine

Diagnostics: The field of nuclear physics was almost born together with the application of X-ray imaging by the work of Röntgen in the late 19th century. X-ray imaging is possible since X-rays interact stronger with heavier nuclei and thus have a shorter range in bones (made mostly of Ca) than in tissue (mainly composed of H, C and O). Today X-ray imaging is an indispensable tool for doctors and dentists in their daily work in locating fractures and finding holes in teeth, respectively. Taking X-ray images from different angles makes it possible to generate 3-D imaging of the harder parts of the human interior via **C**omputerized **A**xial **T**omography (CT or CAT scanning).

When trying to look at the softer parts of the human interior X-rays are obviously not a good idea since soft tissue has more or less the same nuclear composition. One way of overcoming this problem is by the so-called tracer method. In this method one places a radioactive isotope in an organic molecule which binds to or is collected in the kind of tissue on which information is needed. When the radioactive isotope reaches the area of interest the host molecule is trapped and like wise the radioactive isotopes which can then be seen by gamma-cameras. A more precise variant is that of **P**ositron **E**mission **T**omography (PET) which uses radioactive isotopes that decays by emitting positrons (beta-plus decay). The positron then annihilates with one of the nearby electrons and emits two 511 keV gamma-rays which are then detected in coincidence. Another way to access information on the structure of the softer tissue in the human body is to use **N**uclear **M**agnetic **R**esconance (NMR or MR) which basically measures the relaxation time of the proton spin after is has been perturbed. The essence is that the relaxation time is dependent on the molecule or surrounding in which the hydrogen nucleus is situated, thus exhibiting contrast between water, muscles, brain tissue etc. The NMR technique has the advantage, compared to tracer methods and CAT scanning, that it produces

FIGURE 1.3: One of the first X-ray images taken in the late 1800 by W. Röntgen of his wifes hand.

images with more contrast, better resolution and give a complete image of the region, where tracer methods only shows the area where the tracer is present.

Treatment: Cancer therapy is by far the largest field in decease treatment where nuclear physics is applied and a very important one since one million people in the EU alone is diagnosed with cancer every year. Treatment is done by irradiating the tumor with either gamma-rays or ions and thereby destroying the DNA of the cancer cells. Using gamma-rays is today the most widespread method to treat cancer since they are easily produced as bremsstrahlung when high energy electrons are stopped in a thick target. Unfortunately photons have a very flat depth-to-dose profile, that is the energy deposited per length only varies slowly with the deposition depth, and deposits the same dose within a factor of two over a range of 20 cm. This problem could be overcome by irradiating the tumor with ions, protons in most cases, whose depth-to-dose profile grows with the implantation depth up to a maximum situated at the average range of the proton (Bragg peak) and has an increased **R**adio **B**iological **E**fficiency (RBE).

In recent years cancer therapy with heavier ions (^{12}C) has been developed and is now being used on humans two places in the world (GSI, Germany and Chiba, Japan). ^{12}C is used since it is the optimum ion for killing most cells in the tumor and least in the healthy tissue surrounding the tumor. Furthermore irradiating tumors with ^{12}C has the advantage that nuclear reactions take place when the beam is implanted in the patient and lighter carbon isotopes, like ^{11}C and ^{10}C, are produced. These carbon isotopes decay via beta-plus decay and hence the dose deposition can be monitored on-line via PET. Furthermore the idea of using radioactive isotopes for cancer therapy has been discussed since the subsequent decay of the ion would add extra “killing power” to the tumor. For more information on cancer therapy with heavy ions see the nice review on the work done at GSI in Germany by G. Kraft [Kra00].

Another method for cancer treatment has been investigated, eg at ISOLDE at CERN, where a radioactive alpha-emitter is attached to an organic molecule which binds to the tumor. When the radioactive isotope arrives at the tumor the idea is that the ionizing radiation kills the cancer cells while the surrounding tissue is left undamaged. This method has been tested on mice and shows very promising results [Bey00].

Research: Many of the methods mentioned above are not only used for diagnostics or treatment since many of them can be utilized to gain basic knowledge about how the human body functions. As an example brain science could be mentioned where researchers monitor the blood flows or energy consumption in the brain, with eg PET or NMR, when a subject is exposed to a sense impression.

1.3.4 Nuclear energy production and waste management

This field is of course well known, hated or loved, and one that must be taken seriously if our blue planet is to survive in the long run. Especially with the third world closing in on the industrialized countries the amounts of fossil fuels will probably not last very long and our environment will most probably suffer very severely (eg the green house effect). In this perspective nuclear power production must be looked at as an alternative at least for a limited period until possible renewable energy sources can support the majority of the earths energy consumption.

Today only nuclear fission is used for energy production in reactors where uranium and plutonium is made to fission by neutron bombardment, arising as product of the fission, thus making the process "self-fueling" when a sufficient neutron flux is obtained. This unfortunately holds the possibility of nuclear runaway processes which results in a total destruction of the power-plant and a huge radioactive pollution of a large area (think of Chernobyl which was not a nuclear melt-down but still had a great impact). Thus reactors without this dangerous feature must be developed, in my perspective, if nuclear power is to be allowed by the public as a major energy source.

Radioactive waste management is also a problem to be addressed if nuclear power is to deliver a major part of our energy consumption. So far this has been done simply by storing the nuclear waste in old mines etc. A novel technique called **A**ccelerator **D**riven **T**ransmutation (ADT) where the long-lived waste is transmuted, by a neutron flux created by an accelerator, into more neutron rich isotopes with a shorter half-life has been proposed. An obvious advantage of this method is the reduction of nuclear waste but it also produces additional energy though less profitable than the conventional reactor. In this method the nuclear burning is said to done sub critically since an exterior neutron flux is necessary to sustain the nuclear burning process and therefore is very unlikely to cause a nuclear melt-down.

If nuclear power is to be the solution for the worlds energy demands we cannot rely on fission energy alone but must turn to fusion where two light nuclei[1] fuse to produce energy (similar to the processes that fuels the stars). Realizing nuclear fusion in a profitable way has turned out not to be very easy since the energies needed to bring two charged particles close enough to fuse is very high to reach thermally (1 MeV/A correspond to 7.7×10^9 K). For the last 25 years the **J**oined **E**uropean **T**orus project (JET) has been trying to achieve this goal by confining the hot plasma with a magnetic field. The JET collabora-

[1] Lighter than iron which has the highest binding energy per nucleon.

tion managed a few years ago to create more energy by fusion than they used to make it, thus producing energy by nuclear fusion. A new fusion reactor is currently being designed by the international collaboration ITER [ITER] (ITER meaning "the way" in Latin) using magnetic confinement as JET. Nuclear fusion could also be achieved by use high energy heavy ion beams or very intense laser beams to compress a small capsule, containing the the nuclear fuel, causing it to heat dramatically and thereby starting the fusion process. This method is called **I**nertial **C**onfinement **F**usion (ICF). Two facilities are currently being built in France and USA using laser beams to obtain ICF. Laser driven ICF is probably best suited for research whereas accelerator driven ICF most likely will be used if ICF should be implemented in a commercial fusion reactor. Hopefully these new reactors will be the last experimental reactor before nuclear fusion can be utilized commercially to cover the energy shortage in the world. Unfortunately this will probably still take another 50 years!

Apart from the subjects mentioned above many others exists within the realm of modern nuclear physics, eg the search for super heavy nuclei[2], solid state physics, radiocarbon dating, material analysis by neutron scattering and the search for physics beyond the standard model. Much more on these, and other, applications of modern nuclear physics is to be found in a recent NuPEEC report on nuclear science in Europe [NuP02].

1.4 Probing nuclear structure

When trying to extract information on nuclear structure it is of course necessary to have a probe which is sensitive on the appropriate scale which in the case of nuclear physics is on the order of fm, ie 1×10^{-15} m. Obviously visible light is useless, with wavelengths on the order of hundred million fm, and one must look for particles with much higher energy to reach these small scales. The energy scale for nuclear physics is the MeV range where both gamma-rays, leptons and hadrons can participate.

The most successful probes for extracting information on nuclear structure is without doubt performing nuclear reactions by colliding two nuclei (or one nucleus and another particle).

[2] Element 115 has just been discovered this year [Oga04]

1.4.1 Nuclear reactions

As mentioned earlier the first nuclear reactions made in the start of the 20th century was performed with very low energy particles; around 1 MeV/A. After the Second World War larger accelerators were built around the world, mainly in America, which could reach energies of up to 10s of MeV/A. With these beams it became possible to extract structure information about the produced nuclei by detecting and identifying the reaction products. This led to a boom in knowledge on the nuclei close to the line of stability in the 50s and 60s.

Today most nuclear reaction facilities use beam of much higher energies (from 100 MeV/A and up to a few GeV/A) and are more focused on making reactions with secondary beams of exotic nuclei produced by the primary beam of stable nuclei (see section 3.2.1 for this production method). These secondary beams of fast (more or less the same energy as the primary beam) exotic nuclei can then be brought to react with stable nuclei within μs of production. These type of reactions, performed at GSI, RIKEN, MSU, GANIL and other places, aim in many cases to study the nuclear structure via prompt reaction mechanisms. Apart from nuclear structure information the distribution of nuclear matter can also be probed via high energy reactions, eg via momentum distribution of valence nucleons (see eg [Jep04] for an example of the method). The combination of nuclear radius and valence nucleon momentum distribution have in most cases been used to establish the halo nuclei known today.

At the other end of the energy scale facilities such as REX-ISOLDE (0.8 to 3.1 MeV/u) make reactions just above the Coulomb barrier or Coulomb excitations of heavier nuclei. When performing low energy reactions close to the Coulomb barrier the reaction mechanism and overlap between states in the incoming and outgoing channels becomes the determining factor for which outgoing channels will be fed. This selective feeding in low energy reaction may be viewed as a blessing of course depending on which type of reaction and physical information one wish to address.

For radioactive nuclei it is also possible to probe the structure of the nucleus by observing the decay products. The most common decay type for the short lived nuclei, which are presently being produced at facilities around the world, is that of beta decay.

1.4.2 Beta decay

Most of the previous work in the nuclear experimental group in Århus has been done using beta decay as a probe to access nuclear structure information.

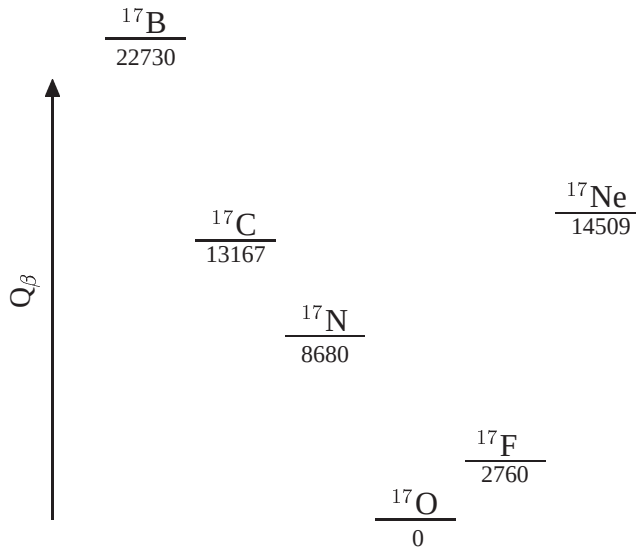

FIGURE 1.4: Graphical representation of Q_β values for the A=17 isobar. The Q_β values is written in keV.

Going further away from stability beta decay becomes an increasingly better probe of nuclear structure since the energy released in the decay in general increase very much. This is shown in figure 1.4 where one can see that a nucleus as ^{17}B release more than 22 MeV in a beta decay. With avarage nucleon binding energies of $\sim$ 8 MeV (smaller near the driplines) these high Q_β values allows for beta-delayed particle emision which is a very sensitive tool to extract nuclear structure information (see eg [Jon96]). In figure 1.5 is shown the possible beta-delayed particle emitters in the N,Z$\leq$50 nuclei. It is evident from figure 1.5 that one could expect beta-delayed emission of many different particles when getting close to the driplines. Many of the beta-delayed channels suggested in figure 1.5 have been observed experimentally.

Especially in halo nuclei beta-delayed particle emission could give very clear information on the structure of the halo. If the very simple approximation of a halo as composed of a core plus a halo part holds the beta decay of such a state would be the same as the combined decay of the core and halo (for more on this simple model see [Nil00]). So in the case of two-neutron halos a beta-delayed deuteron would give evidence of this cluster picture. For an example see [Jep02] on the search for beta-delayed particles from ^{14}Be.

The advantage of beta decay compared to reactions is that the decay mecha-

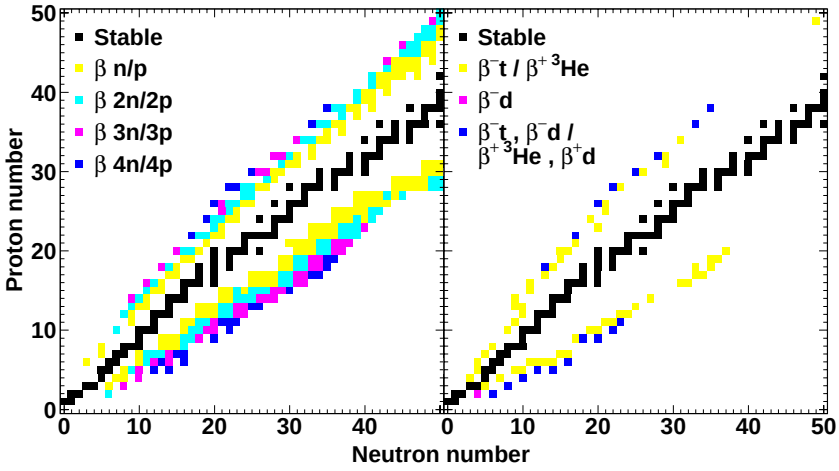

FIGURE 1.5: Energetically possible beta-delayed particle emission from N,Z$\leq$50. Adapted from [Ber00].

nism is well understood and that decay selection rules may favour specific channels, making the spectra simpler. Furthermore due to the fact that all unstable isotopes will decay, these experiments can be performed with much smaller yields (less than 1 ion per second at setup is feasible) compared to reaction experiments wich normally require on the order of 100 ions per second or more (depending very much on the specific reaction experiment).

For more on beta-decay as a probe for exotic nuclei see the review by Jonson and Riisager [Jon01].

Due to the different methods of producing the isotopes at different facilities yields naturally vary significantly and thus different facillities/methods have certain isotopes on which they excel.

In general one might say that reaction experiments are neither better nor worse than decay experiments, but that they acces nuclear structure in different ways and thus compliment each other to give a consistent and full understanding of nuclear physics.

CHAPTER 2

Nuclear structure and reactions

In this chapter I will review the some aspects of nuclear structure, especially the shell model.
Then an overview of different reaction mechanisms will be presented.
Finally I will in more detail discuss the possibilities of probing nuclear structure via low energy reactions via single- or few-nucleon transfer reaction.

2.1 Introduction

Nuclear reactions are, as mentioned earlier, the most used probe in nuclear physics, and also the one that has been used in the three experiments that I will describe in this thesis. Since nuclear reactions can occur in many different ways I will in this chapter try to outline the different types and the mechanisms with which they occur. I will concentrate on some cases which are of special interest to this thesis.

Before plunging into nuclear reactions it would be appropriate to refresh a few of the nuclear properties which will be of relevance later. Due to the fact that the nuclear force is very short ranged (only a few fm) and is very repulsive at short ranges (less than a fm) the nucleus must have a size in the fm range since nucleons cannot be separated by more than a few fm but nor can it condense into a point-like particle. This can be visualized as packing marbles in a spherical bag, and result in a simple behavior of the nuclear radius

$$r \simeq aA^{1/3}, \tag{2.1}$$

where A is the mass number of the nucleus and a is a constant close to 1 fm. Though this is only an approximation for the nuclear radius it is fairly good for stable nuclei with A>20. For stable nuclei the distribution of neutrons and protons are almost similar and the value of a is $\sim$1.2 fm for RMS radii. For radioactive nuclei the distribution of protons and neutrons and thus their radius can differ significantly (op to about 0.5 fm) and may be larger than that for a stable nucleus with same A. Examples of the difference in neutron and proton radius, which have been observed experimentally, are; neutron skin in neutron rich nuclei where the neutron density distribution has a larger RMS radius than the proton density distribution, or neutron halo where the neutron distribution has a long tail which extends out into the classically forbidden region. Furthermore the surface of a nucleus is not a sharp edge but it drops relatively slowly from the inner density to zero over about 2 fm (90 % density to 10 %). For a review on nuclear sizes of unstable nuclei see [Oza01].

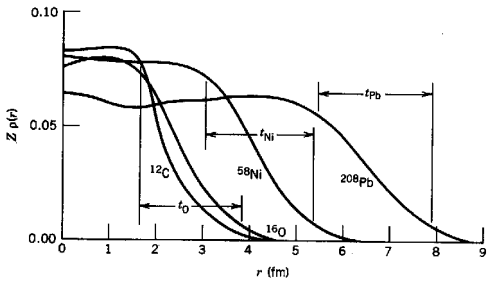

FIGURE 2.1: Examples of radial nuclear charge distributions which illustrates the constant bulk density and the surface behavior. From [Kra88].

2.1.1 Nuclear models

An interesting property of the nucleus is that it exhibits both collective and single particle behavior and thus constructing nuclear models presents a great challenge. For the collective behavior models such as the liquid drop model have been developed and are very suitable for describing rotational and vibrational spectra. Whereas the single particle model reproduce such properties as magic numbers and spin assignment of excited and ground states.

I will now concentrate on the shell model - a single particle model - that have had a very large impact on nuclear physics since it was developed in the late 40's (J.H.D Jensen and M.G. Mayer received the Noble prize in 1963 for developing the shell model and explaining the magic numbers).

The nuclear shell model is in many ways similar to the atomic model in that they both basically are made on the assumption that the particles (nucleons or electrons) move around in a radial symmetric potential and they both exhibit magic numbers or closed shells.

The differences between the atomic and nuclear shell model is that the electrons move in a external field provided by the atomic nucleus and that the "electron gas" surrounding the nucleus is very dilute. In the nuclear case it is the interaction between the nucleons themselves that provides the mean-field in which the nucleons move around and the nuclear density is by no means dilute.

The simplest shell model is obtained by using an infinite well or harmonic oscillator (HO) potential which are easily tractable when solving the Schrödinger equation but not very realistic since they both grow to infinity at large distances hence making the binding energy infinite. A more realistic nuclear potential, which is a mean-field potential and shows the right fall off of the nuclear interaction at large distances, could be the Woods-Saxon potential

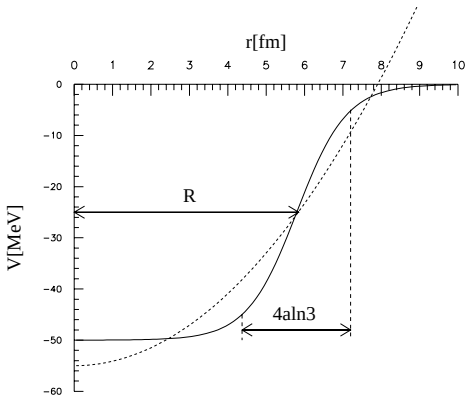

FIGURE 2.2: Realistic nuclear potentials; Woods-Saxon (solid) with radius and skin thickness indicated and the harmonic oscillator (dashed). Note that the HO grows to infinity!

$$V(r) = \frac{-V_0}{1 + \exp\left[(r - R)/a\right]},$$

where V_0 is the strength, R is the radius and a is a parameter for the skin thickness of the potential (see figure 2.2). Even though the Woods-Saxon potential is more realistic it still does not reproduce the magic numbers; N or

Z=2,8,20,28,50,84 but returns the numbers N or Z=2,8,20,40,70,112.

The crucial feature that is missing in this first shell model is a strong spin-orbit coupling between the angular momentum and intrinsic spin of the nucleons. The basic assumption in the strong spin-orbit coupling is that the state in which the angular momentum and intrinsic spin couples parallel ($j = l + 1/2$) has considerably lower energy than the anti-parallel coupling ($j = l - 1/2$). This energy splitting is proportional to the angular momentum l and thus states with high angular momentum can be affected so much as to lower the state with maximum total angular momentum j in a "closed shell" into the "closed shell" just below. This lowering of the shell with highest j is just what is needed to reproduce the magic numbers as discovered independently by the group of H.J.D. Jensen and M.G. Mayer [Hax49, May49]. In figure 2.3 the level diagram for protons is shown calculated with a Woods-Saxon potential and spin-orbit coupling. Note how the lowest shell in the HO closed shells for the heavier systems are lowered into the HO closed shell below. For neutrons a very similar level diagram arise. Due to the Coulomb interaction between protons small changes do occur for example the $1g_{7/2}$ and $2d_{5/2}$ are interchanged for neutrons but the magic numbers persists.

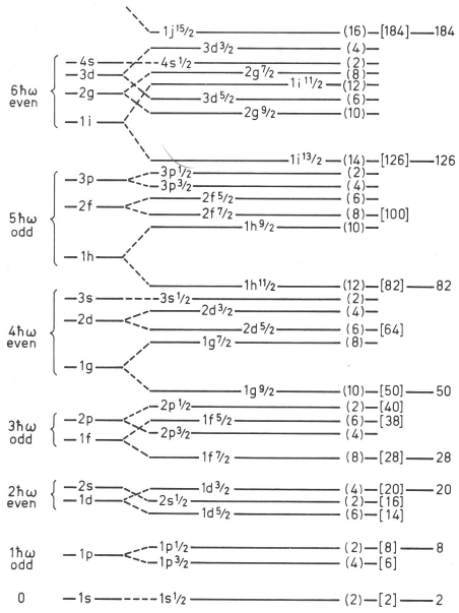

FIGURE 2.3: Level diagram for protons using a realistic potential with spin-orbit interaction. Taken from [May55]

Unfortunately nuclear modeling is not as simple as just to follow the diagram in figure 2.3 and calculations of the level spacing have been performed for varying mass number A. One such calculation for stable nuclei performed by C.J. Veje is shown in figure 2.4 where a Woods-Saxon potential including spin-orbit was used (for more on potential dependencies on A see [Boh69]). In figure 2.4 one sees that the level diagram from figure 2.3 is not absolute since the levels do cross with varying mass number. What is very interesting from figure 2.4 is the fact that the $1d_{3/2}$ and $2s_{1/2}$ are suggested to interchange for light nuclei thus changing the magic number from 20 to 16 which is precisely what has been seen experimentally for light neutron rich nuclei [Kan02].

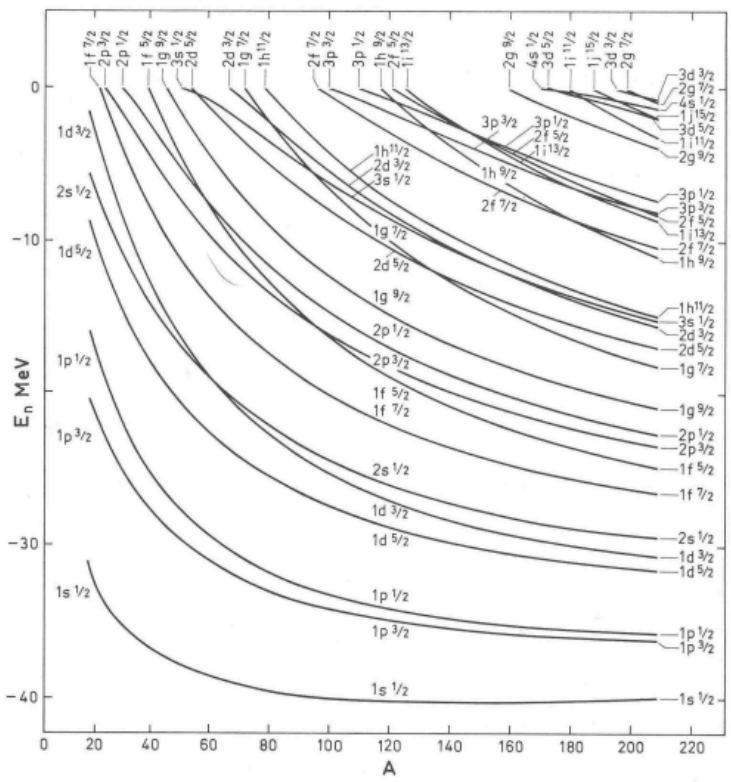

FIGURE 2.4: Level diagram dependencies on mass number for neutrons using a Woods-Saxon potential with spin-orbit interaction. Taken from [Boh69]

The success of the shell model is not only that it predicts the magic numbers but also that it can explain the total angular momentum and parity of the groundstate for complete nuclei. For nuclei with closed shells in both protons and neutrons the total angular momentum (J) and parity ($\pi = (-1)^{\jmath}$) are easily given. Since all spins-states are filled in closed shells they couple to $J = 0$ and because there is an even number of protons and neutrons in each angular momentum shell the parity is positive. Thus in nuclei with two closed shells the ground state configuration is always $J^{\pi} = 0^{+}$. This argument of course also determines the total angular momentum and parity for nuclei with one nucleon outside two closed shells and is just the total spin and parity of the extra nucleon. For example in ^{17}O where a single neutron in the $1d_{5/2}$ shell is outside the two N,Z=8 closed shells, one has $J^{\pi} = 5/2^{+}$. In fact experimental investigations have shown that as long as the nucleus consists of an even number of protons

and an even number of neutrons it always couples to 0^+. Thus for nuclei with an uneven number of nucleons the J^π is determined by the last uneven nucleon. This is very strong evidence for the paring force in nuclei which is also evident from the fact that even-even nuclei are tighter bound than uneven-uneven nuclei. For uneven number of both protons and neutrons one of course faces the problem of angular momentum addition and normally ends op with an array of possible J^π values. This clear picture from the old single particle model is only valid for nuclei with N and Z less than 50 since the level density becomes quite high for heavier nuclei.

In more modern shell models residual interactions such as eg paring are taken into account making the predictability of the model very good when one uses the right interactions and model space. The shell model still has some problems handling phenomena such as halo formation since many shell models use basis sets based on a HO potential which is not suited for describing the extended size of halo nuclei.

As mentioned it might seem strange to talk about an independent particle model in a nucleus where the nucleons are closely packed and would most likely not belong to well defined orbits! But perturbation of the orbits does not occur very frequently since the Pauli principle forbids collisions that deflects nucleons into already filled orbits, thus many of the intuitive collisions are not possible.

For a good review about the basic concepts in the independent-particle shell model see the Nobel lecture by M.G. Mayer [May63] which is very informative whereas for a more detailed description see the book by J.H.D. Jensen and M.G. Mayer [May55]. For a more modern review on the shell model and its implications on nuclear structure see [Cau04].

2.2 Reaction mechanism

A nuclear reaction occurs when two nuclei are brought close enough to touch that is, when they are brought closer than the sum of their radii (Coulomb excitation may also occur when two nuclei interact via their electric fields when they pass at larger distances). Depending on the mechanism through which the reaction takes place the angular and energy dependence of the fragments may vary significantly.

As an example I here consider the variation of total reaction cross section for inelastic proton scattering on a heavy target nucleus with the energy of the outgoing proton. A sketch of this is shown in figure 2.5. At the maximum proton energy (incident proton energy) we see discrete structures corresponding to low lying states in the target nucleus and at low proton energy a Maxwellian peak from protons escaping just over the Coulomb barrier in the proton plus

target nucleus system. These two parts of the spectrum corresponds to *direct reactions* where the proton only interacts with one or a few nucleons in the target, and *compound nucleus reactions* in which the projectile and target combines to form a "long lived" compound nucleus which subsequently decays. Between the two structures is a flat part which is due to *pre-equilibrium reactions* fast but complicated reaction mechanisms such as multiple scattering and resonance reactions. That is we see that different reaction mechanisms contribute to different parts of the spectrum shown in figure 2.5, therefore making it easier to identify the reaction mechanisms involved in a specific set of data. This may of course be very difficult if the incident energy is very low since the compound nucleus and direct contributions may overlap. The graph shown in figure 2.5 also depends on the energy of the incident proton but basically just expands/contracts the flat middle part for higher/lower incident energy (see eg p. 419 in [Hod97] for an example).

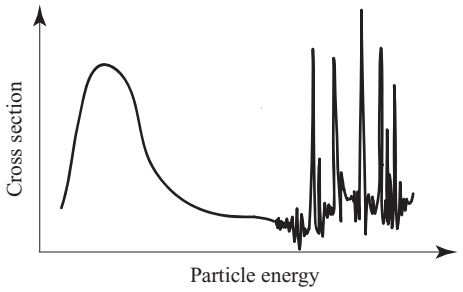

FIGURE 2.5: Sketch of total reaction cross section for varying energy of emitted particle from a nuclear reaction.

In the paragraph above inelastic proton scattering was considered but other reaction products could also emerge when protons are incident on a heavier nucleus. The proton may leave the target nucleus unchanged (*elastic scattering*), or as above excite the target nucleus (*inelastic scattering*). Further *transfer reactions* occurs when one or a few nucleons are transfered between the projectile and target nucleus or a neutron and proton can switch place in a *charge exchange reaction*.

The different reaction channels mentioned above can proceed via different reaction mechanisms such as direct, pre-equilibrium or compound nucleus reactions. A diagram showing how the different reaction mechanisms lead to the same reaction channels is shown in figure 2.6.

For more on nuclear reactions in general see the very nice introductory book by G.R. Satchler [Sat90] and for a more thorough description the book by P.E. Hodgson on nuclear reactions and structure [Hod71].

In the following subsections I will review the different reaction mechanisms, with special emphasis on specific channels which are of interest to this thesis. It is of course not easy to draw unambiguous lines between direct, pre-equilibrium and compound reactions and I will in no way attempt to do so but just try to sketch their characteristics.

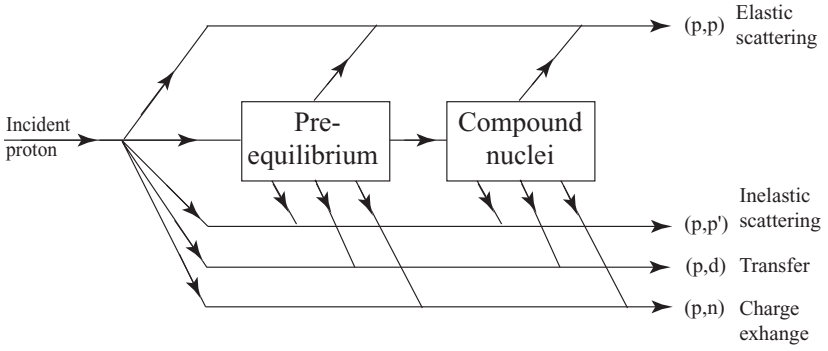

FIGURE 2.6: Diagram showing the different reaction products produced via different reaction channels exemplified with proton scattering. Idea adapted from [Hod71]

2.2.1 Direct reactions

Direct reactions are the simplest reaction type since they normally only involve the interaction between two (or a few pair of) nucleons but can excite the nucleus into many different states. Over the years it has been found that *inelastic scattering* mainly excites collective states, *one-nucleon transfer reactions* excites single-particle states and *multi-nucleon transfer reactions* and *charge-exchange reactions* excites cluster states in the nucleus probed in the reaction [Hod97].

For a reaction to be called direct it must occur fast, on the timescale of the transit time of the projectile through the target nucleus (about 10^{-22} s), and with a minimum of rearrangement in the residual nucleus. In many cases it is a requirement that the wave-functions of the incident and exit channel have a large overlap for a reaction to occur via a direct mechanism. Another requirement on a direct reaction is that the de Broglie wavelength,

$$\lambda = \frac{h}{p} = \frac{\hbar c}{\sqrt{2Emc^2}},$$

of the lightest particle involved is smaller or on the order of the size of one nucleon. If the de Broglie wavelength is larger (1 MeV proton λ ∼4-5 fm) the projectile interacts with the nucleus as a whole and the reaction can hardly be called direct. This argument again proposes that direct reactions dominate for high energy reactions whereas low energy is the regime of compound reactions. Thus particles with $A \cdot E_{kin} \leq 9$ MeV (corresponding to a de Broglie wave length of 1.5 fm) are more likely to react via compound reactions whereas particles with higher energy will tend to react via direct reactions. Since a direct reaction is a localised process with only a few nucleons participating it is most likely to take place at the surfaces of the involved nuclei and not deep inside.

Due to angular momentum conservation the angular momentum of the involved states in the nucleus are given by

$$l = |\mathbf{Q} \times \mathbf{r}|, \tag{2.2}$$

where $\mathbf{Q}$ is the momentum transferred to the nucleus and $\mathbf{r}$ is the distance from the point of the reaction to the center of the nucleus. This means that the maximum angular momentum transfer in a given reaction is

$$l = QR, \tag{2.3}$$

where Q is the magnitude of the transferred momentum and R is the radius of the nucleus. As mentioned above direct reactions mostly occur at the surface of the nucelus thus the maximum angular momentum transfer given by equation (2.3) will in many case be the actual angular momentum transfer.

The common theoretical framework used for direct reactions is the so-called **D**istorted **W**ave **B**orn **A**pproximation (DWBA) which is a fairly precise and tractable model (see eg [Hod71]). The idea of the DWBA model is that the main part of the reactions are elastic scattering and that all other channels are weak perturbations governed by an imaginary potential which removes particles from the elastic channel. The potential used in DWBA is an optical potential consisting of a real and imaginary part. Optical potentials come in various versions and may also contain spin dependent terms. Apart from just using an optical potential the DWBA implements Coulomb distorted wave functions instead of just plane waves.

2.2.1.1 The (d,p) reaction

As one reaction channel which is of special interest here I will here dwell on the direct (d,p) reaction, since it is the reaction mechanism involved when probing the unbound nucleus ^{10}Li.

Historically the (d,p) reaction has been very well studied and has been used extensively to gain knowledge on single particle states in stable and near-stable nuclei. The angular distribution from direct (d,p) reactions was soon seen to be either forward- or backward-peaked dependent on whether the reaction took place at high or low energy, respectivly.

Since the (d,p) reaction is a binary reaction, energy and momentum conservation allows one to extract information about the excitation energy in the produced nucleus by measuring the energy and angle of the outgoing proton. From the angular distibution of the protons the amount of angular momentum transfered can be extracted when models such as DWBA are employed. This is

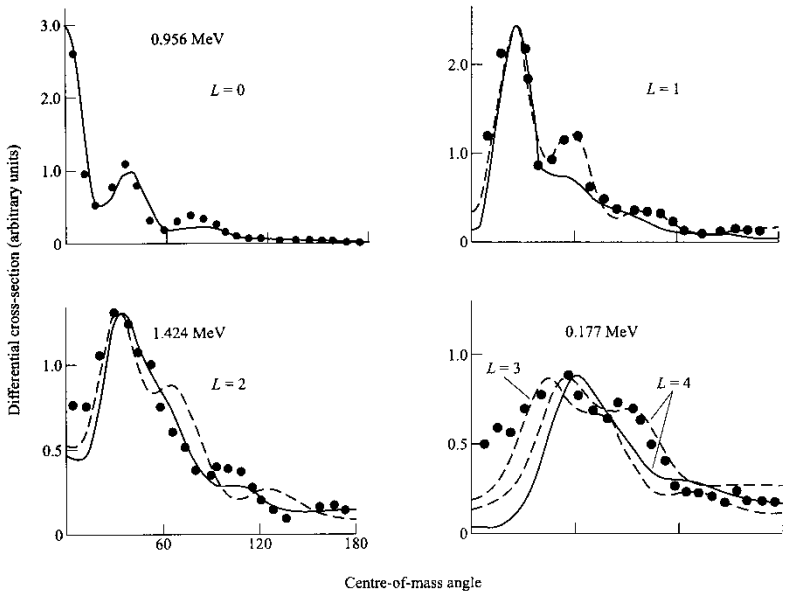

FIGURE 2.7: Comparison of differential cross-section resulting from different channels in the ^{76}Se(d,p)^{77}Se reaction with 7.8 MeV deutrons. Curves are DWBA calculations. Figure taken from [Sat90]

possible since an angular momentum transfer larger than zero implies a momentum transfer on the order of k $\simeq$ l/R to the nucleus (see equation (2.2)). Part of the momentum transfered is, depending on reaction point, into the transverse plane which makes the proton emerge at larger angels on avarage. An example of this is shown in figure 2.7 where the differential cross section for various states involving different angular momentum transfer are populated in the ^{76}Se(d,p)^{77}Se reaction with 7.8 MeV deuterons is seen. Note that the first and largest maximum moves towards larger angles as the angular momentum transfer increases. The lines shown in figure 2.7 are two different DWBA calculations. It was in fact this forward peaked structure that lead Butler [But50] to propose a direct reaction mechanism in contrast to the compound model. Imidiately Butler also discovered the possibility of extracting the transferred angular momentum from the angular distribution of the cross-section (see eg [But58]).

Furthermore in neutron pickup reactions from deuteron targets onto exotic nuclei, calculations predict that the angle integrated cross-section reaches a maximum at E_{Lab} $\simeq$3-5 MeV/u [Len98] compared to E_{Lab} $\simeq$7-10 MeV/u in stable nuclei [Sat83]. Thus indicating that REX-ISOLDE with a present maximum

energy of 3.1 MeV/u is very suitable for (d,p) pickup reactions (for more on REX-ISOLDE see section 3.4).

For an extensive review on direct reactions see the book by G.R. Satchler [Sat83] and for more recent work on transfer reactions with exotic nuclei see [Len98].

2.2.2 Compound nucleus reactions

In a compound nucleus reaction a long lived system consisting of the target and beam nuclei is formed. This system lives long enough for the incoming beam nucleons to spread their energy among the target nucleons, thus making a collective excitation in the system. The life time of a compound nucleus may range from 10 to 10^7 times the transit time of the beam nucleus through the target nucleus, that is up to 10^{-15} s. The life time clearly depends very much on the incident energy, since higher incoming energy transfers more energy into the system and makes it easier to give one nucleon enough energy to escape, therefore giving compound systems created at higher energy a shorter life time. The decay mechanism in compound nuclei is of statistical nature, where eventually one nucleon, or a small group, by statistical fluctuations receives enough energy to escape the compound system. In most cases this leads to the evaporation of a low energy neutron or proton since this is more probable than emitting a composite particle.

Since the energy is redistributed many times among the nucleons in the compound nucleus the decay of the system has no "memory" of its creation, thus giving a rather uniform angular emission of particles. The idea that the compound nucleus has no "memory" is of course not completely true since conservation of eg angular momentum must be fulfilled, but compared to direct reactions the angular distribution from compound reactions are much more isotropic.

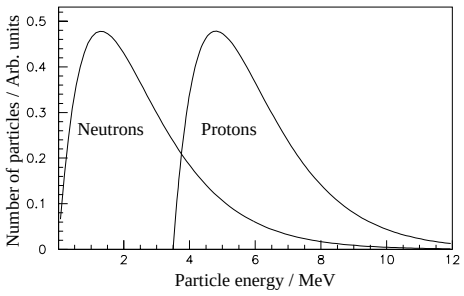

FIGURE 2.8: Energy distribution in center of mass for neutrons and protons emitted from the compound system ^{21}F. Note the effect of the Coulomb barrier which suppressed low energy protons.

Due to the statistical nature of the energy distribution among the nucleons in the compound nucleus the energy of the emitted proton or neutron will have a Boltzmann like distribution just above the relevant barrier

$$E \propto (\epsilon - U_C)e^{(U_C-\epsilon)/T} \tag{2.4}$$

where ϵ is the energy of the emitted nucleon and U_C is the Coulomb barrier (zero for neutrons) and T is the nuclear temperature[1]. For a derivation of this formula see eg the book by Siemens and Jensen [Sie87]. Taking ^{21}F as an example of a compound nucleus (^{9}Li+^{12}C) and calculating the proton and neutron emission spectra (figure 2.8) we see the exponential behavior for the neutrons which are unaffected by the Coulomb barrier whereas the protons are suppressed by the presence of the Coulomb barrier at low emission energy (the normalization is arbitrary). The value used for the calculation presented in figure 2.8 is

$$U_C = \frac{e^2}{4\pi\epsilon_0}\frac{Z_1 Z_2}{r} = 1.44\frac{Z_1 Z_2}{1.2A^{1/3}}\ \mathrm{MeV} = 3.5\ \mathrm{MeV} \tag{2.5}$$

and T is estimated to $\sim$ 1.3 MeV. The formula in equation (2.4) is not the complete picture, for example the penetration of the Coulomb barrier is not a sharp edge but rather a smooth transition making the cut-off at 3.5 MeV for protons more rounded.

The idea of a compound nucleus was first proposed by N. Bohr [Boh36, Boh37] but for a newer, and maybe more understandable, description see eg sections in [Hod71, Hod97]

2.2.3 Resonances and virtual states

Since all states in ^{10}Li are particle unbound is would be appropriate to say a few words about *unbound* states, that is *resonances* and *virtual states*.

A *resonance state* is an unbound state which has a finite half-life even though it lies above the disintegration threshold. The occurence of a resonance is a pure quantum mechanical phenomenen and can take place when a potential barrier of finite thickness is present. In the nuclear physics case the potential creating the barrier would be either from a Coulomb potential, if the projectile is charged, or a from an angular momentum potential if the relative angular momentum is non-zero. In the schematic picture shown in the left part of figure 2.9 it is visualised how an incident wave impinges on a potential barrier, tunnels through the barrier and enters the interior of the nucleus. When the wave packet is inside the potential barrier it cannot easily escape, since it again has to tunnel through the barrier, and therefore stays inside the nucleus for a substantial time (many cycles around inside the nucelus). Resonances frequently have widths on the order of keV thus giving life-times on the order of 10^{-20} s (τ=$\hbar/E$) whereas a

[1] The definition of a nuclear temperature is some what difficult since temperature is a statistical phenomena and a nucleus only contains on the order of 100 particles. Typical evaporation temperatures for compound nuclei are on the order of 1-2 MeV.

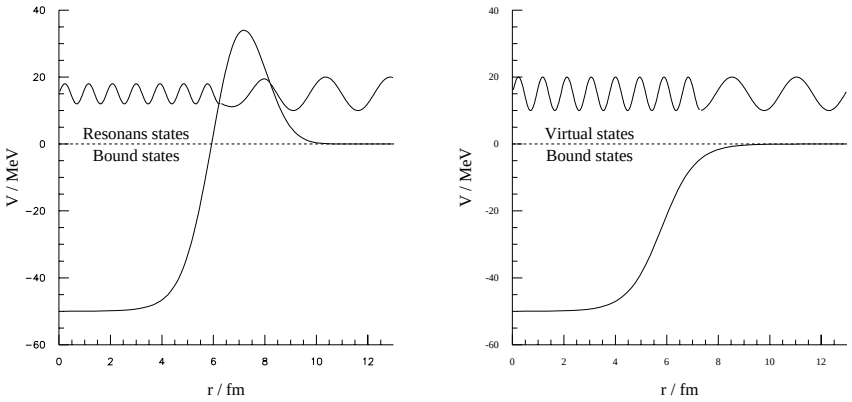

FIGURE 2.9: Two potentials showing the difference between a resonance and vitual state. See text for further explanation.

50 MeV nucleon traverse 10 fm in about 10^{-22} s, that is it makes ~ 100 cycles inside the nucleus.

If no barrier is present the wave packet can escape essentially unhindered since now only the varying depth of the potential can lead to reflection. This situation is schematically shown in the right part of figure 2.9 and is called a *virtual state*. In most cases the presence of a nuclear potential without barrier only distorts the wave packet very little thus the probability of trapping the wave packet for many cycles is minute. This leads in general to a shorter life-time for virtual states and concequently to a larger width.

Since the modification of the wave packet is only minute it can be very difficult to probe virtual states in transfer reactions when a nucleon is being transferred to the virtual state. A virtual state is more likely to leave a trace when it is created in a stripping reaction where the nucleon is simply left in the virtual state (eg high energy one-neutron stripping from ^{11}Li which leaves the remaining halo neutron in the s-wave ground state). On the other hand resonance states show up in most kind of reactions also low energy transfer reactions since the transferred nucleon is much more easily trapped which manifests itself by an increase in cross-section at the resonant energy. The resonant cross-section has the *Breit-Wigner* shape

$$\sigma(E) \propto \frac{\Gamma}{(E - E_R)^2 + \Gamma^2/4} \tag{2.6}$$

where E_R and Γ is the position and width of the resonance, respectivly. This

expression for the resonant cross-section was first derived by Breit and Wigner [Bre36] by the means of second order perturbation theory (see eg a more recent derivation in [Bra83] or other text book on nuclear or atomic physics). Since the *Breit-Wigner* formula is derived in second order perturbation theory it is assumed that the coupling is weak thus one must use it with caution in nuclear physics where the coupling may be strong. Especially if the resonance is located close to a threshold, compared to the width of the resonance, one has to take the changing fase-space into account. The growth in phase-space with energy above the threshold can easily be taken into account, eg by using an R-matrix type calculation which uses an energy dependent width (see [McV94] for an approximation of the energy dependence of the width). The formal theory for R-matrix calculations were developed for resonant compound reactions, see [Lan58].

CHAPTER 3

Experimental equipment

In this chapter I will introduce the experimental equipment with which we have performed the experiments discussed in this thesis.
This chapter will include an introduction to how radioactive isotopes are produced and ionized, the general layout of ISOLDE and a more thorough description of the newly constructed post-accelerator REX-ISOLDE at ISOLDE.

3.1 Introduction

In the early era of nuclear physics radioactive isotopes were often investigated via decay products emerging from thick production targets. This method of course had the disadvantage that the decay products (especially baryons) loose much of their kinetic energy inside the target. In modern nuclear physics the exotic nuclei are often produced, separated and then transported to a decay or reaction area. With these new methods it is possible to either stop a low energy beam <100 keV in a very thin foil to detect decay products or make an energetic beam react with a secondary target. The techniques developed for separating the radioactive isotopes from the stable have had a major impact on the quality and possibilities in nuclear physics, thus making it feasible to perform detailed decay experiments on nuclei with production rates of less than 1 ion per second.

3.2 How to produce short-lived radioactive isotopes

Since radioactive isotopes do decay it is necessary to produce them when trying to investigate their properties. For the isotopes with relatively short half-lifes (days to minutes) collection and off-line analysis has been feasible more or less since it became possible to accelerate beams to more than a few Mev/u. But today where most isotopes of interest have half-lifes less than seconds it is necessary to produce and measure decays/reactions on-line. In the following subsections I will shortly review the two main methods for producing radioactive isotopes.

3.2.1 In-Flight Separation

In the **I**n-**F**light **S**eparation method (IFS) the isotopes are, as the name indicates, separated In-Flight. This is done by bombarding a relatively thin target (some mm) by an energetic beam of stable nuclei (>50 MeV/u) and through reactions producing the relevant radioactive isotopes which emerge from the target with energy and momentum per nucleon close to that of the incoming beam. In IFS the most common reaction mechanism is that of projectile fragmentation where some of the peripheral nucleons are shaved off in the very fast reaction. The presence of different reaction channels produces a cocktail beam of many stable and radioactive isotopes. This mixed beam is then tagged (that is each ion is identified by mass and charge) through one or several analysing magnets, energy loss detectors, time-of-flight, etc. before it arrives at the experimental setup. The tagging of individual ions makes it possible to perform ”many” experiments at the same time since many isotopes occur in the beam at the same time. Because

the radioactive isotopes are created In-Flight the time from production to reaction is very fast (down to $\sim$ 100 ns) thus allowing to investigate extremely short lived isotopes. This mixed structure and time scales of IFS makes it an excellent way to search for new isotopes close to the proposed driplines.

3.2.2 The ISOL technique

The technique of **I**sotope **S**eparation **O**n **L**ine (ISOL) was pioneered at the Niels Bohr Institute by Kofoed-Hansen and Nielsen in 1951 when they produced, transported and subsequently measured the decay properties of ^{91}Kr [Kof51]. Today the development of the ISOL method has moved us 8 isotopes further away from stability with the study of ^{99}Kr [Ber03a].

In the ISOL method the radioactive isotopes are produced in a thick target (many cm) in which they are stopped or a thinner target followed by a catcher. By heating the thick target the isotopes are made to diffuse out of the target and into an ion source. These targets are often made of many thin foils or powder to speed up the diffusion process whereas the thin targets are specific to the radioactive product wanted (via specific reaction mechanisms). The ion source unit can be of many different types each chosen to enhance the ionization of a specific isotope. The most selective case is that of laser ionization (utilized at ISOLDE and LISOL at Leuvain-La-Neuve) where a specific chemical element (eg Be) can be ionized in 2 or 3 steps, see [Fed00]. The method of resonant ionization can in the extreme case separate isomers. At ISOL facilities the reaction mechanisms for producing radioactive isotopes are somewhat more unclear compared to IFS since both spallation, target fragmentation and fission can contribute in producing the same isotope.

Since the isotopes have to diffuse out of the target before they are ionized and accelerated the shortest time from production to detection is about 5 ms thus limiting the ISOL method to isotopes with half-lifes longer than a few ms. The transport time can be reduced at facilities using thin targets and a gas catcher since the radioactive isotopes are not stopped in the target and consequently do not have to diffuse out of the target. In this case eg IGISOL in Jyväskylä, Finland the transport time can be reduced to $\sim 100\mu$s.

In figure 3.1 a comparison of the ISOL and IFS methods is shown. As shown on the figure post-acceleration is possible for both ISOL and IFS though it might be more complicated for IFS since the radioactive beam first must be slowed down from >50 MeV/u to $\sim$10 keV/u before re-acceleration. For a review on production methods and related topics see [Gei95]. In the next section I will concentrate on ISOLDE which is the Aarhus groups home field (see eg [Eur03]

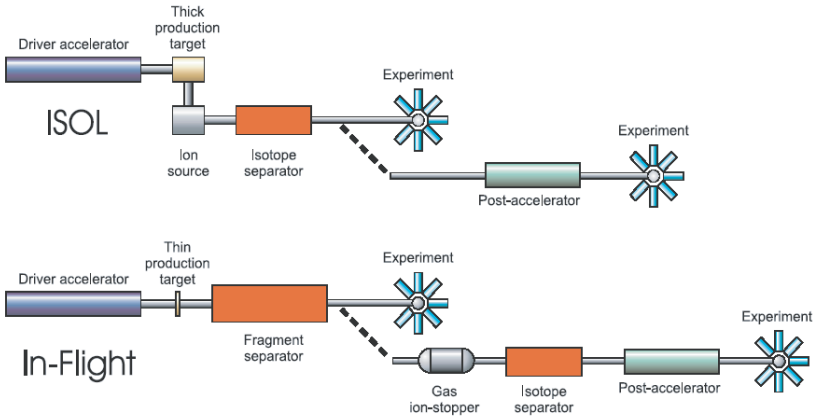

FIGURE 3.1: Graphical comparison of ISOL and In-Flight separation methods. Graphic taken from [Eur03]

for a compilation of present and planned facilities).

3.3 The ISOLDE facility

Inspired by the work of Kofoed-Hansen and Nielsen many nuclear physicists and chemists argued in the start of the sixties for a facility capable of producing short lived isotopes in order to push the limits of nuclear knowledge even further. In 1965 the construction of the first ISOLDE separator magnet was initiated (in fact in Aarhus) and already in 1967 the first successful experiment was performed driven by the 600 MeV proton **S**ynchro**C**yclotron (CERN SC). Since then the ISOLDE facility has been upgraded several times and even moved to its present place close to the 1 GeV **P**roton **S**ynchrotron (PS) booster (the PS booster has recently been upgraded to 1.4 GeV). The present ISOLDE facility became operational in 1992 [Kug92]. The latest development at ISOLDE is the construction of the post-accelerator REX-ISOLDE which I will return to in the next section. For a review of the first 30 successful years in the history of ISOLDE see [Jon00].

ISOLDE [Kug00] is, as the name suggest, an ISOL[1] facility, situated at CERN in Geneva, Switzerland. The ISOLDE radioactive isotope production is driven by the PS Booster which provides a pulsed 1.4 GeV proton beam. The

[1]The DE should according to many people (especially Danes) be an abbreviation for Danish Engineering!

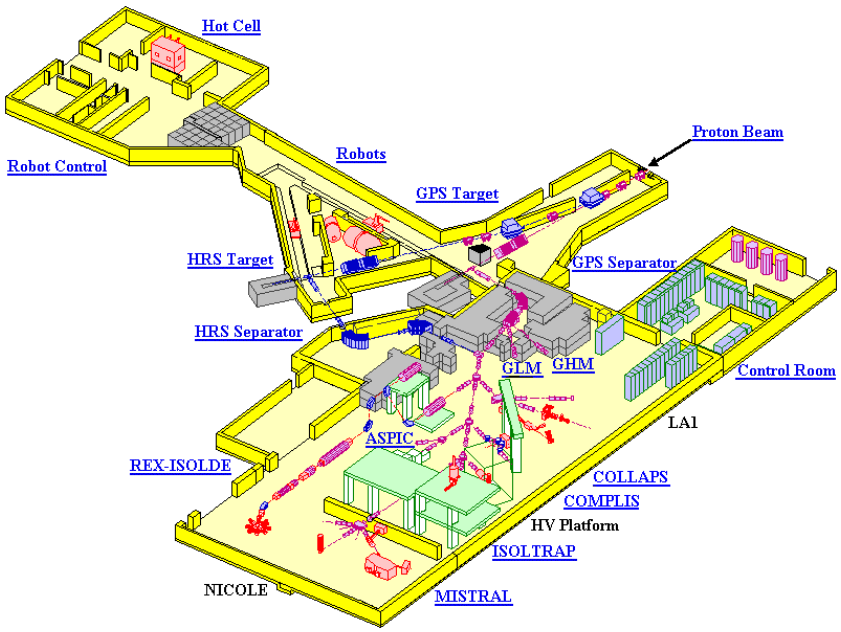

FIGURE 3.2: Layout of the present ISOLDE facility. Graphic downloaded from [ISOLDE]

minimum separation between two pulses from the PS Booster is 1.2 s and the intensity can be varied from 10^{10} to 3×10^{13} protons per pulse (ie up to 4μA). The pulsed structure of the ISOLDE beam is very useful when investigating radioactive decays and reactions of very short-lived species (less than a few 100 ms) since it makes it possible to separate beam related events from background due to the time distribution after proton impact on the ISOLDE production target. The PS Booster proton beam is incident on a target at one of two target stations. The target thickness is on the order of 10 to 50 g/cm^2 and can be of either powder, liquid or solid (thin foils or pellets). The produced isotopes diffuse out of the heated target ($\sim 2000^\circ$) and into an ion source which can be of different type depending upon the chemical properties of the wanted element. Presently ISOLDE has surface, laser, hot plasma and cold plasma ion sources the latter being a plasma ion source with a cooled transfer line to enhance volatile elements since all other elements will ”stick” on the cold surface. After ionization the ions will be accelerated to 20-60 keV and led to either the **G**eneral **P**urpose **S**eparator (GPS) or **H**igh **R**esolution **S**eparator (HRS) where they will be mass separated with a resolving power of 1/2400 or 1/30000, respectively. After mass separation the beam is transported to an experimental setup at one of the beam-

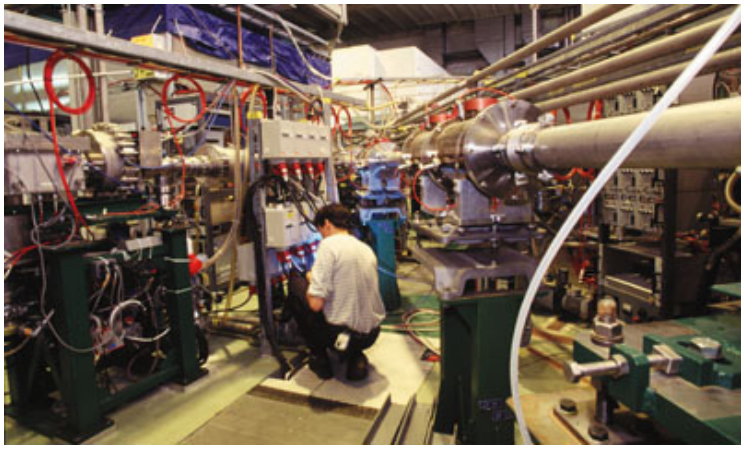

FIGURE 3.3: Photograph from the ISOLDE experimental hall.

lines. Some of the beam lines are dedicated to permanent experimental setups, eg ISOLTRAP where mass measurements of radioactive ions occur whereas other beam lines are for temporary setups. In figure 3.2 a layout of the ISOLDE hall is presented and in figure 3.3 a photograph from the ISOLDE hall is shown.

3.4 The post-accelerator REX-ISOLDE

In the lower left corner of the main hall of ISOLDE shown in figure 3.2 the newly constructed REX-ISOLDE is present. The **R**adioactive Beam **Ex**periement (REX-ISOLDE) [Hab00] is an accelerator specifically designed to perform fast acceleration of short-lived isotopes in the low energy range 0.8-3.1 MeV/u. At these energies, in the top end of the astrophysical interesting energy range, information about the nuclear synthesis might be extracted. In nuclear structure a few MeV/u is also very interesting since clean one- or two-nucleon transfers can be performed on light nuclei at these energies. Especially the (d,p) reaction on neutron-rich projectiles may prove very fruitful for investigating the nuclear structure of even more neutron-rich nuclei.

When entering REX-ISOLDE the ISOLDE beam is first accumulated and cooled in the REX-TRAP [Sch02], a Penning trap, for about 20 ms before it is transported to the REX-EBIS charge breeder where the ions are charge breed for 5-18 ms. REX-EBIS [Wen01] is an Electron Beam Ion Source which is designed to charge breed the 1^+ ions from the ISOLDE ion source to a given charge state with $A/q < 4.5$ such that the ions can be accelerated in the REX-LINAC. The

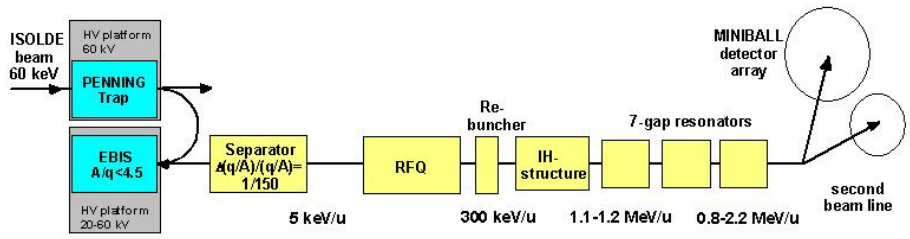

FIGURE 3.4: Schematic overview of REX-ISOLDE. Graphic downloaded from [REXweb]

ions leave REX-EBIS with 5 keV/u and before entering the REX-LINAC an A/q selection is performed by an electrostatic and magnetic mass separation. The REX-LINAC consists of an RFQ and IH-structure [Sie02] which accelerates the ions to 1.1-1.2 MeV/u and a 7-gap resonator [Pod02] that further accelerates the ions to energies in the range 0.8-2.2 MeV/u. The 7-gap resonator has recently (in the shutdown period 2003-2004) been upgraded to a 9-gap resonator to allow acceleration up to 3.1 MeV/u. After acceleration the radioactive ion beam is again mass separated before it enters one of the REX-ISOLDE beam lines. Beam line 1 is dedicated to the MiniBall gamma detector array. The first radioactive beam was accelerated at REX-ISOLDE in the autumn of 2001 were Coulomb excitation of ^{26}Na was performed at the Mini-Ball setup as described in [Kes03]. In this article the 3.1 MeV/u upgrade of REX-ISOLDE is also described. In figure 3.4 a schematic overview of the main components of REX-ISOLDE is shown.

Due to the superposition of the ISOLDE 1.2 s time structure and the 49 Hz cycle of the REX-EBIS a complicated time structure of the radioactive beam occurs. The length of the REX-EBIS pulses is on the order of 10-50 μs. The pulse from the REX-EBIS is again overlaid with a micro structure in the REX-LINAC which depends on the final energy of the beam, ranging from 0.3 ns bunches separated by 10 ns at 2.2 MeV/u to a continuous beam at 0.8 MeV/u. This micro structure has so far not been seen/used in our experiments but holds in principle the possibility for time-of-flight measurements.

One problem with REX-ISOLDE is the rest-gas in the EBIS which in some cases can give a very large contamination. For example in the ^{9}Li case the first experiment was performed with ^{9}Li^{+3} ions which has the same A/q as ^{12}C^{+4}. As seen in figure 3.5 the amount of ^{12}C^{+4} from REX-EBIS is almost 200 nA or about 10^9 ions per second thus making it very difficult for us to see the ^{9}Li beam of about 10^5 ions per second. The number of ^{12}C^{+4} is probably overestimated by

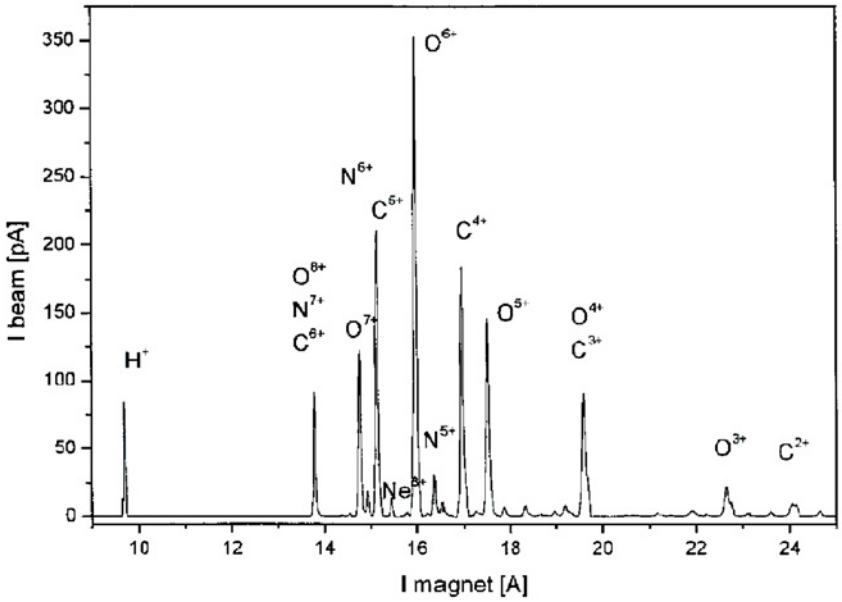

FIGURE 3.5: Mass-analysed rest-gas spectrum from REX-EBIS.Spectrum adopted from [Wen01]

an order of magnitude or two [2] but it is still an overwhelming amount compared to the $^{9}Li^{+3}$ ions. In our second experiment, which led to the data presented in chapter 5, the decision was made to try $^{9}Li^{+2}$ (difficult for the LINAC since A/q=4.5) where the most abundant contamination was $^{18}O^{+4}$. From figure 3.5 it is seen that $^{16}O^{+4}$ (which has the same ionization effectively as ^{18}O) is down by a factor of two compared to $^{12}C^{+4}$. This means that $^{18}O^{+4}$ contamination is suppressed by about three orders of magnitude, due to its natural abundance of 0.2%, compared to the $^{12}C^{+4}$ contamination present at the first experiment. Including the two order of magnitude reduction discussed above we would expect on the order of 10^{4} $^{18}O^{+4}$ arriving at the setup per second. Due to this significant reduction of contamination the experiment was now feasible.

Another thing that has to be taken into account when performing reactions with radioactive beams is that they normally have very low intensities. This fact was clearly visible in the paragraph about $^{12}C^{+4}$ contamination which would not have been a problem with a stable beam of say 10^{12} per second. Furthermore since it is the heavy particle (at least in reactions with protons or deuterium)

[2] We had some additional losses due to bad focusing of the REX beam at the entrance to the reaction chamber.

that is accelerated the experiment is performed in so called inverse kinematics. This has the advantage that most reaction products are focused in the beam direction but in turn this focusing makes the angular resolution rather poor. In inverse kinematic most of the beam energy is preserved for translational energy and only a fraction can enter in a given reaction since the center of mass energy is restricted (eg for ^{9}Li on a deuteron target at 2.36 MeV/u E_{CM}=3.86 MeV). The ratio between translation and center of mass energy has the disadvantage that only limited excitations can be achieved in the reaction products but the advantage that the reaction products have a larger translational energy after the reaction making them easier to detect using telescope detectors. In [Gun01] the potential and limitations of low-energy and low-intensity beams has been investigatede by reactions with stable beams. They demonstrated that it easily is feasible to perform transfer and Coulomb excitations with beam intensities of $\sim 10^{6}$ nuclei per second. This test was done with one MiniBall gamma detector, thus using a large solid angle Si-detector would make it possible to perform reactions a lower intensities due to higher efficiency and less background. These low intensities of course requries a lower intensity of possible contaminant beams.

In fact the intensity of the REX-ISOLDE beam also has an upper limitation set by the dead-time of the data aquisition. A typical example could be an 8 μs data taking window followed by 20 μs dead-time due to data processing. This only allows for one reaction per REX-EBIS pulse, which arrives at the detector setup at a frequency of 49 Hz. Assuming a cross-section of 10 mb, a solid angle coverage of 20% and 10^{19} target particles per cm^2 (about 1 μm CD target) this gives a maximum intensity of 5×10^{8} particles per second, which again arrives at the setup in 49·35 μs = 1.7 ms out of the 1 s thus reducing the intensity with about a factor of 1/600. Therefor an intensity of about 10^{6} particles per second (being bunched at REX-EBIS) is a conservative upper limit if random coincidences is to be avoided. Further it is crucial that the intensity of the contaminant beam is much less than 10^{6} per second otherwise the contamination would swamp the data aquisition.

3.5 Detectors

In our work at ISOLDE several detector types have been used to detect different reaction or decay products in different energy ranges. During the last 4 years in the group, I have experienced working with different neutron detectors (^{3}He detectors and Tonerre - a large neutron time-of-flight array), gas-Si telescopes, Si-Si telescopes both in segmented and unsegmented versions, and plain Si detectors. Due to the many different kinds of experiments we perform our

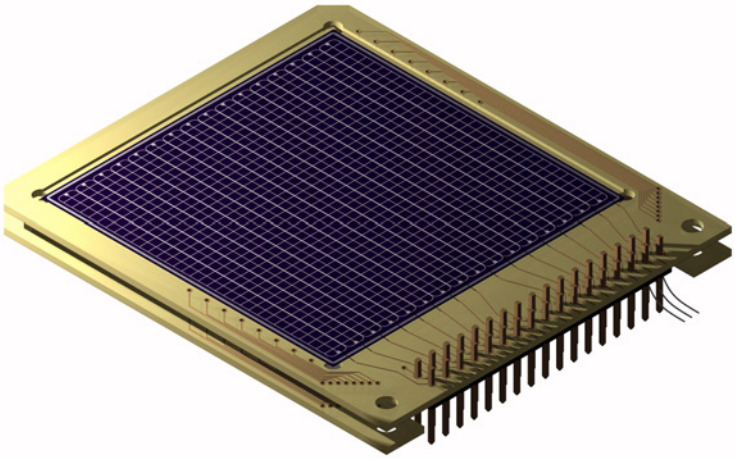

FIGURE 3.6: Telescope with newly designed 16×16 strip DSSSD backed by a Si-pad detector. Figure adopted from [Ten04]

detector setup is rarely the same making it very interesting to participate in the experiment preparations. In the following I will focus on the segmented Si-Si telescopes which have been used for the REX-ISOLDE experiments.

Our Si-Si telescopes are constructed from a thin **D**ouble **S**ided **S**ilicon **S**trip **D**etector (DSSSD) and a thick Si-pad detector. The area of both detectors is 50×50 mm^2 and they are placed in a holder approximately 5 mm apart. The DSSSD have 16 front and 16 back strips giving a spatial resolution of 3.1×3.1 mm^2 and a thickness around 60-70 μm (we presently have 3 thin DSSSDs, two thick around 300 μm and one 500 μm). The Si-pad detectors also come in various thicknesses from 700-1500 μm. A typical telescope setup would be a 60 μm DSSSD in front of a 1500 μm Si-pad which allows for unambiguous identification of protons, deuterons, tritons and alpha particles with energy above 2.5 MeV, 3.0 MeV, 3.5 MeV and 10 MeV, respectively (for protons over 15 MeV punch through sets in and identification gets tricky).

In the first two REX-ISOLDE experiment (^{9}Li+^{2}H and ^{9}Li+^{9}Be June 2002) only one DSSSD telescope was used. The DSSSD was 64 μm thick and had a 600 nm contact- and deadlayer. See [Ber03b] for a description of the DSSSD.

In the third REX-ISOLDE experiment (^{9}Li+^{1}H elastic resonance scattering October 2003) several DSSSDs were used some of which had a novel design with a thinner deadlayer (100 nm) [Ten04] and the contact-layer was replaced by a grid covering 2% of the total area. A drawing of the new detector design is shown in figure 3.6.

The procedure for determining which pixel have been hit is straightforward in the case of only one hit but requires an energy matching (normally 50 keV) between front and back strips to determine which front and back strip that correspond to the same particle when the detector have been hit more than one time. The energy matching condition is also applied to events with only one hit to assure that it is a physical hit and not just noise. In many cases low energy electronic noise is present in one or several strips.

In beta decay experiments where an isotope has been stopped in a thin foil energy corrections for energy loss in detector deadlayer and foil can be very important. For the energy loss correction to be possible the charge and mass of the ejectile is needed. With this information it is possible to calculate backwards out through the deadlayer and stopping foil, successively. In the reaction case this correction is not as important partly due to the lack of knowledge concerning the reaction point in the target but also due to the limited angle resolution which influence the final extraction of excitation energy much more. For more details on the energy loss correction procedure see [Ber03b].

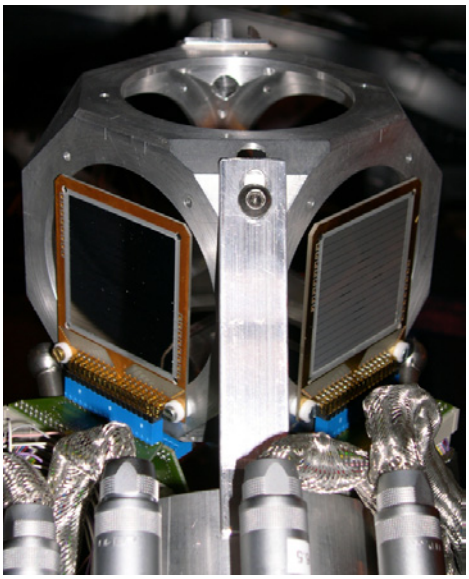

FIGURE 3.7: Photograph of the detector setup used for a decay spectroscopy experiment on ^{11}Li.

In general the different DSSSDs have energy resolution around 30-40 keV (FWHM) when deadlayer corrections have been performed and have a detection efficiency close to 100% where the events lost are discarded due to insufficient charge collection in either front or back strip (the energy matching cannot be fulfilled).

Calibrating the DSSSDs is either done off-line with alpha-sources (^{148}Gd, ^{239}Pu, ^{241}Am and ^{244}Cm) or on-line with the radioctive alpha-emitter ^{20}Na. For more on the calibration proceedure see [Ber03b].

As an example a photograph of the detector setup used in a ^{11}Li beta-decay experiment (IS417 at ISOLDE) is shown in figure 3.7. In this experiment 4 DSSSD telescopes and 16 ultra-thin Si telescopes with 1 μm integrated ΔE detector and 10 mm^2 active area were used together with the Tonnerre neutron time-of-flight array. The data from IS417 is currently being analysed by our

collaborators in Madrid.

CHAPTER 4

Why study the unbound nucleus ^{10}Li?

In this chapter I will explain why it is interesting to study the particle unbound nucleus ^{10}Li.

4.1 Introduction

At first glance the interest in the particle unbound nucleus ^{10}Li might seem minute but due to the very interesting structure observed in the next Li isotope, ^{11}Li, the properties of ^{10}Li are indeed of great interest.

In the mid eighties it was discovered that ^{11}Li had a very large interaction cross section [Tan85b], which later was interpreted as caused by a so called two-neutron halo structure in ^{11}Li [Han87], that is the neutron distribution in ^{11}Li has a large tail (r_{RMS} = 3.12±0.02 fm [Oza01]) outside the normal radius expected for a mass 11 nucleus ($r_{RMS} \simeq$ 2.7 fm, see equation (2.1)). Thus in a schematic picture the ^{11}Li nucleus can be thought of as a ^{9}Li core surrounded by two loosely bound neutrons (S_{2n}=300 keV). Requirements for the long exponential tail characteristic for halos is a low separation energy (stable nuclei $S_{p/n}$ ∼8 MeV) to enhance the tunneling probability and some s- or p-wave admixture, where no angular momentum barrier is present, thus giving a lower barrier through which the nucleon(s) must tunnel. An exaggerated illustration of the two-neutron halo nucleus ^{11}Li is shown in figure 4.1. Due to the fact that ^{10}Li is unbound ^{11}Li is a so called Borromean[1] nucleus, that is none of its subsystems ^{9}Li-n or n-n are bound. To be able to get a theoretical understanding of the very interesting nucleus ^{11}Li knowledge on the unbound subsystems is necessary, see eg [Gar02].

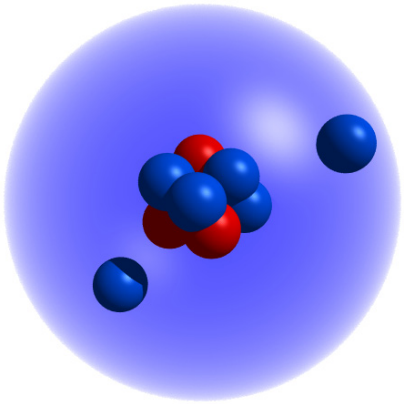

FIGURE 4.1: Exaggerated illistration of the Borromean nucleus ^{11}Li.

4.2 Previous knowledge on ^{10}Li

It is a well known fact, both experimentally and theoretically (see section on shell model), that the ground-state spin-parity of ^{9}Li is $3/2^-$ thus coupling to a $1p_{1/2}$ neutron (next level in shell model see figure 2.3) the ground state of ^{10}Li should be either 1^+ or 2^+. But in this region of light neutron-rich nuclei the $2s_{1/2}$ is normally seen as an intruder state below the $1p_{1/2}$ and thus 1^- and 2^-

[1]The word Borromean is adapted from the Italian family Borromeo which used the Borromean rings in their family crest.

Reaction	-S$_n$ (MeV)	Γ (MeV)	Proposed state	ref.
^{9}Be(^{9}Be,^{8}B)^{10}Li	0.80(25)	1.2(3)	Ground state	[Wil75]
^{11}B(π^-,p)^{10}Li	0.15(15)	<0.4	Ground state	[Ame90]
^{18}O +^{nat}C (frag.)	<0.15		Ground state	[Kry93]
^{11}B(^{7}Li,^{8}B)^{10}Li	$\geq$0.10	<0.23	Ground state ($s_{1/2}$)	[You94]
	0.54(6)	0.36(2)	Excited state ($p_{1/2}$)	
^{11}Li+C (strip.)	<0.05		Ground state ($s_{1/2}$)	[Zin95]
Breakup of ^{11}Li	0.21(5)	$0.12^{+0.10}_{-0.05}$		[Zin97]
	0.62(10)	0.6(1)		
^{18}O+^{9}Be (frag.)	<0.05		Ground state	[Tho99]
^{10}Be(^{12}C,^{12}N)^{10}Li	0.24(4)	0.10(7)	($p_{1/2}$, J^π=1$^+$)	[Boh99]
^{9}Be(^{13}C,^{12}N)^{10}Li	0.53(6)	0.35(8)	($p_{1/2}$, J^π=2$^+$)	[Boh99]
^{9}Be(^{9}Be,^{8}B)^{10}Li	0.50(6)	0.40(6)	($p_{1/2}$)	[Cag99]
^{9}Li(^{2}H,p)^{10}Li	0.35(11)	<0.32		[San03]

TABLE 4.1: Summary of previous experimental work on ^{10}Li and their results.

states are also possible candidates for the ^{10}Li ground state. The reason for $2s_{1/2}$ intruding below the $1d_{1/2}$ and $1p_{1/2}$ is subject of debate and several explanations have been proposed (see eg [Cau04] for a discussion of the same problem in ^{11}Be). In the following I will refer to the four virtual/resonance states in ^{10}Li as s-doublet (1$^-$ and 2$^-$) and p-doublet (1$^+$ and 2$^+$).

The ordering of the s-wave virtual states and p-wave resonance states in ^{10}Li is much debated. There exists however a general consensus that the ground state of ^{10}Li is a very low lying s-wave virtual state situated 30 to 50 keV over the ^{9}Li+n threshold. Furthermore a p-wave resonance around 0.5 MeV above the ^{9}Li+n threshold has also been reported on several occasions.

In table 4.1 a compilation of previous experimental results on ^{10}Li together with possible state assignments proposed by the authors is shown. Thus at the present time experiments seem to indicate that the low-energy level scheme of ^{10}Li is as follows: A $s_{1/2}$ ground state at 30 keV (relative to ^{9}Li+n), a $p_{1/2}$ around 300 keV excitation energy (maybe J^π=1$^+$) and another $p_{1/2}$ around

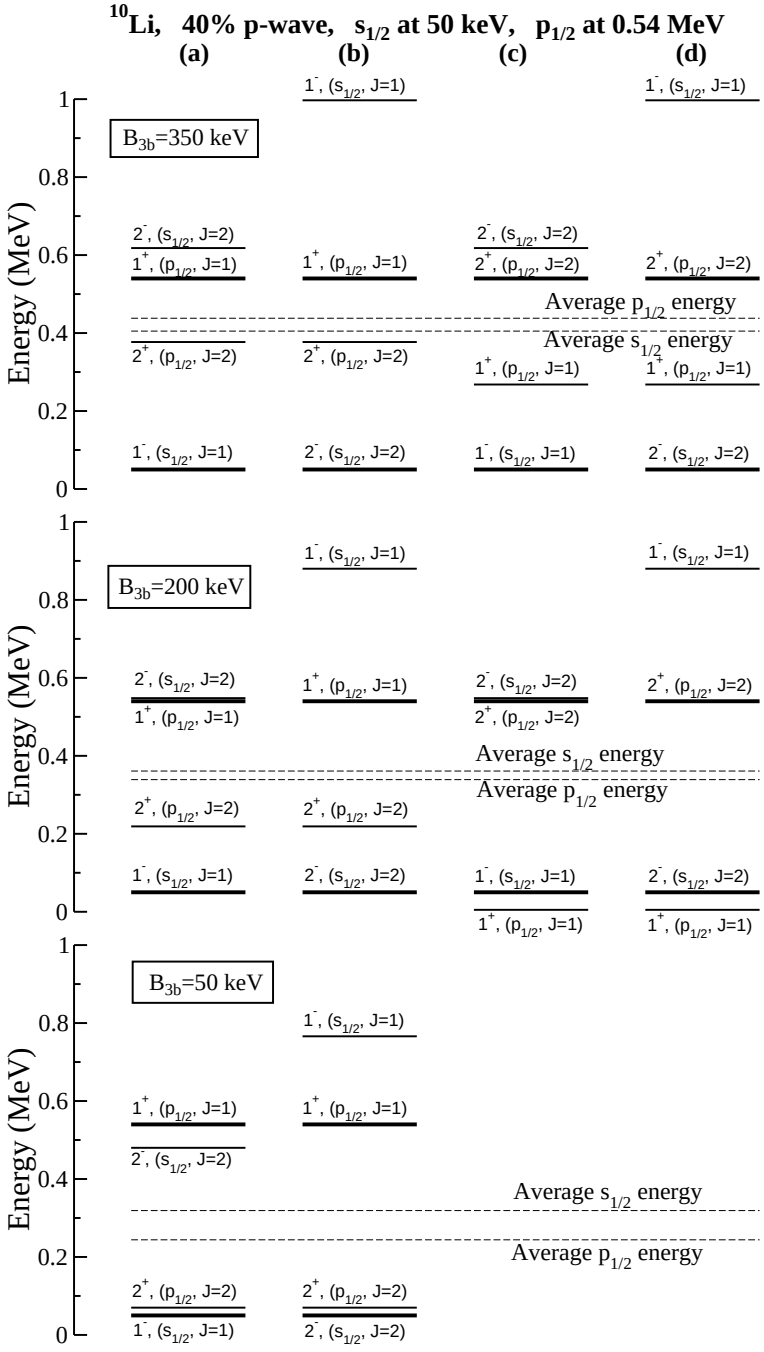

FIGURE 4.2: Theoretical calculations for the levels in ^{10}Li [Gar02]. For explanation see text.

500 keV excitation energy (maybe J^{π}=2^{+}).

4.3 Theoretical work on ^{10}Li

Garrido *et al* [Gar02] have recently performed calculations based on the experimental "facts" discussed above. They assume a $s_{1/2}$ state at 50 keV and a $p_{1/2}$ state at 540 keV plus a 40% p-wave content in the ground state configuration of ^{11}Li. In figure 4.2 the calculations are shown for different ordering of the s- and p-doublet and varying three-body contribution (B_{3b}) to the total binding. From the calculations by Garrido it is very difficult to extract the ordering of the levels in the s-doublet (1^{-} and 2^{-}). Whereas it seems most likely that the p-state at $\sim$ 0.5 MeV is the 2^{+} and that the 1^{+} is situated around 0.35 MeV. This senario is shown in column c and d in the upper row (B_{3b}=350 keV) in figure 4.2. Furthermore this picture is consistent with the majority of the experimental data listed in table 4.1.

As mentioned in the paper by Garrido *et al.* most experimental observables are not very sensitive to the separation and ordering within the two doublets but only the sum energy of each doublet. Thus experiments which can extract spin and parity directly for different states are needed.

4.4 What do we want to learn about ^{10}Li?

The obvious thing that we want to learn about ^{10}Li is of course the ordering and separation of the four lowest lying s- and p-states, which would be of great importance in the theoretical calculations for the ^{11}Li properties.

Experimental information on the s- and p-states in ^{10}Li can be extracted in different ways as indicated in table 4.1. Another, and so far not exploited way, would be to make low energy transfer reactions of neutrons onto a ^{9}Li nucleus thus creating ^{10}Li via a simple one-nucleon transfer reaction. This way of populating levels in ^{10}Li is well studied through numerous low-energy transfer reactions to bound and unbound states performed during the past five decades (see eg compilation by [Sat83]).

The way to extract the spin-parity of the levels in ^{10}Li is "straightforward" in the sense that the method has been employed in many of the experiments mentioned above. The angular momentum transfer to the state can often be found, if the reaction is assumed to be direct, from the shape of the differential cross section (as discussed in section 2.2.1). With knowledge on the angular momentum transfer and J^{π} of the beam and target nuclei one can often extract spin and parity by angular momentum and parity conservation.

CHAPTER 5

Nucleon transfer reactions: ^{9}Li+^{2}H/^{9}Be

In this chapter I will introduce the data from the $^{9}Li+^{2}H$ and $^{9}Li+^{9}Be$ reactions performed at REX-ISOLDE in June 2002.
The method and results of the analysis of these data will be presented here together with an outlook concerning the remaining beam-time for this particular experiment.
This chapter represents the main part of my work during the last two years of my PhD.

5.1 Introduction

The ^{9}Li+^{2}H and ^{9}Li+^{9}Be experiments (IS367, see proposal at [IS367]) were performed at REX-ISOLDE in the summer of 2002 and the data from these reactions (especially ^{9}Li+^{2}H) have been the subject of my main (scientific) attention ever since.

This, our experiment at the newly constructed REX-ISOLDE post-accelerator, has in many ways been pioneering work in our collaboration since it is our first reaction experiment at such low energies and also because it is a new instrument at ISOLDE thus still experiencing many problems.

In this specific experiment at ISOLDE the ^{9}Li nuclei were produced in a 70 g/cm^2 Ta target, consisting of 13 rolls of 20 μm Ta foil which was bombarded with a pulsed 1.4 GeV proton beam on average every 2.4 s (3×10^{13} protons per pulse). The target was heated to 2100^{o}C for faster diffusion into the surface ion-source where the ^{9}Li atoms were ionized. The ^{9}Li^{1+} ions were extracted by a 30 kV electrostatic potential and mass separated in the GPS magnet after which an intensity of 1×10^{7} ^{9}Li per proton pulse was recorded. The ^{9}Li beam was then lead through the REX-ISOLDE post-accelerator, described in section 3.4, with a total efficiency about 1%. The main part of the loss occured at and in the REX-TRAP and REX-EBIS from injection and charge-state selection.

5.2 Experimental setup

In this experiment a fairly simple setup consisting of one DSSSD telescope and one small telescope was utilized.

The REX-ISOLDE 2.36 MeV/u (2.2% energy spread[1]) ^{9}Li^{2+} entered the detector area through a 4 mm diameter tungsten collimator before it was incident on the target. The targets were mounted on a ladder which could be moved so all 4 positions could be irradiated by the ^{9}Li beam. In the 2002 run targets of deuterated polypropylene and beryllium were used. The 6.4 μm thick deuterated polypropylene target ($(C_3D_6)_n$) had a deuterium purity of more than 95% and was irradiated for 30 hours (17 hours accepted for analysis with a total of 1.8×10^{9} ^{9}Li ions incident on target, see section 5.3.2). The impurities in the CD target were ^{1}H which introduced complications in the one-neutron pick-up channel, see section 5.3.3. The self-supporting CD target had a very uneven thickness varying up to $\pm$17% thus giving rise to roughly a 10% increase in the final experimental resolution. The thickness variation of the CD target was determined by measuring alpha particles, from a source, which had passed through the target

[1] That is 90% of the beam particles energy within $\pm$ 2.2% of the central energy.

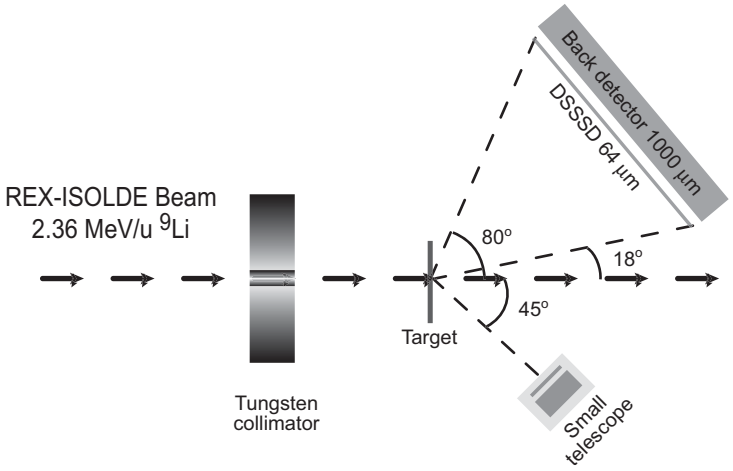

FIGURE 5.1: Sketch showing the detector setup with the DSSSD telescope and a small telescope on either side of the target position.

and then simulating energy loss and spread arising from different thickness variations (our simulations are described in appendix A). The self-supporting ^{9}Be target had a thickness of 5.2 μm and was irradiated for about 27 hours. Furthermore 7 hours of data with a ^{9}Li beam on an empty target holder was taken. In this data no events were seen thus assuring us that no background was present from scattering of the beam on the target holder and longlived radioactive activity in the reaction chamber.

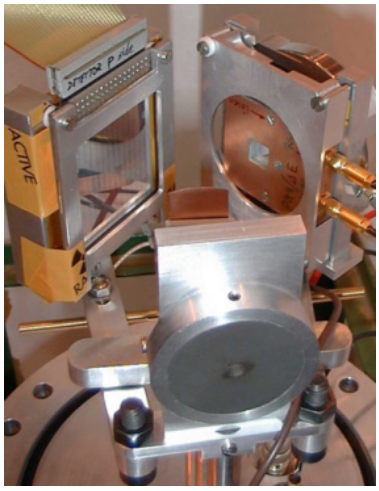

FIGURE 5.2: Photograph of the detector setup used in the transfer experiments.

After the target ladder a DSSSD-telescope was situated on the right side of the beam direction (seen from top) consisting of a 64 μm 16$\times$16 strip (5$\times$5 cm^2 total area) DSSSD and a 1000 μm Si-pad detector of same total area. The DSSSD-telescope covered from 18° to 80° and the distance to the point where the line-of-sight is perpendicular to the detector was 40.5$\pm$1.0 mm (this distance and the coordinate system of the DSSSD was determined by fitting the spatial distribution from a isotropic source placed at the target position). In figure 5.1 the main components of the detector setup is shown, and in figure 5.2 a photograph. The DSSSD-telescope

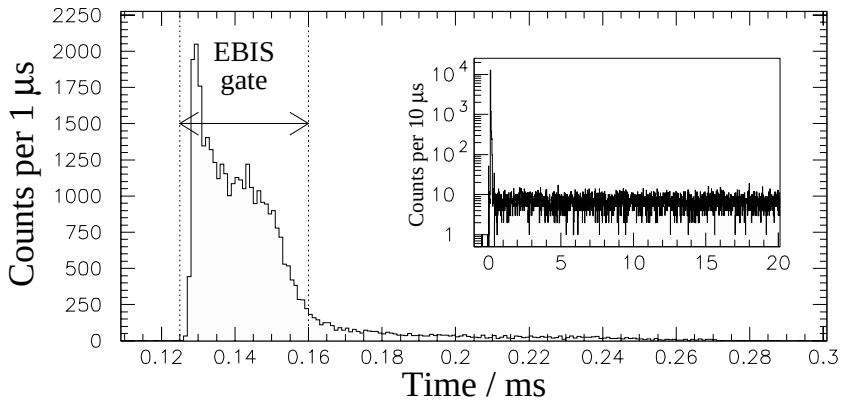

FIGURE 5.3: Time distribution of all events with respect to the extraction signal from the EBIS.

allows for unambigious identification of protons, deuterons, tritons and alpha-particles with higher energy than 2.5 MeV, 3.25 MeV, 3.75 MeV and 10.5 MeV respectivly. On the other side with respect to the beam direction a small three layered telescope (in the following the *small telescope*) was situated at 45° with an angular acceptance of about $\pm 7°$. The *small telescope* was composed of a 10 μm Si front detector backed by a 100 μm and 300 μm Si detector, all three with an active area of 100 mm^2. The very thin energy loss detector allowed for identification of alpha particles with energy as low as 3 MeV. Unfortunately the charge-one particles seen in the *small telescope* were not separable, most likely due to a large inherent capacitance.

5.3 ^{9}Li on ^{2}H target

In this part of the experiment the idea was to pick-up the neutron from ^{2}H onto ^{9}Li thus creating ^{10}Li. The idea was to feed l=0 states in ^{10}Li since the neutron in ^{2}H is in an $s_{1/2}$ state and the reaction energy so low that it would only allow for l=0 transfers. This has later been found not to be true since intrance channels with both l=0,1 are fed even at these low energies. Unfortunatly the ^{9}Li+^{2}H $\rightarrow$ ^{10}Li+p reaction has a threshold of 2.3 MeV, thus the remaining energy for exciting ^{10}Li is very limited (E_{CM}=3.86 MeV).

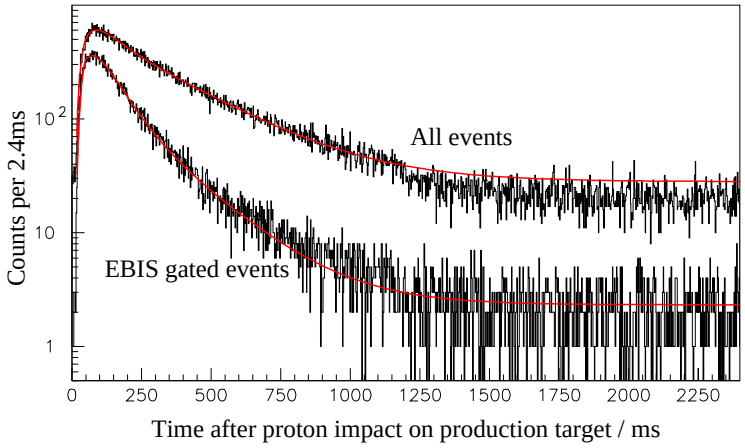

FIGURE 5.4: Time distribution of all events (upper curve) and events inside the EBIS gate (EBIS gated) from the ^{9}Li+^{2}H reaction. Lines are fits of the two time distributions (see text for detailes).

5.3.1 General characteristics of the ^{9}Li+^{2}H data

In figure 5.3 the time distribution of all events with respect to a signal generated when a pulse is extracted from REX-EBIS is shown. In the insert is shown the total time distribution which reveals a flat background, eg from the beta-decay of ^{9}Li, and a pronounced peak close to zero due to reactions in the target with the bunched REX beam. A zoom on the EBIS-peak is shown as the main part of figure 5.3 and shows that the peak contains some structure. The cut from 0.125 ms to 0.16 ms (EBIS gate) indicates what will be accepted as events arrising from reactions with the REX beam in the data analysis. As one can easily see this EBIS gate drastically reduces the non-reacting background since the time where data is accepted is reduced by a factor of 0.035 ms/20.4 ms$\simeq$1/600. An interesting observation has been that the ^{9}Li and the contaminant ^{18}O arrives at the setup with different time distributions with respect to the EBIS extraction signal. When comparing the events inside the EBIS gate with the events in the tail (0.16 ms to 0.26 ms) it is found that the tail contains up to an order of magnitude more ^{18}O relative to ^{9}Li. This effect is at the present time not fully understood, but it might be caused by the continous charge breeding of ^{18}O which is probably not trapped and thus not as spatially and timely (when extracted) confined as the ^{9}Li component.

In figure 5.4 is shown the time distribution after proton impact on the production target for *all events* and *EBIS gated events*. The data set of all events includes reactions and background, mostly from beta-decay of ^{9}Li which has

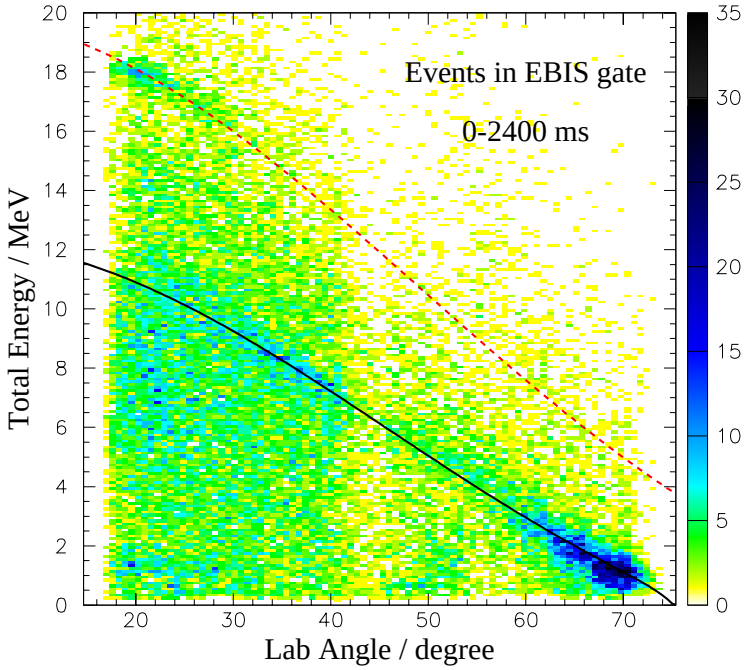

FIGURE 5.5: Total energy vs laboratory scattering angle for all events inside the EBIS gate. The black line indicates the position of elastically scattered deuterons and the dashed red line indicate the position of ^{9}Li scattered on ^{12}C.

been deposited in the reaction chamber. Whereas the EBIS gated events mainly arise from reactions in the CD target caused by the accelerated ^{9}Li beam. Thus the EBIS gated events should show a time structure composed of a release from the ISOLDE target-ionsource unit [Let97] (^{9}Li) plus a flat component (^{18}O). Conducting a fit of the EBIS gated events with an ISOLDE release time distribution

$$P = \frac{1}{N}(1 - \exp(-\lambda_r t))[\alpha \exp(\lambda_f t) + (1 - \alpha) \exp(-\lambda_s t)] \tag{5.1}$$

(see [Let97] for details) and a flat background the lower red line in figure 5.4 is found. This release, which tells us at which rate ^{9}Li is incident on the CD-target, can now be folded with an exponential decay to yield the time distribution of *all events*. A fit of *all events* with only a decay-constant, a flat background and normalization as free variables, is shown as the upper red line in figure 5.4. The resulting halflife for ^{9}Li is 173±5 ms in good agreement with the litterature value of 178.3±0.4 ms [Aud03]. In general one may note from the EBIS gated

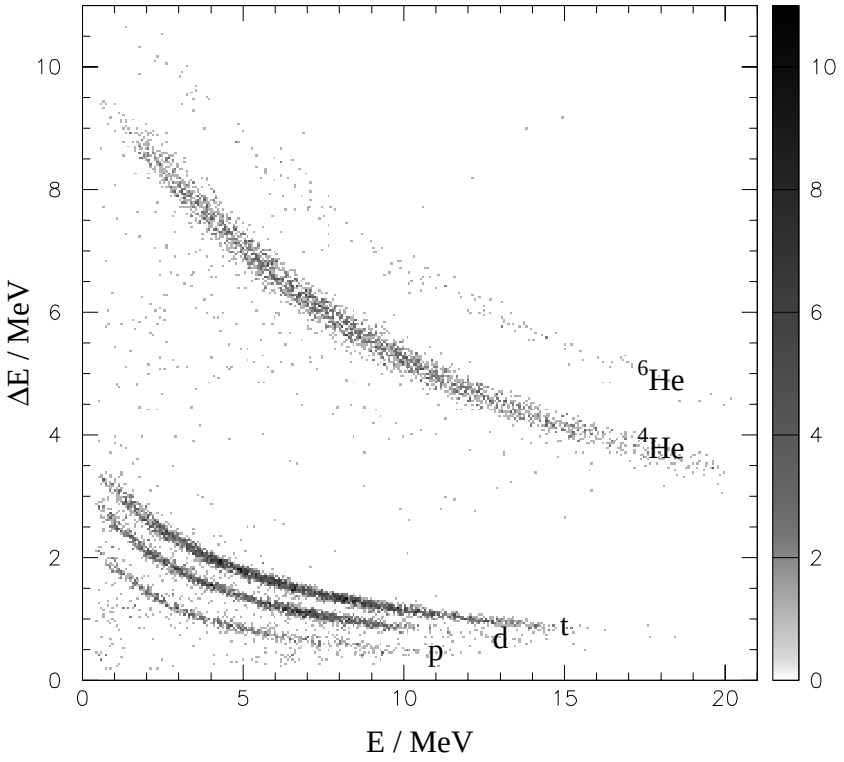

FIGURE 5.6: ΔE-Eplot for the products from the ^{9}Li+^{2}H reaction. In the plot both protons, deuterons, tritons, ^{4}He and ^{6}He are clearly identified.

time distribution that most reaction events are seen to arise from the ISOLDE beam (time distribution peak at short time) and a smaller flat background arising from ^{18}O restgas in the EBIS (see eg section 3.4). In figure 5.4 a small kink at 1200 ms (especially in *all events*) can be seen, this is due to the fact that not all proton pulses on the production target was separated by 2.4 s. By comparing the number of counts on either side of the kink at 1200 ms is has been found that approximatly 80% of the pulses was separated by 2.4 s or more.

Since most of the reaction channels are expected to be binary, ie two particles in both entrance and exit channel, the energy and angle of the outgoing particles are linked very closely, thus a total energy vs laboraty scattering angle plot should give information on the reaction channels. Such a plot of the total energy (energy-loss in DSSSD plus energy in back detector) vs laboratory angle for all events inside the EBIS gate and within the first 2400 ms after proton impact on production target is shown in figure 5.5. Unfortunately no clear structures are

seen in figure 5.5 except for elastically scattered deuterons (^{9}Li+^{2}H) indicated by a solid black line and elastically scattered ^{9}Li (^{9}Li+^{12}C) in the upper left corner indicated by a dashed red line. Furthermore figure 5.5 shows that data is missing in the region from 42-46° which is due to a malfunctioning front-strip in the DSSSD during the experiment.

Due to the very thin DSSSD (64 μm) it is possible to identify the reaction products by using the DSSSD and Si-pad detector as a telescope. In figure 5.6 the ΔE'-E' plot for the events within the EBIS gate and within the first 2400 ms after proton impact is shown. In figure 5.6 the following first order correction of the energy dependence of the energy-loss in the DSSSD has been performed

$$\begin{aligned} \Delta E' &= \Delta E \cos\theta \\ E' &= E + (1 - \cos\theta)\Delta E, \end{aligned} \tag{5.2}$$

where ΔE, E and θ are the measured energy-loss in the DSSSD, the energy measured in the Si-pad detector and the angle at which the particle penetrated the DSSSD, respectivly. Apart from the clear identification of the reaction products in figure 5.6 the low-energy cut-off is also found to be approximatly 2.3 MeV, 3 MeV, 3.5 MeV, 10 MeV and 11 MeV for protons, deuterons, tritons, alpha particles and ^{6}He. With the clear separation of the reaction products it is now possible to continue with a more detailed analysis of the specific reaction channels. This will be done in the folowing subsections where the reaction products will be analysed one at a time. Though counterintuitive I will start with the deuterons since they mainly arise from elastical scattering, and thus serves as normalization. In the following all events discussed will be events inside the EBIS gate.

5.3.2 Deuterons from the ^{9}Li+^{2}H reaction

In figure 5.7 the time distribution for all deuterons identified in figure 5.6 is shown. The time distribution is much like the total time distribution which shows both an ISOLDE beam and flat background component. The presence of a flat background component in the deuteron time distribution is very much expected since Rutherford scattering between ^{18}O and ^{2}H must occur.

In figure 5.8 two panels show the total energy vs laboratory scattering angle for all (0-2400 ms after proton impact) and late (1200-2400 ms after proton impact) deuterons. On both panels are shown lines indicating elastic deuteron scattering on ^{9}Li (solid black) and ^{18}O (dotted red). The panels in figure 5.8 clearly show that the deuterons mainly originate from elastic scattering plus a smeared out contribution at shorter times, which is most likely from compound reactions between ^{9}Li and ^{12}C. Especially the clearly visible shift in the band

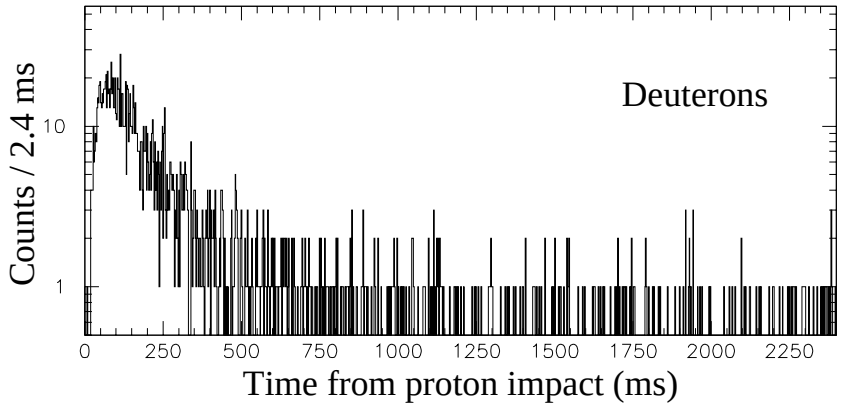

FIGURE 5.7: Time distribution of all deuterons from the ^{9}Li+^{2}H reaction.

of elastically scattered deuterons from all deuterons (mostly from ^{9}Li reactions) and late deuterons (mostly from ^{18}O reactions) gives good confidence in the data set, analysis method and understanding of the beam composition. Assuming that the deuterons arise exclusively from one reaction channel (^{9}Li+^{2}H $\rightarrow$ ^{9}Li+^{2}H or ^{18}O+^{2}H $\rightarrow$ ^{18}O+^{2}H) excitation energies can be extracted. In the upper panel in figure 5.9 the extracted excitation energy in ^{9}Li (assuming the ^{9}Li+^{2}H channel) for the early data (0-600 ms) is shown in solid black together with the late data (1200-2400 ms) in dashed black. This clearly shows that almost all deuterons

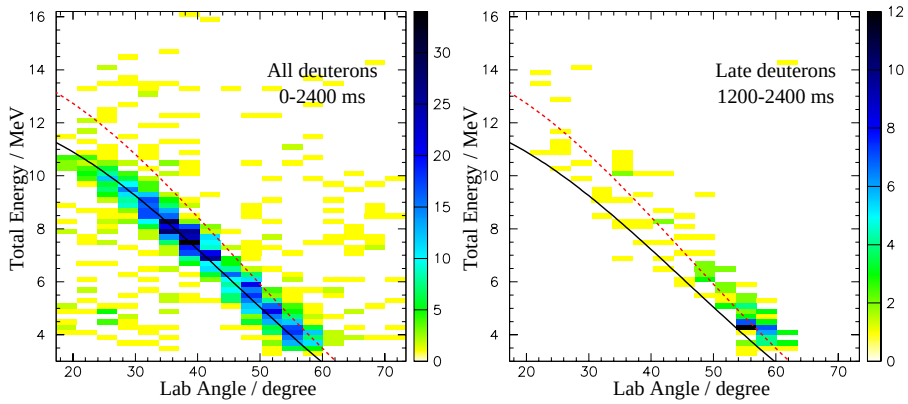

FIGURE 5.8: Total energy vs laboratory angle for all and late deuterons from the ^{9}Li+^{2}H reaction. The line indicates elastic deutron scattering from ^{9}Li (solid black) and ^{18}O (dotted red).

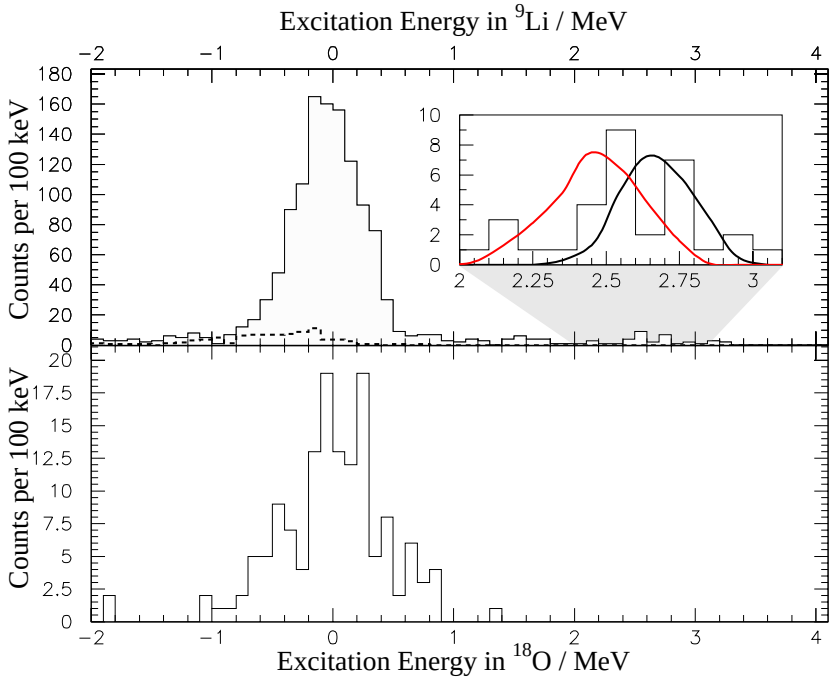

FIGURE 5.9: Extracted excitation energy for the deuteron channel. Upper panel: Excitation energy in ^{9}Li for early data (solid black) and estimated background (dashed black) and an insert high lighting possible excited states (see text). Lower panel: Excitation energy in ^{18}O for late data.

are elastically scattered and that the estimated background component in the first 600 ms from ^{18}O is very low. In the lower panel the excitation energy in ^{18}O is presented for the late data (assuming the ^{18}O+^{2}H channel) which comfirms that the background originates from elastic scattering of ^{18}O on ^{2}H. In the upper panel of figure 5.9 an insert shows an expansion of the excitation energy in ^{9}Li from 2 to 3 MeV, together with simulations of the 1st excited state in ^{9}Li (2.69 MeV, black) and the 2nd excited state in ^{9}Be (2.43 MeV, red). The 2nd excited state in ^{9}Be has been simulated using the cross-section found by A. Szczurek *et al* [Szc89] where the 2.43 MeV state in ^{9}Be was probed via 7 MeV deuterons. The simulation is based on a total of 0.3×10^{9} ^{9}Be nuclei incident on target whereas the ^{9}Li simualtion is adjusted to the data. Comparing the shape and position of the two simulations it seems unlikely that the events arise exclusively from ^{9}Be but rather that the main part is from the 1st excited state in ^{9}Li. Assuming that the ^{9}Be contamination originates from the decay of ^{9}Li in the REX-trap or REX-EBIS the fraction of ^{9}Be would roughly be 1% (^{9}Be could

in principle also originate directly from the ISOLDE target ion source, but this will not be taken into account since beryllium isotopes are difficult to ionize with a surface ion source). This comes about since the time for trapping and charge breeding is 20 ms, which is about 1/10 of the half-life of ^{9}Li, thus less than 10% of the ^{9}Li decays in the trap-EBIS unit of which only half decays to the ground-state of ^{9}Be. Most of these 5% will escape from the confining potentials since the ^{9}Be nuclei have higher recoil energy than the radial potential thus only on the order of 1% of ^{9}Be would be expected from decay of ^{9}Li. Based on these estimates and the argument about the excited states shown in the insert in the upper panel of figure 5.9, I will in the following assume that the early deuterons arise from ^{9}Li and a small contribution from ^{18}O.

To get the total amount of ^{9}Li incident on target the natural approach would be to compare the elastic cross-section to simulations of Rutherford scattering. To extract the elastic cross-section relative to Rutherford cross-section requires a few steps. The first step is to extract the center-of-mass (CM) angular distribution of the deuteron events in the elastic peak (-1.0 to 1.0 MeV) which is shown in the upper panel of figure 5.10 (note that the CM angles are with respect to the incomming ^{9}Li beam, ie Rutherford scattering of deuterons peak at 180°). The dashed line in the upper panel of figure 5.10 shows the total data in the first 600 ms whereas the solid line shows the data where the background from ^{18}O has been subtracted. The central panel shows a simulation of the CM angular distribution for deuterons Rutherford scattered on ^{9}Li. The simulation is based on 10^{9} ^{9}Li incident on target[2] which is close to the actual amount.

The lower panel in figure 5.10 shows the ratio between the background subtracted data and the simulated Rutherford scattering. In both upper and central panel more than the identified deuterons have been included since the events in the lower right corner of figure 5.5 mostly originates from elastically scattered deuterons. Thus a narrow cut containing most of the elastically scattered events stopped in the DSSSD has been added to the identified deuterons in this analysis. At first glance it seems as if the elastic cross-section relative to Rutherford cross-section (σ_{el}/σ_R) should be scaled down by a factor of ~ 4.5 if we assume that the σ_{el}/σ_R should be 1 at large angles. To get a more firm handle on the ^{9}Li normalization our collaborators, A.M. Moro and J. Gómez-Camacho [Mor04], have performed a fit of the extracted σ_{el}/σ_R using an optical model calculation (DWBA with the Fresco code). The optical model potential used consisted of a real part with Woods-Saxon shape, imaginary part with surface shape (Woods-Saxon derivative) and a spin-orbit term with surface shape radial part. The two

[2]The simulation has been performed with 10 times the statistics, and then scaled down by the same factor.

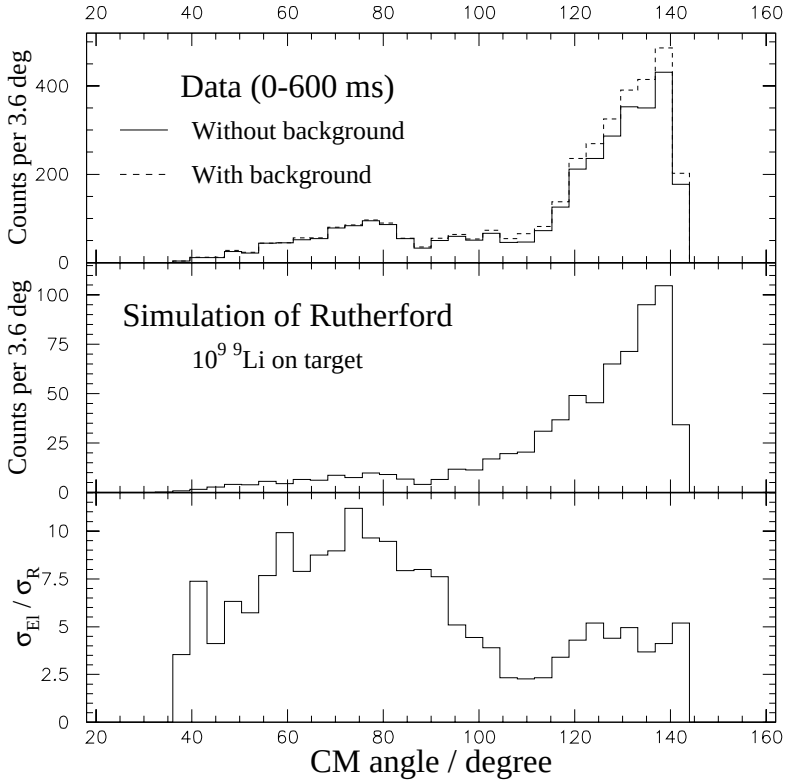

FIGURE 5.10: Upper panel: CM angle distributions for total early data (0-600 ms) (dashed line) and background subtracted data (soild). Center panel: CM angle distributions for simulated Rutherford scattering. Lower panel: Extracted total elastic to Rutherford cross-section. See text for further details.

best fits are shown in figure 5.11 and the fit parameters are tabulated in table 5.1 (the parameters labeled *fixed* were held fixed during the fit). From the optical potential fits a renormalization factor of 1.8 is found, that is 1.8×10^{9} ^{9}Li incident on target in total or 7×10^{4} per pulse (17 hours and one pulse per 2.4 s). The uncertainty on the amount of ^{9}Li in the beam is on the order of 10%. The calculations show that even at 120-140°, the regime where Rutherford scattering normally dominates, a large amount of nuclear elastic scattering is present.

In the ^{18}O case (1200-2400 ms) a similar calculation of the CM angular distribution and a simulation of the Rutherford scattering can be performed. From these calculations the angular distribution of σ_{el}/σ_R for the ^{18}O+^{2}H reaction can be extracted. See figure 5.12. Normalizing the amount of ^{18}O from the σ_{el}/σ_R

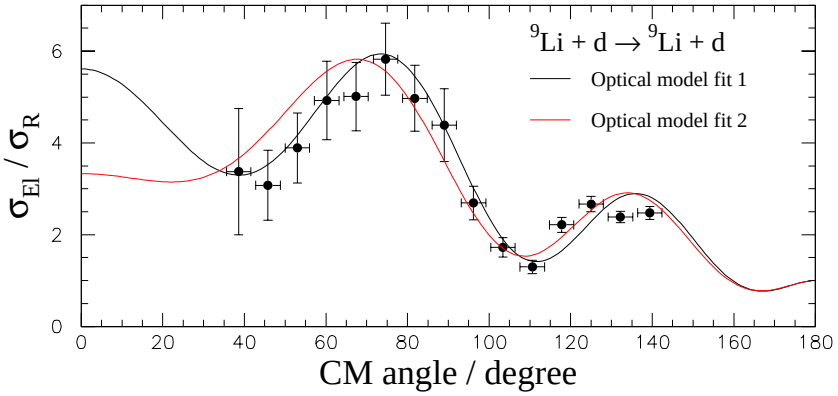

FIGURE 5.11: Renormalized σ_{el}/σ_R for the ^{9}Li+^{2}He channel. The black and red curves show optical potential fits of the data. See text and table 5.1 for more details.

might again be a matter of debate, but it has here been set to 1 at large angles (close to maximum Rutherford scatering). From earlier experiments on d+^{18}O elastic scattering by Stephenson *et al* [Ste79] (10 MeV deuterons) and Wickenberg *et al* [Wic63] (7 MeV deuterons) both show a clear destructive interference which, in form, is in agreement with the structure seen in figure 5.12. The ^{18}O elastic deuteron scattering relative to Rutherford scattering presented in figure 5.12 is based on a simulation of 0.14×10^{9} ^{18}O incident on target. The uncertainty on the normalization of the ^{18}O content in the beam is on the order of 20%

Parameter	Optical model fit 1	Optical model fit 2
V_{real}	104.6 MeV	134 MeV
r_0	1.2 fm (fixed)	1.0 fm (fixed)
a_0	0.65 fm (fixed)	0.64 fm
W_{imag}	12.4 MeV	12 MeV
r_i	1.2 fm (fixed)	1.0 fm (fixed)
a_i	0.65 fm (fixed)	0.72 fm
V_{ls}	6 MeV (fixed)	6 MeV (fixed)
r_{ls}	1.4 fm (fixed)	1.4 fm (fixed)
a_{ls}	0.7 fm (fixed)	0.7 fm (fixed)

TABLE 5.1: Parameters from the optical model fit of the elastically scattered deuterons.

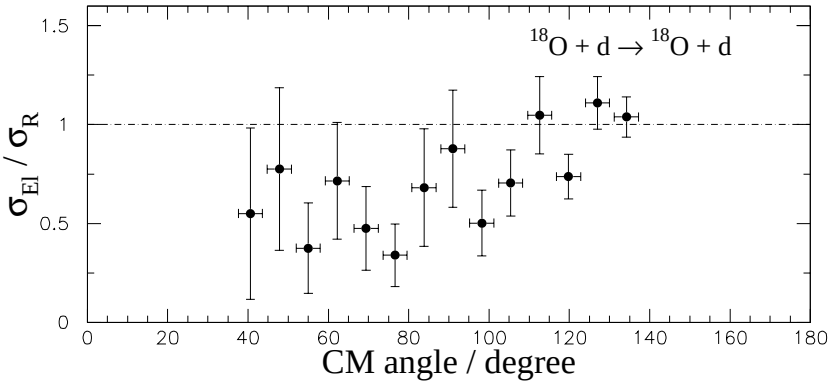

FIGURE 5.12: Extracted σ_{el}/σ_R for the ^{18}O+^{2}H elastic scattering reaction.

and could probably be made smaller if a DWBA calculation was performed.

Thus from the deuteron data the conclusion is that we have in total 1.8×10^{9} ^{9}Li (0-600 ms) and 0.13×10^{9} ^{18}O (1200-2400 ms) incident on target and a maximum of 20% ^{9}Be contamination, though the ^{9}Be contamination more likely is on the order of 1%. It would be appropriate to note that if a large ^{9}Be contamination was present this would decrease the total amount of ^{9}Li since elastically scattered deuterons from ^{9}Li and ^{9}Be are indistinguisable. Assuming, as discussed above, that the REX-ISOLDE beam mainly consists of ^{9}Li and ^{18}O the fraction of ^{18}O relative to ^{9}Li in the first 600 ms after proton impact on target would be about 4%.

5.3.3 Protons from the ^{9}Li+^{2}H reaction

In figure 5.13 the time distribution of the protons identified in figure 5.6 is shown. Again a strong ISOLDE component is present on a small flat background.

In the case where protons are detected in the DSSSD telescope one should keep in mind that the ^{1}H contamination in the CD target will produce elastically scattered protons in addition to the expected protons produced in (d,p) reactions. The total energy vs laboratory angle plots for all (0-2400 ms) and late (1200-2400 ms) protons are shown in the left and right panels of figure 5.14. In the panels lines indicating the position of protons originating from certain levels are shown: In the left panel, showing all protons, the reaction channels;

^{9}Li+^{2}H → ^{10}Li(0.35 MeV)+p	in solid black
^{9}Li+^{1}H → ^{9}Li(gs)+p	in dashed red
^{9}Li+^{12}C → ^{20}O(18 MeV)+p	in dotted blue

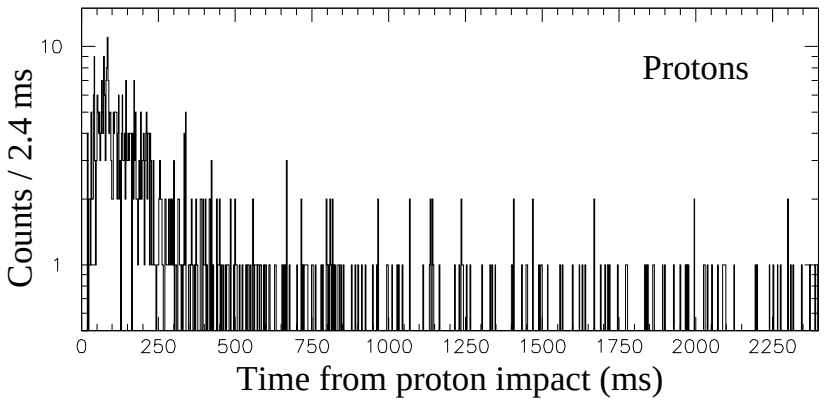

FIGURE 5.13: Time distribution of all protons from the ^{9}Li+^{2}H reaction.

are shown. In the right panel, showing the late protons, the reaction channels;

^{18}O+^{1}H $\rightarrow$ ^{18}O(gs)+p	in solid green
^{9}Li+^{1}H $\rightarrow$ ^{9}Li(gs)+p	in dashed red
^{18}O+^{2}H $\rightarrow$ ^{19}O(gs)+p	in dotted purple (upper)
^{18}O+^{2}H $\rightarrow$ ^{19}O(1.47 MeV)+p	in dotted purple (lower)

are shown. In the left panel of figure 5.14 two weak lines are visible in the lower left corner on a more or less smeared out background. The two lines coincide with elastically scattered protons shown by the red line (contamination in the deuterium target) and events which could originate from a state at 350 keV excitation energy in ^{10}Li. The dotted blue line in the left panel indicates the trend for protons emitted from the compound nucleus reaction ^{9}Li+^{12}C $\rightarrow$ ^{21}F*. In the right panel no clear structures are seen though it seems as if elastic scattering of protons in the target is present (solid green), which again has a shift compared to ^{9}Li + ^{1}H elastic scattering (dashed red) as in the deuteron case. The remaining data in the right panel seems to originate from states in ^{19}O populated in the one neutron transfer.

The shift between the positions of ^{9}Li and ^{18}O elastic proton scattering, which agrees with data, was one of the features that confirmed that it is elastic proton scattering and not excited states in the ^{9}Be+^{2}H $\rightarrow$ ^{10}Be+p reaction around 6 MeV excitation energy (these levels should also have a very large cross-section to give rise to so many events). The hypothetis that the data indicated with dashed red in the left panel in figure 5.14 arise from elastic scattering and not excited states in ^{10}Be is further supported when the excitation energy in ^{9}Li and ^{10}Be

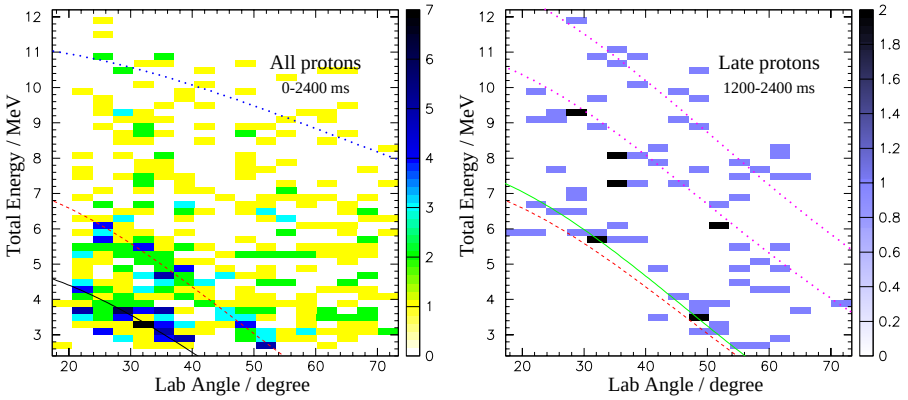

FIGURE 5.14: Total energy vs laboratory angle for all and late protons from the ^{9}Li+^{2}H reaction. The lines indicates positions for specific channels. See text for details.

are extracted from the proton data since the corrsponding peak is narrower in the ^{9}Li excitation energy spectrum. Furthermore, if ^{9}Be was present in larger quantities in the ISOLDE beam, the reaction channel leading to the ground state in ^{10}Be (^{9}Be + ^{2}H $\rightarrow$ ^{10}Be + p) should be visible in the excitation energy spectrum for ^{9}Li+n system around -7 MeV. The few counts present around -7 MeV excitation energy in ^{9}Li+n system seen in figure 5.15 set an upper limit of about 10-20% ^{9}Be contamination from previous measured cross section [Pow70]. All data are therefore consistent with a negligible ^{9}Be beam component, hence I will not consider this possibility further.

The extracted excitation energy in the ^{9}Li+n system assuming that all early protons (0-600 ms) arise from ^{9}Li on ^{2}H is shown in figure 5.15. Note that most of the events are below zero excitation energy, thus excluding that they arise from the ^{9}Li+^{2}H channel. In figure 5.15 the background estimated from the late proton events (1200-2400 ms) is indicated by a red line. The background only has a contribution below zero excitation energy, and will therefore not influence possible events corresponding to states in the ^{9}Li+n system. The black line in figure 5.15 correspond to the three different contributions discussed above; a state in ^{9}Li at 350 keV (peak above zero), elastically scattered protons on ^{9}Li (peak just below zero) and a compound contribution from ^{9}Li on ^{12}C (hatched area). The compound contribution has been estimated by equation 2.4 with the parameters discussed in the same section. Here the binding energies of the involved nuclei are in our favour since the compound contribution only is present below zero excitation energy. The elastic peak has been simulated, and gives an estimate of the experimental resolution for this channel. The ^{10}*Li peak* (events from 0-1 MeV

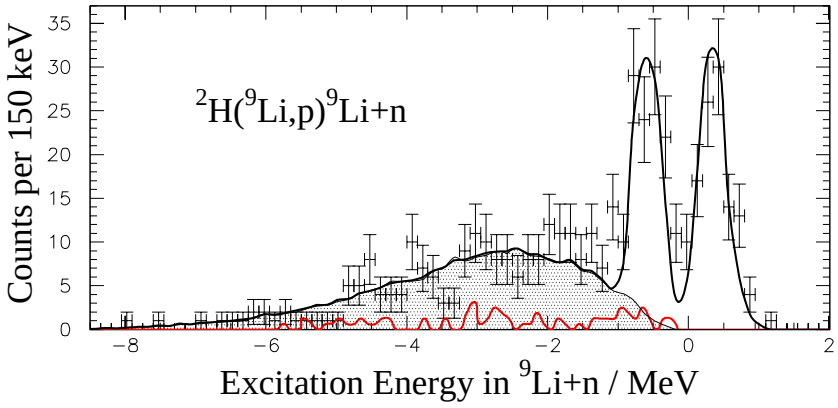

FIGURE 5.15: Extracted excitation energy in the ^{9}Li+n system superimposed with calculation (black) and estimated background (red).

in figure 5.15) has been simulated based on an R-matrix calculation[3] with the same values as obtained in a recent experiment with the same reaction, ^{9}Li+^{2}H $\rightarrow$ ^{10}Li+p, with 20 MeV deuterons by P. Santi *et al* [San03] where a *bump* at 350 keV with a width of $\sim$ 300 keV was observed.

The excitation energy in ^{19}O can of course also be extracted, but the spectrum does not show any interesting structures apart from weak indications of the two levels in ^{19}O plotted in dotted purple in the right panel if figure 5.14, and the elastically scattered protons, and will thus not be shown.

By selecting the events above zero excitation energy (0-1 MeV) in figure 5.15 the CM angular distribution for these ^{10}*Li events* can be extracted. The acceptance of the detector setup for protons from a 350 keV state in the ^{9}Li+n system can be extracted by simulating a uniform angular distribution for protons with the correct energy angular correlations. From the simulated acceptance per reacting ^{9}Li, the number of target nuclei, the number of incident ^{9}Li and the total CM angular distribution of the ^{10}*Li events* it is now possible to extract the absolute differential cross-section for the ^{10}*Li events*. The extracted differential cross-section is shown in figure 5.16 with a systematic error on the normalization of about 20%. Due to the limited angular coverage in this case it is not very easy to extract much information based on the differential cross-section, though some structure is visible. Theoretical calculation based on an optical model are currently being performed by A.M. Moro and J. Gómez-Camacho [Mor04]. Ex-

[3]That is the calculation includes the change in phase-space with energy over the threshold when calculating of the shape of excitation energy, as described in section 2.2.3.

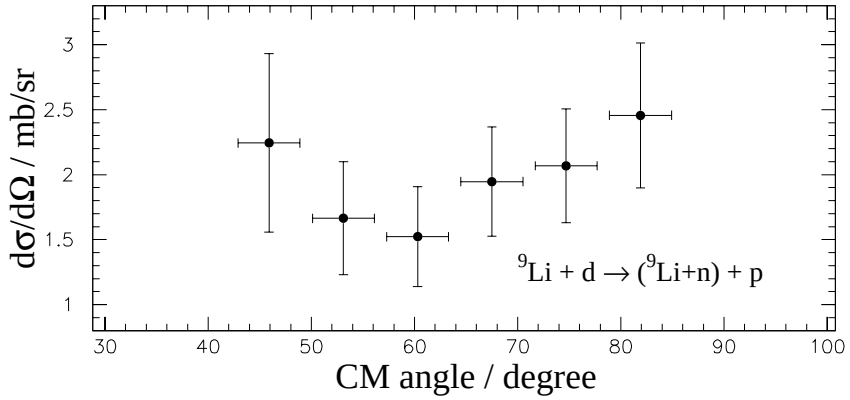

FIGURE 5.16: Extracted differential cross-section for the ^{10}*Li events* (0-1 MeV excitation energy in figure 5.15) from the ^{9}Li+^{2}H reaction.

traction of the spin of the possible state seen at roughly 350 keV from the shape of the excitation energy spectrum is unfourtunatly not possible in the R-matrix framework, since one particular shape can easily be obtained by assuming either a s- or p-state, as was already pointed out by McVoy and van Isacker for the^{10}Li case [McV94].

It should be noted that the proton energy range accessible in the ^{9}Li+^{2}H reaction at 2.36 MeV/u does not extend to much higher excitation energies in the ^{9}Li+n system than 1.-1.5 MeV. This should serve as a reminder not to trust too much the upper tail of the ^{10}*Li events* since acceptance artifacts might play a role. But some clarification should be reached with the pending repetition of the experiment at 3.1 MeV/u (hopefully in the spring of 2005).

In conclusion, the proton data seems to be well understood since a structure $\sim$ 350 keV above the ^{9}Li+n system has been observed, which is in very nice agreement with a similar experiment by P. Santi *et al* [San03]. In spite of the limited beam time and moderate ^{9}Li beam it seems as if this first attempt to populate states in the ^{9}Li+n system was succesfull. It will be very interesting to see the results of the remaining beam time for this experiment where, hopefully, a stronger ^{9}Li beam and better optimized detector setup will be available.

5.3.4 Tritons from the ^{9}Li+^{2}H reaction

In figure 5.17 the time distribution of the tritons identified in figure 5.6 is shown. This shows that all tritons originate from the ISOLDE beam, thus the triton events are very clean without any ^{18}O background component.

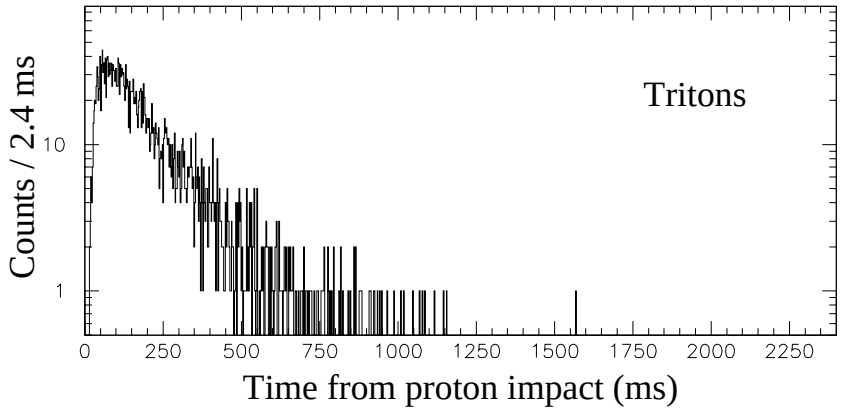

FIGURE 5.17: Time distribution of all tritons from the ^{9}Li+^{2}H reaction.

Since only one triton event is present after 1200 ms in figure 5.17, only *all events* (0-2400 ms) will be presented in figure 5.18 of the total energy vs laboratory angle plot. The total energy vs laboratory angle in figure 5.18 for the triton events seems to be very clean, as the data can be described purely by ^{9}Li+^{2}He $\rightarrow$ ^{8}Li+t, where ^{8}Li is fed in both the ground state, 1st excited state (0.9808 MeV), 2nd excited state (2.255 MeV) and 3rd excited state (3.21 MeV) (see level scheme for ^{8}Li in left part of figure 5.20). The four lines on figure 5.18 indicates the positions of these four states in ^{8}Li (lowest excitation energy in the nucleus corresponds to highest proton energy in figure 5.18). As in the

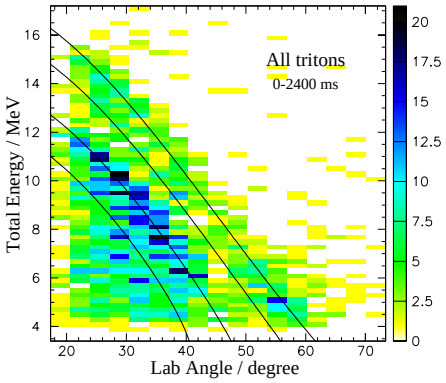

FIGURE 5.18: Total energy vs laboratory angle for all tritons from the ^{9}Li+^{2}H reaction. The lines indicates kinematics of levels in the residual nucleus ^{8}Li.

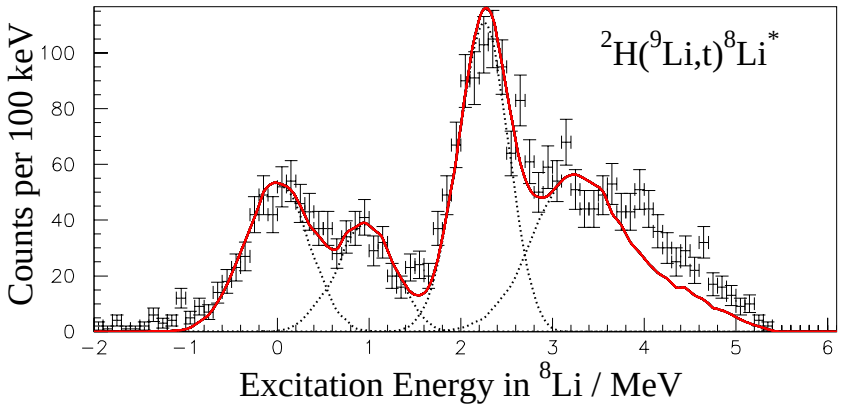

FIGURE 5.19: Extracted excitation energy in ^{8}Li superimposed with calculation (black lines) of ground state and the first three excited states in ^{8}Li.

previous cases the excitation energy in the residual nucleus, ^{8}Li, has been extracted assuming a binary reaction between ^{9}Li+^{2}He. This is shown in figure 5.19. The dotted curves on figure 5.19 are simulations of the four lowest known states in ^{8}Li, the three lowest just simulated as delta-functions and the fourth by an R-matrix calculation. All simulations are based on literature values for the levels in ^{8}Li [Ajz88] (see left part of figure 5.20), thus only the weight of the four peaks has been fitted to obtain the solid red curve. The red curve in figure 5.19 confirms that the triton events originates from ^{9}Li+^{2}H $\rightarrow$ ^{8}Li+t, since the complete data set is described almost perfectly by the ground state and first three excited states in ^{8}Li. The only discrepency seen between data and simulation occurs above 3-4 MeV where the tail of the data seems to be larger than predicted. Several possible explanations for this exists. Firstly, it may be due to the poor knownledge on the position and width of the third excited state, though this is not very likely since the data above 3 MeV seems to exhibit another structure than the one an R-matrix calculation would give. Secondly, it may be the interference between the 1^{+} state (third excited state) and fourth excited state at 5.4 MeV which might also be a 1^{+} state, though again the structure in the data above 3 MeV does not point in this direction. Thirdly, it might be due to states which should be present in the low energy end of the excitation energy spectrum (see subsequent paragraph), but has previously not been observed in other experiments.

The lowest shell model filling of ^{8}Li gives an unpairred proton and neutron in the $p_{3/2}$ orbit (see black circles in the right part of figure 5.20) which can

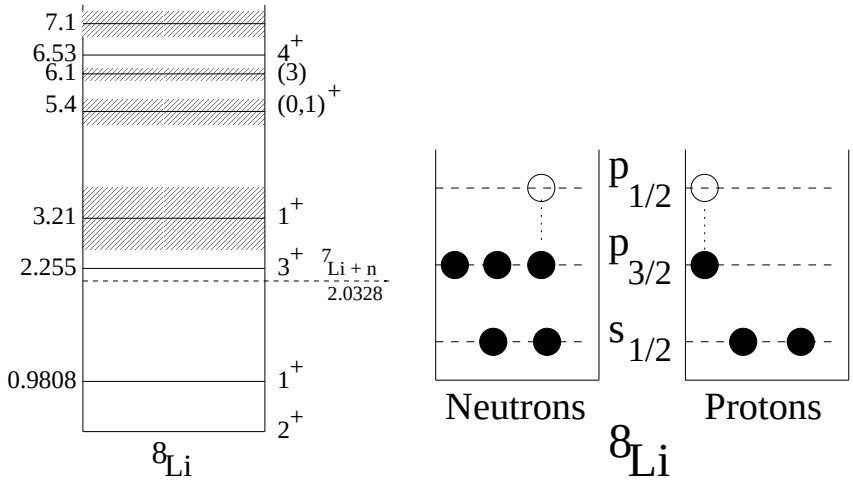

FIGURE 5.20: Left: The experimentally established level scheme for ^{8}Li (values from [Ajz88]). Right: Scheme showing the shell model filling of the levels in ^{8}Li.

couple to 0^+, 1^+, 2^+ and 3^+. These first four states should therefore be found as the four lowest in the excitation energy spectrum of ^{8}Li. The left part of figure 5.20 shows the 2^+ as the ground state and 1^+ and 3^+ as first and second excited states in ^{8}Li, but a 0^+ state is missing. The next states in the excitation energy spectrum of ^{8}Li then arise from an excitation of either the unpairred proton or neutron into the $p_{1/2}$ level (shown as open circles in the right part of figure 5.20) which then returns a 1^+ and 2^+ level, each (coupling of $p_{3/2}$ and $p_{1/2}$). This is the origin of the third excited (1^+) state at 3.21 MeV. Recent *ab initio* calculations by Wiringa *et al* suggest that the 0^+ state should be located around

J^π	Exp/MeV	CK/MeV	VMC/MeV	Spec. Fact.(CK)	Spec. Fact.(VMC)
2^+	0	0	0	**0.885** / 0.012	**0.966** / 0.114
1^+	0.98	1.08	1.1	**0.355** / 0.061	**0.457** / 0.009
0^+	not obs.	4.95	2.3	**0.1018** / -	**0.007** / -
3^+	2.26	1.69	3.3	**1.330** / -	**0.911** / -
1^+	3.21	2.77	3.5	0.035 / **0.088**	0.002 / **0.030**
2^+	not obs.	4.24	3.8	0.047 / **0.296**	0.014 / **0.107**

TABLE 5.2: Theoretical calculations of excitation energy and spectroscopic factors for states in ^{8}Li [Kur04, Wir04]. The spectroscopic factor are tabulated as SF($p_{3/2}$) / SF($p_{1/2}$).

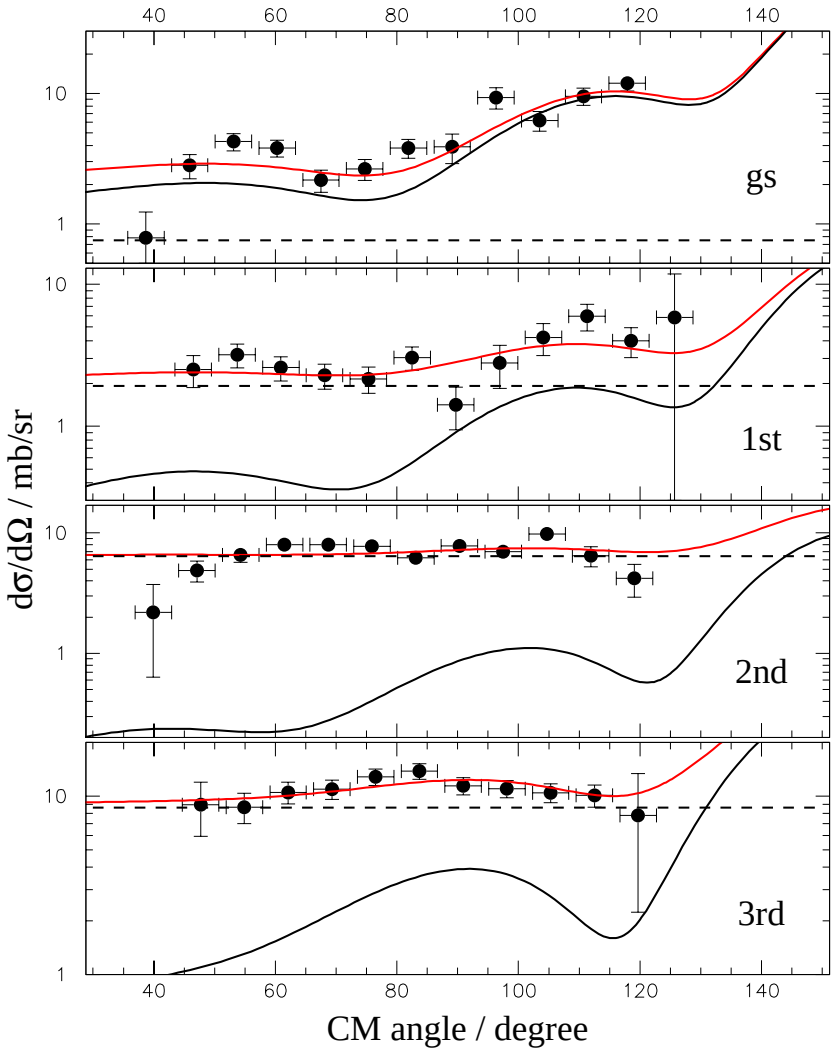

FIGURE 5.21: cross-section for the four lowest states in ^{8}Li. The red line shows best fit of data to DWBA calculation (solid black) plus flat compound contribution (dotted black). See text for details.

2-3 MeV excitation energy in ^{8}Li (2.83 MeV [Wir00] and 2.3 MeV [Wir04]), whereas shell model calculations based on the 1p shell interactions by Cohen and Kurath [Coh65, Coh67] predict the 0^{+} to be situated around 4.95 MeV [Kur04]. In table 5.2 the complete calculations of excitation energy and spectroscopic factors from Wiringa (VMC) and Kurath (CK) [Wir04, Kur04] are shown. The

Parameter	^{8}Li+t potential	Triton binding potential
V_{real}	142 MeV	57.5 MeV
r_0	1.16 fm	1.5 fm
a_0	0.78 fm	0.5 fm
W_{imag}	12.0 MeV	-
r_i	1.88 fm	-
a_i	0.61 fm	-

TABLE 5.3: Optical model parameters for the ^{8}Li+t [Pow70] and triton binding potential. For the triton binding potential only the depth was fitted to obtain correct binding energy.

spectroscopic factors in table 5.2 are written as SF($p_{3/2}$) / SF($p_{1/2}$).

The CK and VMC spectroscopic factors in table 5.2 clearly follow the picture described above about the grouping of the levels by spin-parity. Furthermore they suggest that the 2^+ state from the one-particle one-hole excitation should be situated around 4 MeV. This 2^+ state might also explain the discrepancy between data and calculations at higher excitation energy in figure 5.19. But before proceding to look after new states in ^{8}Li it would make sense to look at the extracted differential cross-sections for the four levels seen in figure 5.19. By making selections in the excitation energy of ^{8}Li the cross-section for the ground state (-0.6 to 0.4 MeV), 1st excited state (0.7 to 1.4 MeV), 2nd excited state (1.7 to 2.7 MeV) and the 3rd excited state (2.9 to 4.2 MeV) can be extracted. In all four cases the estimated contamination from neighbouring states is less than a few % (except for the 2nd excited state which has about 10% contamination from the 3rd excited state). The resulting differential cross-sections, corrected for acceptance, are shown in figure 5.21 superimposed with DWBA calculations by A.M. Moro and J. Gómez-Camacho [Mor04]. The latter have been performed with the ^{9}Li+d potentials extracted from the elastic scattering data, a ^{8}Li+t potential adobted from [Pow70] (Woods-Saxon real part, Woods-Saxon derivative imaginary part and no spin-orbit part) and a triton potential where the depth was fitted to give the correct binding energy of the triton (only real Woods-Saxon potential). The paramaters for the ^{8}Li+t and triton binding potentials are listed in table 5.3. Interestingly the *optical model fit 2* data for the ^{9}Li+d potential in table 5.1 gives very bad agreement with data whereas the *optical model fit 1* is in resonable agreement. Therefore only calculations based on the *optical model fit 1* is presented in figure 5.21.

The calculated cross-sections have been fitted to the data with a scaling factor plus an angular independent component to give a first order estimate of the

State in ^{8}Li	Spec. Fact. (w. comp.)	Spec. Fact. (w.o. comp.)
gs	4.2	5.2
1st	0.8	2.4
2nd	0.7	6.5
3rd	2.5	9.5

TABLE 5.4: Spectroscopic factors for excited states obtained from fit with and without a first order compound contribution.

compound contribution. The obtained values are listed in table 5.4. This indeed is not in very good agreement with the calculated spectroscopic factors in table 5.2. This disagreement might be due to the limited inclusion and understanding of the compound contribution which at these low energies have been seen earlier to play a significant role, eg in ^{9}Be+d at 2.5 MeV/u [Pow70]. In general it seems that the compound contribution has been seriously underestimated in this very simple approach.

Concerning the compound contribution it seems, both in the fit but also in the disappearence of structure in the angular distribution, that at higher excitation energy a larger fraction of the cross section must be attributed to compound reaction compared to direct reaction mechanism. This is the same general picture as discussed in the introductory section 2.2 about direct vs compound reactions. Especially in figure 2.5 where it is shown how particles emitted at low and high energy correspond to compound and direct reactions, respectly. In our case the spectrum shown in figure 2.5 would be squeezed very much together which indicates that direct and compound reactions will mix. Still, it seems as if the systematics of more compound contribution at lower particle emission energy (higher excitation energy) is present in the triton data. It should be noted that ^{11}Be, containing only 11 nucleons, should probably not be called a compound nucleus, but it still seems as if the general trends hold true even for this small system.

Returning to the level scheme and spectroscopic factors calculated by Wiringa *et al* [Wir04] we might use this information to get a better understanding of the experimental data for ^{8}Li. First of all, it should be noted that the missing 0^{+} state at low excitation energy has a very small spectroscopic factor, and is predicted to be situated where the spectrum already is very rich, thus it will be very difficult to acces this state via the ^{9}Li+^{2}H reaction. Furthermore one of the 2^{+} states from the one-nucleon excitations is predicted to be situated just below 4 MeV, which coincides with the discrepency between calculations and data in figure 5.19. To

include a 2^{+} around 4 MeV with a width similar to the 3.21 MeV state (ie $\sim$ 1 MeV) could probably solve the discrepancy between calculation and data in figure 5.21. But due to the poor statistics and the limited angular resolution this will not be attempted here. Hopefully it will be possible to present more decisive results when the next beam time of the ^{9}Li+^{2}H have been performed at higher beam energy (3.1 MeV/u) and with an improved angular resolution.

In general the conclusion for the triton data is that they are very clean and well understood, though the differential cross-sections seem to be dominated by a compound contribution. If the up-coming experiment at REX-ISOLDE in 2005 confirms a state around 4 MeV the data would be in very good agreement with the calculations of Wiringa *et al* [Wir04] in table 5.2.

5.3.5 ^{4}He and ^{6}He from the ^{9}Li+^{2}H reaction

In the upper and lower panel of figure 5.22 the time distribution of the ^{4}He and ^{6}He events identified in figure 5.6 is shown, respectivly. From the upper panel in figure 5.22 it is evident that the ^{4}He events, as the tritons, arise from the ISOLDE beam and has at most a very weak background from ^{18}O. In the ^{6}He case the same picture seems to hold true, though the statistics is very poor. Therefore I will only consider *all evente* ^{4}He and ^{6}He in the following data analysis.

In the left panel of figure 5.23 is plotted the energy vs laboratory scattering angle for all identified ^{4}He events from 0-2400 ms after proton impact on target. Superimposed on this figure are curves indicating the position of the ground state, 2st and 3nd excited state in ^{7}He (0.0, 2.92 and 5.8 MeV)[4] from the reaction ^{9}Li+d (solid black) and a hypothetical level at 10 MeV excitation energy in ^{17}N from the reaction ^{9}Li+^{12}C forming the compound nucleus ^{21}F (dashed blue).

From the left panel of figure 5.23 it is seen that the majority of the ^{4}He events can be assigned as comming from ^{9}Li on ^{2}H plus a smaller contribution from the ^{9}Li on ^{12}C reaction forming the compound nucleus ^{21}F.

In the right panel of figure 5.23 the energy vs laboratory scattering angle is shown for all identified ^{6}He events. In this figure curves indicate the position of the ground state and 1st excited (1.27 MeV) state in ^{5}He from the reaction ^{9}Li+^{2}H (solid black) and a hypothetical level at 5 MeV excitation energy in ^{17}N from the reaction ^{9}Li+^{12}C (dashed blue). It is clear that most of the ^{6}He events originate from ^{9}Li on ^{2}H (^{9}Be on ^{2}H is energetically forbidden) with a few events coming from the reaction ^{9}Li on ^{12}C forming the compound nucleus ^{21}F. A similar result as seen for the ^{4}He and tritons.

In the two previous subsections it has become clear that most reaction prod-

[4] A state at 0.57 has resently been proposed to exist in ^{7}He [Mei02].

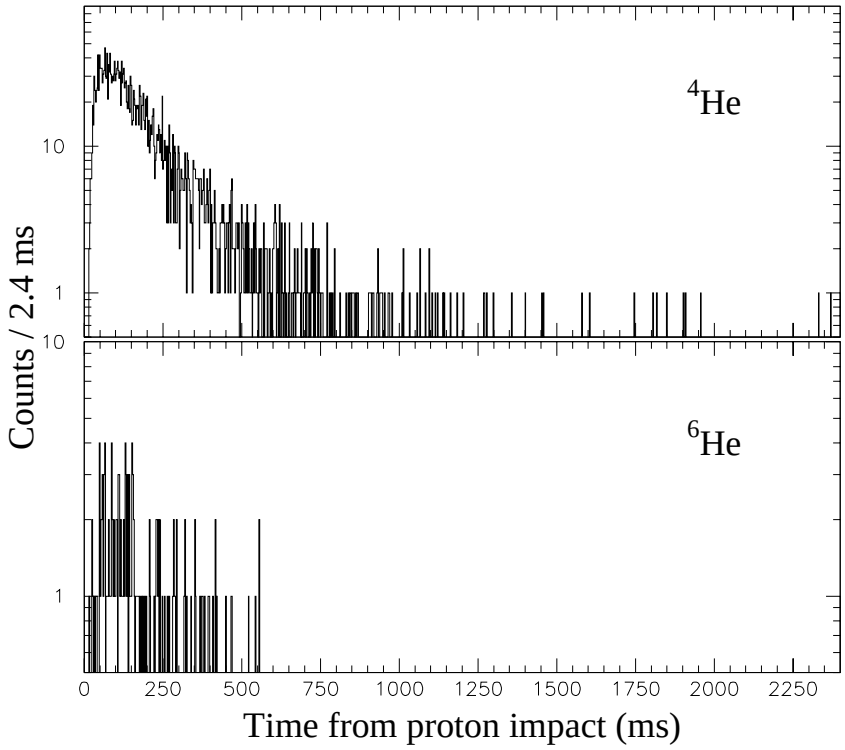

FIGURE 5.22: Time distribution of all ^{4}He and ^{6}He events from the ^{9}Li+^{2}H reaction shown in upper and lower panel, respectivly.

ucts come from ^{9}Li incident on deuterons. If we assume the reaction to go through the 2-body channels (1) and (2)

$$^{9}\mathrm{Li} +^{2} \mathrm{H} \rightarrow \begin{cases} ^{4}\mathrm{He} +^{7} \mathrm{He} & \rightarrow \; ^{4}\mathrm{He} +^{6} \mathrm{He} + n & (1) \\ ^{5}\mathrm{He} +^{6} \mathrm{He} & \rightarrow \; ^{4}\mathrm{He} + n +^{6} \mathrm{He} & (2) \\ ^{4}\mathrm{He} +^{4} \mathrm{He} + 3n & & (3) \end{cases}$$

and not to the 5-body channel (3), the ratio between ^{4}He and ^{6}He should be close to one[5]. But what is evident from the coincidences between the *small telescope* and the DSSSD is that very few ^{4}He-^{6}He coincidences are observed, whereas many ^{4}He-^{4}He coincidences are seen (the ratio is $\sim$ 1/20 see middle part and dashed line in bottom of figure 5.24). This shows that a substantial amount of the heavy helium isotopes produced in the first step of the reaction

[5]Except for small deviations due to different acceptance of the two nuclei.

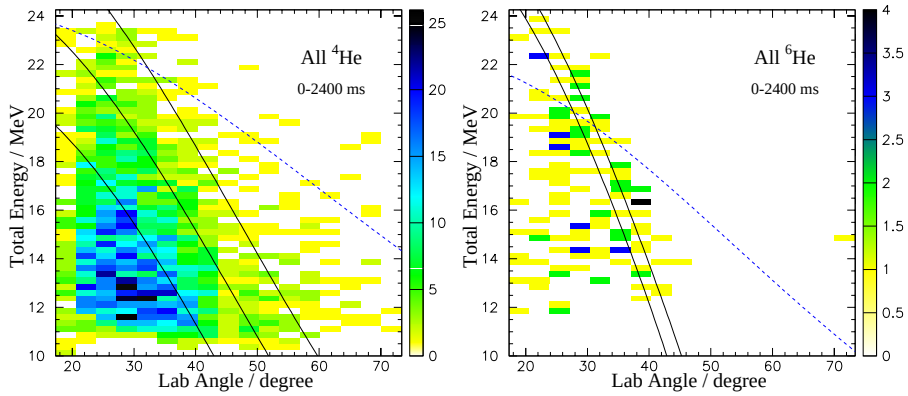

FIGURE 5.23: Total energy vs laboratory angle for all and late protons from the ^{9}Li+^{2}H reaction. The lines indicates positions specific channels. See text for details.

subsequently decay to ^{4}He before being detected, a fact also apparent from the relative numbers of ^{4}He and ^{6}He in the upper and lower panels of figure 5.22, respectively. In all cases this results in at least a 3-body channel either directly or via the breakup of the unbound reaction product; ^{5}He or ^{7}He. Since at most two outgoing particles are detected, a detailed description of the data would include model assumptions and I shall refrain from attempting this. However, it should be noted that in spite of the many-body final state the lines corresponding to the levels calculated assuming 2-body final state seem to describe the data in both panels of figure 5.23 surprisingly well. This indicates that an initial 2-body break-up occurs followed by neutrons being emitted at low energy to form the 3- or 5-body final state. Therefore it seems resonable to conclude that the neutrons do not change the angle and energy per nucleon significantly.

For events where two fragments are detected in coincidence between the DSSSD and the small telescope the missing energy can be reconstructed from the beam energy and the Q-value of the reaction. The reconstructed energy for the coincidences is shown in figure 5.24. The upper frame shows the coincidences between tritons in the small telescope and all events in the DSSSD. The middle frame shows the coincidences between ^{4}He in the DSSSD and ^{4}He in the small telescope. The lower frame shows the coincidences between ^{4}He in the DSSSD and ^{6}He in the small telescope (solid line) and vice versa (dashed line).

The spectrum of missing energy for the ^{8}Li+triton final state is consistent with the spectrum of the excitation energy in ^{8}Li (compare the lower part of figure 5.19). Note that the kinematical acceptance for coincidences favours the lower excitation energies. This demonstrates that the coincidence technique is

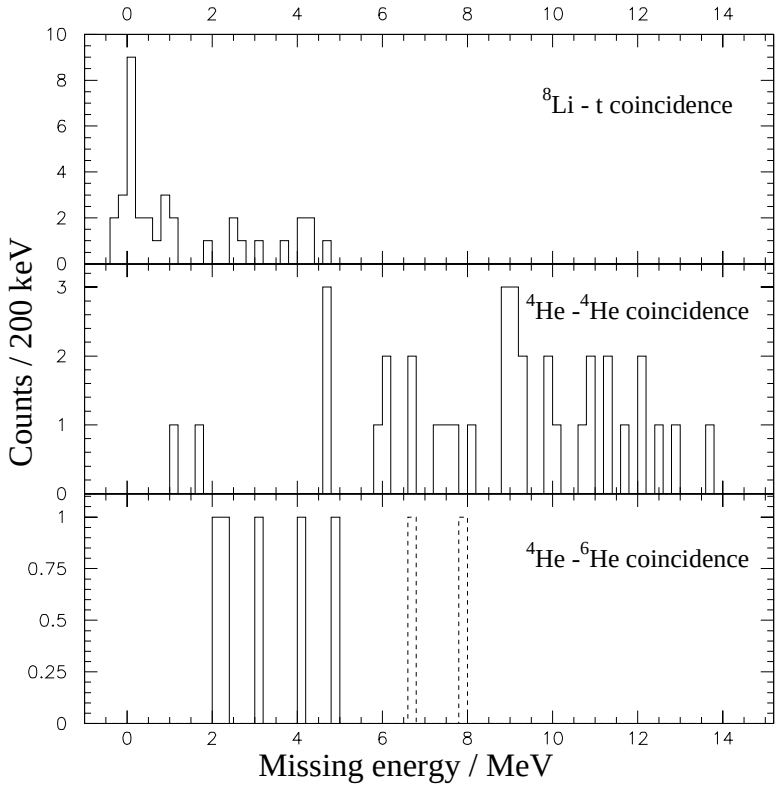

FIGURE 5.24: Plots of missing energy when reconstucting coincidences between DSSSD and the small telsecope (ST), ie E_{Beam} + Q_{Val} - (E_{DSSSD}+E_{ST}). Top: ^{8}Li in DSSSD and tritons in ST. Middle: ^{4}He in both DSSSD and ST. Bottom: ^{4}He in DSSSD and ^{6}He in ST (solid line) and vice versa (dashed line).

working correctly. The middle part of figure 5.24 shows the energy of the three neutrons which are left undetected when two alpha particles are detected, it gives a broad energy distribution. The bottom part of figure 5.24 shows the energy of the single missing neutron. The difference between the solid and dashed line probably arises from the differences in kinematical acceptance and the fact that ^{6}He needs higher energy (about 1-2 MeV cf figure 5.6) to be identified in the DSSSD telescope. Since the kinematic acceptance of the coincidences is rather small, a detailed interpretation of the events is not possible.

Before concluding I would like to touch on the absence of events originating from ^{18}O in some of the reaction channels. In the proton and deuteron channel ^{18}O events are present (especially deuterons from the elastic channel), whereas

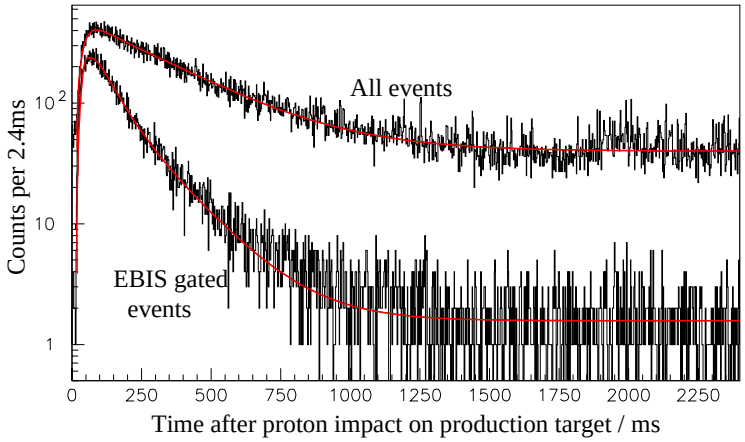

FIGURE 5.25: Time distribution of events from the ^{9}Li+^{9}Be reaction which shows that most events arise from the ^{9}Li content in the beam.

there are no triton events originating from ^{18}O. This is due to the unfavorable Q-value of -1.79 MeV for the ^{18}O+^{2}H$\rightarrow^{17}$O+t reaction. Also in the helium channels ^{18}O events are almost absent, which might be due to the reduced penetrability of charge-two particles vs charge-one particles through the nuclear Coulomb barrier.

5.3.6 Concluding remarks: ^{9}Li on ^{2}H target

We have observed both proton, deuteron, triton, ^{4}He and ^{6}He events emerging when 2.36 MeV/u ^{9}Li impinges on a deuteron target, and thus seen that the many open channels are fed.

It has been proven with the triton case that nuclear structure information can indeed be extracted through transfer reactions at REX-ISOLDE energies. Further it has been demonstrated that differential cross-sections for specific channels can be deduced. With improved angular resolution and an optimized setup to allow for larger CM angular acceptance this can prove very valuable.

The goal of populating states in the particle unbound nucleus ^{10}Li has not been completely fulfilled, although a structure which corresponds very well to recent data from Santi *et al* [San03], has been observed. A future follow-up on the experiment at higher energy (3.1 MeV/u) will most likely take place in 2005 where an improved beam intensity and detector setup hopefully will be available.

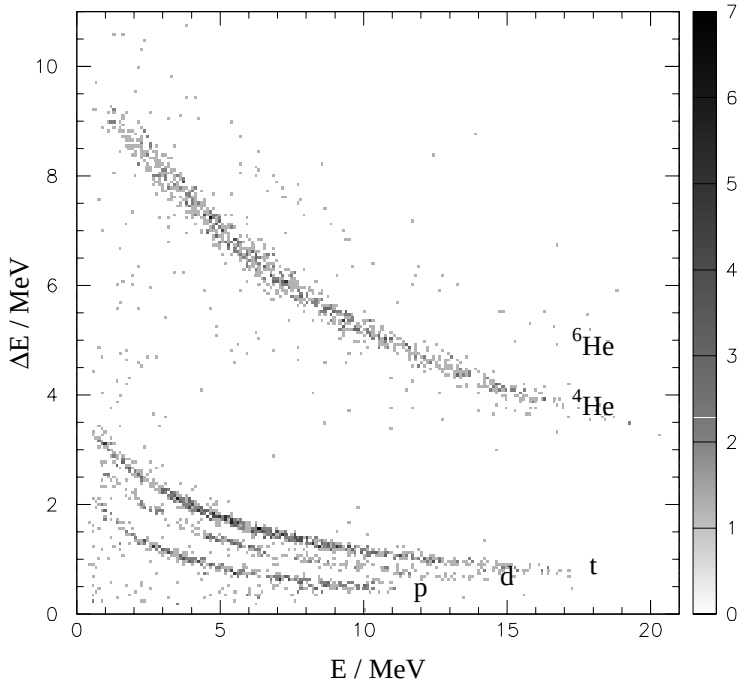

FIGURE 5.26: ΔE-Eplot for the products from the ^{9}Li+^{9}Be reaction. Again both protons, deuterons, tritons, ^{4}He and ^{6}He are identified.

5.4 ^{9}Li on ^{9}Be target

This part of the experiment was designed to study the transfer of a $p_{3/2}$ neutron from ^{9}Be to ^{9}Li. The proposed signature of this reaction should be two ^{4}He nuclei arising from the breakup of ^{8}Be. Unfortunatly the two ^{4}He particle signature proved more difficult to detect than anticipated, though a preliminary analysis of the data shows that it is possible to probe the ^{9}Li+n system from the ^{9}Li+^{9}Be $\rightarrow$ ^{9}Li+n+^{4}He+^{4}He reaction, via either the 0^{+} ground state or 2^{+} first excited state of ^{8}Be. In the following the preliminary analysis of the experiment will be presented.

5.4.1 General characteristics of the ^{9}Li+^{9}Be data

In the ^{9}Li+^{9}Be case the EBIS pulse looks very much as in the ^{9}Li+^{1}H case, hence the same EBIS gate has been applied (0.125-0.160 ms).

The EBIS gated time distribution of all events is shown in figure 5.25 and

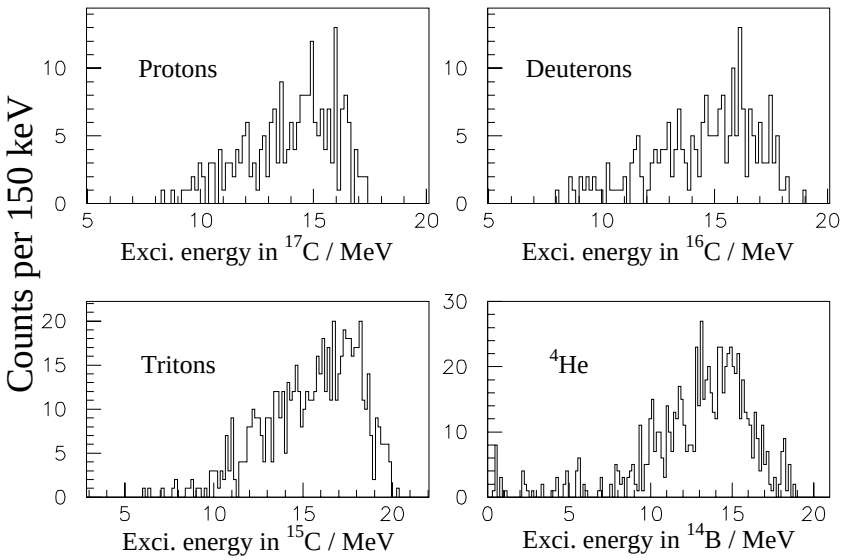

FIGURE 5.27: Extracted excitation energies from the protons, deuterons, tritons and ^{4}He events assuming they arise from the ^{9}Li+^{9}Be reaction.

shows, as the time distribution from the deuteron target, that most events arise from the ^{9}Li beam combined with a flat background from ^{18}O reactions. Again a fit of the release from the target (EBIS gated events) and release folded with the decay of ^{9}Li has been conducted. In this case a half-life of 184$\pm$10 ms has been extracted, again in good agreement with the known half-life. In the following *all events* will refer to all events inside the EBIS gate unless otherwise stated.

In figure 5.26 a ΔE-E plot of all particles penetrating the DSSSD is shown. As in the case of the deuteron target both protons, deuterons, tritons, ^{4}He and ^{6}He are identified. From the ΔE-E plot in figure 5.26 the different types of particles are easily separated and time distributions for these channels have been extracted. All extracted time distributions show a clear beam related structure as in the deuteron target case.

Assuming that the protons, deuterons, tritons and alpha particles, identified in figure 5.26, originate from the

$$^{9}\mathrm{Li} + {}^{9}\mathrm{Be} \rightarrow {}^{17}\mathrm{C} + \mathrm{p}$$
$$^{9}\mathrm{Li} + {}^{9}\mathrm{Be} \rightarrow {}^{16}\mathrm{C} + \mathrm{d}$$
$$^{9}\mathrm{Li} + {}^{9}\mathrm{Be} \rightarrow {}^{15}\mathrm{C} + \mathrm{t}$$
$$^{9}\mathrm{Li} + {}^{9}\mathrm{Be} \rightarrow {}^{14}\mathrm{B} + {}^{4}\mathrm{He}$$

channels (^{6}He has been ignored due to very low statistics), respectively, exci-

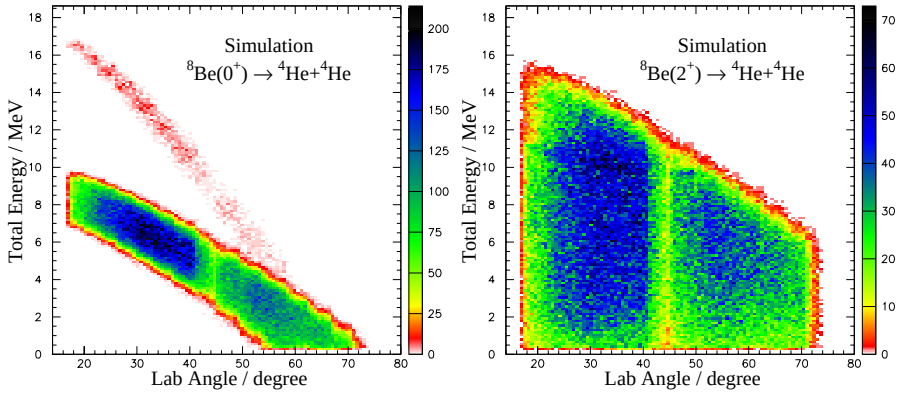

FIGURE 5.28: Total energy vs laboratory angle for ^{4}He particles emitted in the break-up of ^{8}Be via the 0^{+} (left) and 2^{+} (right).

tation energies can be extracted. The excitation energies are shown in the four panels in figure 5.27 which all show a structureless bump looking like the compound nucleus distributions described in section 2.2.2. The only excitation energy which looks a little bit different is the one for ^{14}B (^{4}He detected), which should also be fed via the break-up of ^{8}Be into a 3-body final state. The conclusion is therefore that the single-hit spectra do not hold much spectroscopic information in the ^{9}Be case. To obtain spectroscopic information coincidence data are needed.

5.4.2 Coincidences from ^{9}Be target

If coincidences between two ^{4}He particles are seen they would most probably originate from the break-up of ^{8}Be after neutron pick-up. The total energy vs laboratory angle plots in figure 5.28 show simulations of ^{4}He events from the break-up of ^{8}Be proceeding via the 0^{+} ground state (left panel) and the first excited 2^{+} state (right panel). In the left panel of figure 5.28 it is seen that no events which proceede via the 0^{+} ground state in ^{8}Be have high enough energy to penetrate the DSSSD[6] (the few events in the *red banana* are summing from two ^{4}He hitting the same pixel). The events from ^{8}Be(2^{+}) are shown in the right panel of figure 5.28, and shows that only a small fraction of these ^{4}He events will penetrate the DSSSD.

Since the ^{4}He events from ^{8}Be in most cases are stopped in the DSSSD the obvious first step is to look for coincidences between ^{4}He in the *small telescope*

[6]Only ^{4}He above 10.5 MeV will penetrate, cf section 5.2.

and all events in the DSSSD. In the left panel of figure 5.29 the ΔE-E plot for the *small telescope* is shown. The grey shaded area indicates the selection of ^{4}He events in the *small telescope*. The right panel in figure 5.29 shows the total energy vs laboratory angle plot of all events in the DSSSD which are in coincidence with ^{4}He in the *small telescope*.

Assuming that all coincidences are ^{4}He+^{4}He events it is possible to extract the invariant mass spectrum, that is the excitation energy in ^{8}Be. The invariant mass can be calculated by the formula:

$$\text{Inv. Mass} = \frac{1}{4}\frac{(\vec{P_{\alpha 1}} - \vec{P_{\alpha 2}})^2}{M_{^4\text{He}}}, \tag{5.3}$$

where $\vec{P_{\alpha i}}$ are the momentum of the ith ^{4}He particle and $M_{^4\text{He}}$ is the mass of ^{4}He. Since the invariant mass only includes the difference of the two ^{4}He momenta it does not matter in what frame the momenta are calculated, thus the laboratory frame is chosen since further uncertainties will be added by transformations. From the position in the DSSSD (front strip vs back strip, $\sim 3^{\circ}$ angular acceptance) and *small telescope* (no granularity, $\sim 15^{\circ}$ angular acceptance), and the energy deposited in the respective detectors the momenta of the two ^{4}He in coincidence can be calculated. Using equation (5.3) the invariant mass spectrum of the ^{4}He-^{4}He coincidences can be extracted.

The invariant mass sepctrum in figure 5.30 clearly shows that the ^{4}He-^{4}He coincidences between the *small telescope* and the DSSSD proceed via the first excited 2^{+} state at 3.04 MeV in ^{8}Be (R-matrix calculation with width of $\sim$

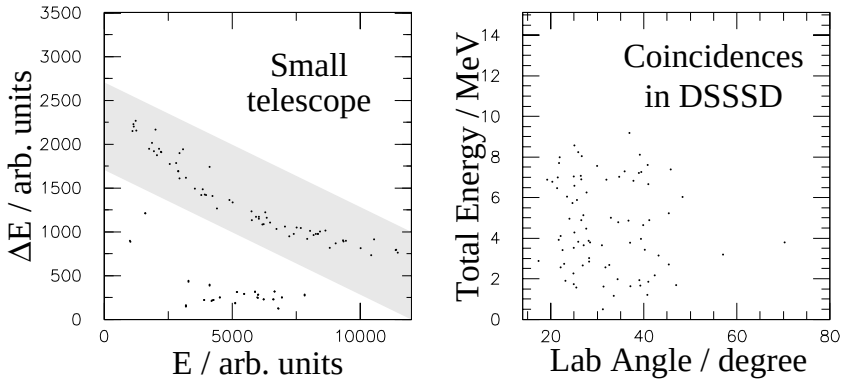

FIGURE 5.29: Left: ΔE-E plot for the *small telescope* where the selected ^{4}He are shaded in grey. Right: Total energy vs laboratory angle plot for all events in DSSSD in coincidences with ^{4}He in the *small telescope*.

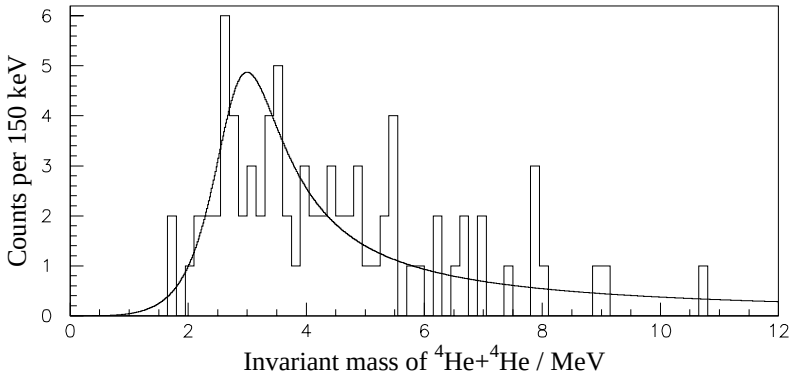

FIGURE 5.30: Invariant mass spectrum of coincidences between *small telescope* and DSSSD. The line shows a calculation of the 2^+ state in ^{8}Be.

1.5 MeV shown as line).

Apart from the coincidences between the *small telescope* and the DSSSD double hits in the DSSSD can also occur. In this case, assuming both hits in the DSSSD are ^{4}He, the invariant mass spectrum can be extracted, and is shown as the solid histogram in figure 5.31. In the figure a peak at zero energy (the peak is asymmetric since invariant mass by definition is positive), whereas events around 3 MeV are almost absent. The dashed histogram in figure 5.31 is an estimate of the background from random coincidences based on the method of *event mixing*. Performing *event mixing* means that all pairs of coincidences are broken, and pairred again in an uncorrelated way[7]. The data and event mixing in figure 5.31 shows very clearly that in the case of DSSSD coincidences the break-up of ^{8}Be proceeds via the 0^+ ground state at 91 keV.

Assuming that all events in figure 5.30 and the events below 200 keV in figure 5.31 arise from break-up of ^{8}Be via the 2^+ (first excited state) and 0^+ (ground state), respectivly, the excitation energy in ^{10}Li can be extracted. This is shown in the upper and lower panel of figure 5.32, respectivly. Unfortunately the only common feature in the two panels of figure 5.32 is the very low statistics. The events in the upper panel of figure 5.32 does not show any specific structure which should probably be ascribed to the very poor angular resolution of the *small telescope*. Whereas the events in the lower panel seem to be concentrated at positive energies. Especially the 8 events in a peak close to zero excitation energy look interesting, or as a lucky statistical coincidence! In both cases the

[7] In our case this was done by storing the highest energy hit, and subsequently using this as the highest energy hit in the next coincidence pair.

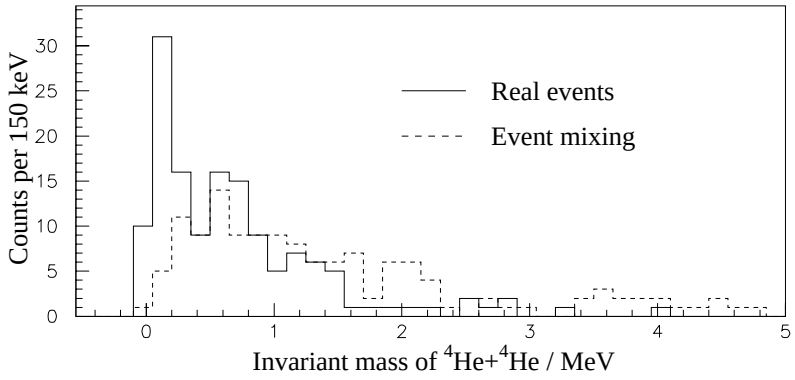

FIGURE 5.31: Invariant mass spectrum obtained from coincidences between two DSSSD (solid). The dashed line are from event mixing and shows that the peak at zero are from real coincidences.

data should improve significantly if two DSSSD telescopes were to be employed at opposite sides of the beam direction placed further away from the target to enhance the angular resolution.

If all events above zero excitation energy are assumed to come from real ^{10}Li events it is interesting to note that the peak around zero excitation excitation energy in ^{10}Li only appears in the events from the 0^{+} ground state of ^{8}Be. It will be very interesting to see if (much) better data could be acquired in the upcomming experiment.

It is interesting to note that the 2^{+} coincidences are seen between the DSSSD and *small telescope* whereas the 0^{+} coincidences are only seen in DSSSD double hits. This is due to the difference in energy in the break-up of ^{8}Be, 3.04 MeV in the 2^{+} case and 0.091 MeV in the 0^{+} case. In fact the distance between the two ^{4}He particles from the 0^{+} break-up is seen to be separated by approximately the size of only one pixel (one pixel is 3.1 mm across). This means that about half of the coincidences are lost since the two particles in a coincidence have to hit both a different front and a different back strip, whereas if the two particles, in a coincidence event, hit different front strips but the same back strip (and vice versa) the event will not be observed. See figure 5.33 for visualisation. Thus an enhanced granularity of the DSSSDs or a larger distance to the detector would improve on this problem. Especially if higher ^{9}Li beam energy will be employed this point must be kept in mind since higher beam energy will focus the particles from the break-up of ^{8}Be even more.

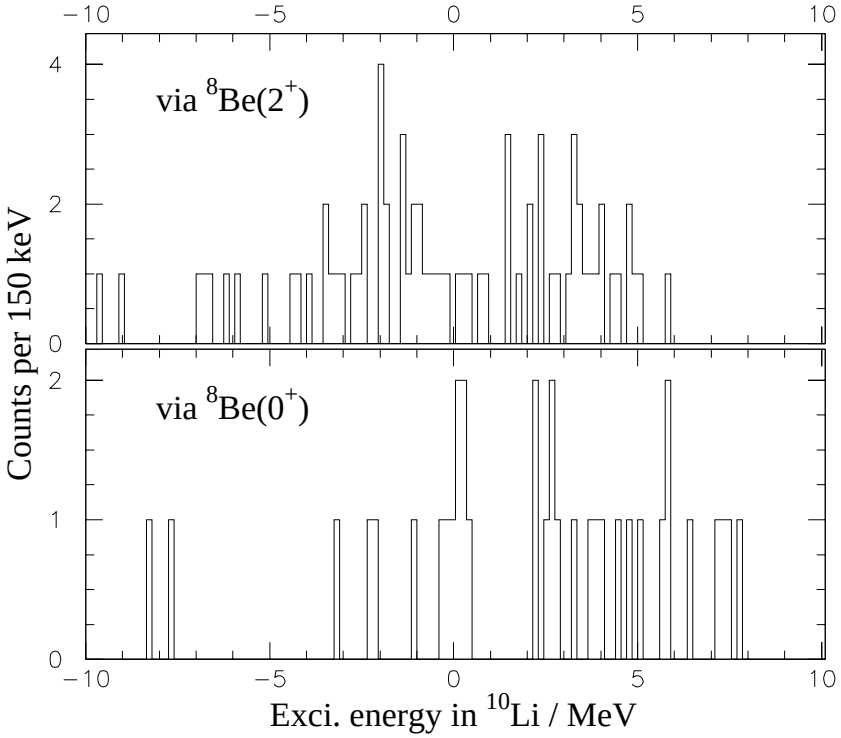

FIGURE 5.32: Excitation energy in ^{10}Li from the ^{9}Li+^{9}Be reaction. Extracted assuming break-up of the 2^{+} first excited state (upper panel) and 0^{+} ground state in ^{8}Be.

5.4.3 Concluding remarks: ^{9}Li on ^{9}Be target

Though more difficult than the transfer reaction on a deuteron target it has been shown that deuteron pick-up from ^{9}Be, leaving ^{8}Be which subsequently break-up into two ^{4}He, is feasible. It has even been shown that ^{8}Be is fed in both the 0^{+} ground state and 2^{+} first excited state, and that events proceeding via these two states can be separated.

The break-up of ^{8}Be has been seen to proceed via both the 0^{+} and 2^{+} state in approximately same quantities even though the acceptance of the two channels are very different, due to the small active area of the *small telescope*. Therefore a setup with a DSSSD on either side of the beam direction would greatly improve the acceptance for the 2^{+} channel, and possibly give very good data. Though it should be noted that the analyzed beam time on ^{9}Be target was the full 27 hours, that is 10 hours more than on the CD target, which does indicate that a much

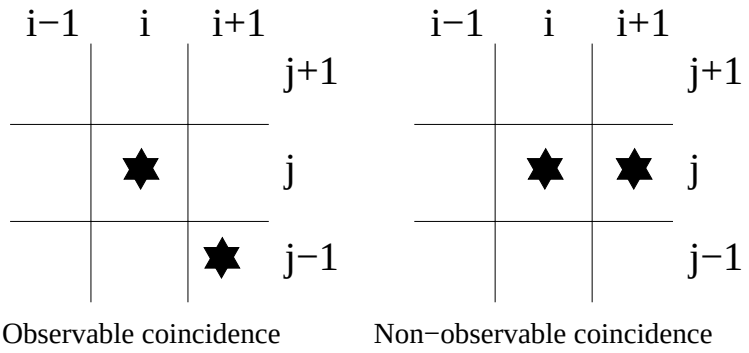

FIGURE 5.33: Sketch showing the difference between observable (left) and non-observable (right) coincidence event in the DSSSD.

better acceptance must be achieved if reasonable results are to be obtained.

Even though the prospects of the ^{9}Li+^{9}Be reaction might not seem too bright, I still think that it should be pursued, at least to investigate if valuable information can be extracted this way.

5.5 Conclusion on transfer reactions

In general it has been shown that most of the channels which can be populated in the ^{9}Li+^{2}H and ^{9}Li+^{9}Be reactions at 2.36 MeV/u are observed.

In the ^{9}Li+^{2}H case several interesting features were seen. First of all the deuteron channel showed an enlarged elastic cross-section relative to Rutherford cross-section. The deuteron data was used to normalize the amount of ^{9}Li incident on target. The proton channel indicates a state at $\sim$ 350 keV above the ^{9}Li+n threshold with a width of $\sim$ 300 keV, which is in agreement with previous experiments. Finally the triton channel also proved very interesting, since the excitation energy spectrum of ^{8}Li could be extracted from 0-4 MeV. This excitation energy range is of great interest since theory has predicted two unobserved states to be present in the range 0-5 MeV. The upcoming continuation of the beam time on this experiment will be very interesting, since better statistics and higher beam energy should enable us to solve several of the remaining questions.

In the ^{9}Li on ^{9}Be target it has been shown that the method of detecting the two ^{4}He particles, ejected from the break-up of ^{8}Be, is feasible. Further it has been shown that the break-up can proceed both via the 0^{+} ground state and 2^{+} first excited state, and that they can be separated.

These two experiments have proved that it is quite difficult to perform re-

actions with radioactive beams due to the very low yield of the wanted beam (less than 1×10^{5}/s was achieved). This effect was enhanced by the unfortunate reality that it has proved more difficult to deliver the radioactive beams with REX-ISOLDE than expected. Further the issue of contaminant beams also complicates the experiment, since only a very weak contaminant beam of 10^{4}/s would introduce serious problems, whereas a contaminant beam of 10^{6}/s in most cases would rule out the possibility of performing the experiment.

Even though this is our first experiment with transfer reactions on radioactive beams at very low energy I still think that it has shown that we are indeed on the right track with respect to extracting nuclear structure information.

As an improvement of the experiment it would be very useful to have detection of the heavy residue from the reaction, since this would allow for coincidence measurements which potentially is much cleaner, and possibly extension of the angular coverage. This could be achieved by a dedicated spectrometer at REX-ISOLDE, which at the present time is under consideration. Apart from this other considerations should be made before the continuation of the experiment. Some of these are addressed in the Outlook and Improvements chapter at the end of this thesis.

CHAPTER 6

Elastic resonance scattering: ^{9}Li+^{1}H

In this chapter I will introduce the concept and idea of elastic resonance scattering.
The data from our elastic resonance scattering experiment ($^{9}Li+^{1}H\rightarrow^{9}Li+p$) and a test experiment ($^{12}C+^{1}H\rightarrow^{12}C+p$) will be presented together with a tentative analysis.

6.1 Introduction

The first beam time on the elastic scattering of protons on ^{9}Li (IS371) was performed at REX-ISOLDE in October 2003 (see proposal at [IS371]). Unfortunately the REX-EBIS unit was suffering severe problems with a high voltage supply, causing this beam time, and the second run on IS367, to be shortened. Because of these problems less than 2 days of effective data taking on IS371 was completed. In spite of the shortened beam time the test still turned out to be a success, since both reasonable data and valuable experience at REX-ISOLDE was achieved.

The purpose of performing a resonant elastic scattering experiment of protons on ^{9}Li was to look for the **I**sobaric **A**nalogue **S**tates (IAS) of ^{10}Li in ^{10}Be to gain insight on the states in ^{10}Li via an independent probe. The basic idea is that the spectrum of the IAS, correspond to states in ^{10}Li, only shifted by the Coulomb displacement energy, caused by the different Coulomb interaction in the two nuclei. The displacement energy is composed of a general Coulomb shift between two members of the same isobaric multiplet and the Thomas-Ehrmann shift [Tho50, Ehr51] between different levels within one nucleus. A compilation of Coulomb displacement energies for most $3 \leq A \leq 239$ nuclei are given in [Ant97].

When using a thick target in resonant elastic scattering experiments the ions scan the relative energy between the ion and the proton while stopping in the target. This makes the experiment very efficient, since time consuming step-wise scanning of the resonance energy is avoided, but also more difficult to analyse because the reaction position, and thereby resonance energy, has to be extracted from the proton energy and angle. It is feasible to extract the resonance energy unambiguously if the incoming ion (^{9}Li) has a larger energy-loss per length than the elastic scattered particle (proton) and if none of the involved nuclei have an excited state which can be excited by the maximum resonance energy.

In IS371 the ^{9}Li was produced in a 70 g/cm^2 Ta target, as in the IS367 experiment described in the previous chapter. Proton energy, intensity and ion-source parameters were also as described in the previous chapter. Most of the proton pulses, incident on the production target, were separated by 2.4 s and about 45% were only separated by 1.2 s. The ^{9}Li intensity at the detector setup was estimated to be 10^{4}/s . As in the previous experiment a ^{18}O contamination was present.

In addition to ^{9}Li, a 2.21 MeV/u $^{12}C^{+4}$ beam, from rest-gas in the REX-EBIS, was produced to perform a cross-check with ^{12}C+^{1}H resonant elastic scattering reaction, already experimentally investigated in 1951 by Goldhaber

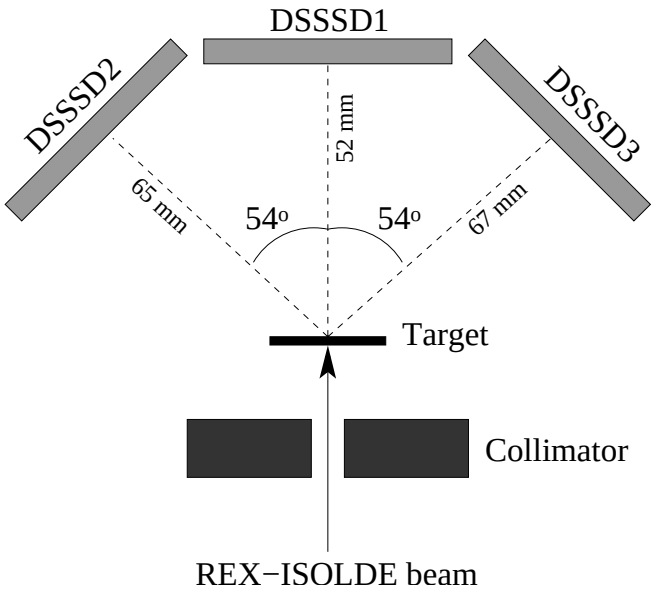

FIGURE 6.1: Sketch of setup used in the IS371 experiment. Note that the labels DSSSD1-3 should be understood as the whole telescope, ie a DSSSD and a Si-pad detector.

and Williamson [Gol51] (for a compilation of experimental effort on this reaction see [Gur98]).

The data presented in this chapter has only been preliminary analysed, thus several open questions and short-comings still need to be addressed. Even though this analysis has not been completed, it still seems appropriate to present it here, since interesting results have been achieved.

6.2 Experimental setup

For the IS371 experiment a setup composed of three DSSSD telescopes was used.

The REX-ISOLDE $^{9}Li^{+2}$ beam (2.25 MeV/u) entered the detector setup through a 4 mm diameter tungsten collimator, and was subsequently stopped in a 105$\pm$5 μm polyethylene target ($(C_4H_2)_n$). The CH target was irradiated with ^{9}Li for 24 hours and with ^{12}C for 12 hours. The detector setup consisted of three DSSSDs all backed by thick Si-pad detectors, forming telescopes. The specifications of the detectors were as follows (all DSSSDs are of 16$\times$16 strips with a total area of 5$\times$5 cm, as described in section 3.5): One DSSSD of 60 μm thick-

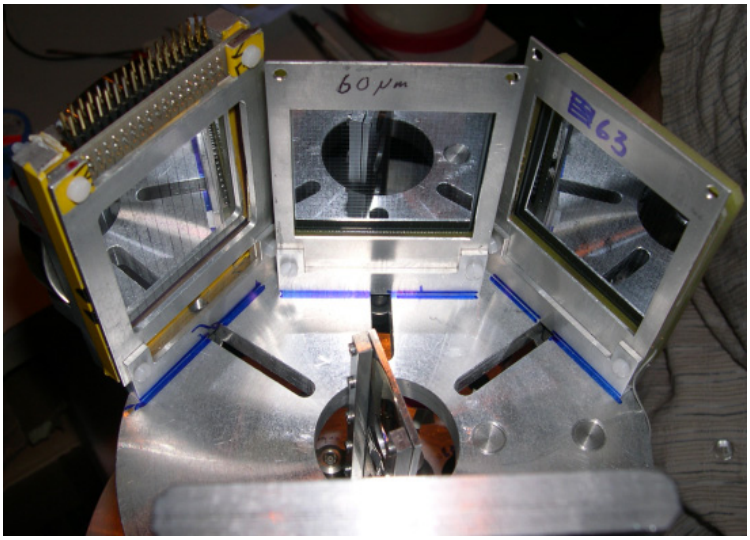

FIGURE 6.2: Photograph of setup used in the IS371 experiment. In the lower part of the photograph the tilted target-ladder is visible. The middel and right DSSSD are of the new type with only 100 nm dead-layer.

ness (new type with thin window) backed by a 1498 μm Si-pad (DSSSD1), one DSSSD of 64 μm thickness (old type with thick window) backed by a 700 μm circular 5 cm diameter Si detector (DSSSD2) and one DSSSD of 63 μm thickness (new type with thin window) backed by a 1473 μm Si-pad (DSSSD3). In figure 6.1 a sketch of the main components in the detector setup and their relative position is shown. In figure 6.2 a photograph of the setup used in the IS371 experiment is shown (the REX-ISOLDE beam enters from the bottom of the photograph). The DSSSDs in the middle and to the right are of the new type with a thinner dead-layer, which can be seen by the slightly darker reflection. All detectors are covered by a mask (the aluminium frame) to avoid noise from edge effects.

The setup with three DSSSD telescopes was applied to look for charged particles scattered into large angles, in contrast to normal resonant elastical scattering experiments where only particles close to zero degree scattering are wanted. It was subsequently observed that very few events where seen in the two off-center DSSSD telescopes (DSSSD2 and DSSSD3 in figure 6.1), and that elastically scattered protons for normalization were almost absent.

In both cases described below an EBIS gate of 100 μs was applied, and in the ^{9}Li case the time distribution of this was very noisy. Interestingly some of

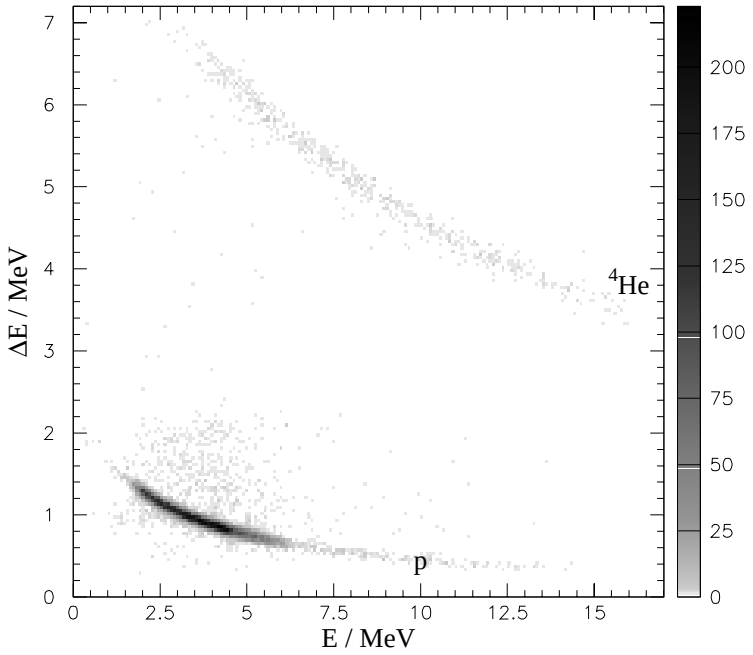

FIGURE 6.3: ΔE-Eplot for all the products from the ^{12}C+^{1}H resonant elastic scattering. Note that only protons and a few ^{4}He are observed in this case of stable beam.

this noise seemed to be correlated with the REX-EBIS/REX-TRAP cycle, and should be investigated further.

6.3 The test case: ^{12}C+^{1}H

This part of the experiment was performed to have reference data so that cross-checks could be made, and to establish that the method of resonant elastic scattering works with solid targets.

The time distribution of the ^{12}C data is of course not very interesting since they are produced continously in the REX-EBIS. Hence the first interesting plot for the ^{12}C data is a ΔE-E plot for all events seen in the DSSSD telescopes, which is shown in figure 6.3. From the ΔE-E plot it is seen that a very large amount of protons and only few ^{4}He are seen (about 16000 protons and 500 ^{4}He nuclei). Due to the preliminary status of the analysis I will in the following only address the protons.

From the protons identified in the three DSSSD telescopes a combined total

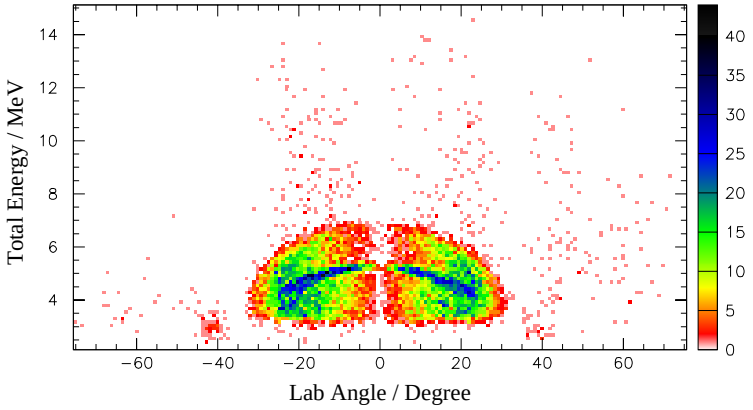

FIGURE 6.4: Total energy vs laboratory angle for proton events from the ^{12}C+^{2}H reaction.

energy vs laboratory scattering angle plot can be extracted, and this is shown in figure 6.4. The left DSSSD covers from -70° to -40 °, the center DSSSD from -30 ° to 30 ° and the right from 40 ° to 70 °. In both figure 6.3 and figure 6.4 it is seen that a large quantity of low energy protons (less than 7 MeV) are present, whereas only a small amount is present at higher energy. Via simulations it can be shown that this small amount of high energy protons mostly arise from compound reactions between the ^{12}C beam and the ^{12}C in the target, since only this reaction can produce such high energy protons. In figure 6.4 the forward peaked structure of the elastic proton scattering is visible, and confirms that only the center DSSSD telescope is important for the analysis. In the same figure the data shows a blue band, which correspond to a resonance in the ^{12}C+^{1}H reaction. The structure seen in figure 6.4 clearly show the kinematic limitations of elastic scattered protons (maximum energy at a given laboratory angle), and that the blue line from the resonance in ^{13}C becomes more defuse at larger angles.

As mentioned in the beginning of this chapter the ^{12}C enters the target with 2.21 MeV/u and scans the resonance energy (E_{CM} between ^{12}C and ^{1}H) as it is stopped in the target. If an elastic scattering between ^{12}C and ^{1}H occurs at a certain depth the proton will be emitted with an energy which depends on the depth. The emitted proton will also suffer energy-loss in the remaining part of the target, but it is possible to calculate the resonance energy afterwards if the energy-loss per length is larger for ^{12}C (incoming nucleus) than for ^{1}H (outgoing nucleus).

It is now possible to extract the resonance energy unambiguously in ^{13}C from the energy and angle of the detected protons, since the first excited state

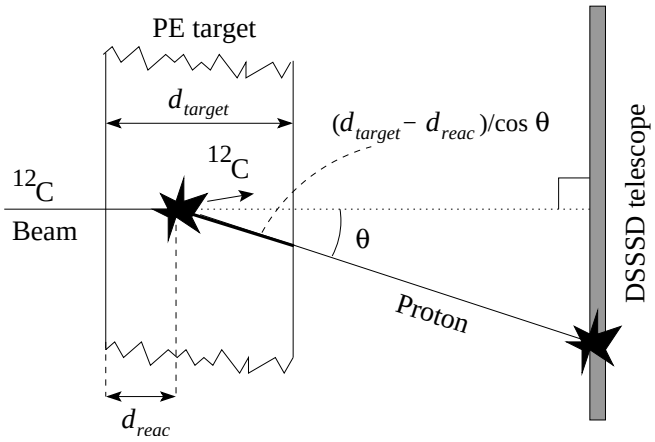

FIGURE 6.5: Sketch of the important parameters for resonant elastic scattering in thick targets. See text for method to extract resonance energy.

in ^{12}C is at 4.44 MeV and thus higher than the maximum resonance energy (E_{CM}=2.04 MeV, at 2.21 MeV/u ^{12}C). From the position of the proton hit in the DSSSD the proton scattering angle, θ, can be found. This is possible assuming that the REX-ISOLDE beam is well collimated, which is a good approximation since the beam passes a collimator with 4 mm diameter a few cm before the reaction target, and the DSSSD has a resolution of approximately 3 mm.

The extraction of the resonance energy proceeds via two steps: Firstly the energy of the proton leaving the target has to be found from the energy detected in the DSSSD, the thickness of the dead-layer of the DSSSD and the entry angle of the proton (θ). This exit energy can be found from an energy-loss calculation based on ion ranges from SRIM 2003 [SRIM]. Secondly the resonance energy (E_{CM} at the depth where the reaction occurs) can now be calculated by adjusting the reaction depth (d_{reac}) until the energy-loss of ^{12}C passing through d_{reac}, and the energy loss of the proton passing through (d_{target}-d_{reac})/cos(θ) gives the correct exit energy for the proton. This calculation can of course not be performed analytically but has to be done via an iterative process of continuously recalculating the energy losses. In figure 6.5 is shown a sketch of how the reaction occurs in the target, and some relevant physical parameters. The figure is not to scale.

When adding the threshold energy of ^{12}C+p in ^{13}N (1.9435 MeV) to the resonance energy, extracted in the way described above, the excitation energy in ^{13}N shown in figure 6.6 is found. In figure 6.6 the excitation energy has been fitted with a simulation of the Rutherford component (flat distribution, adjusted

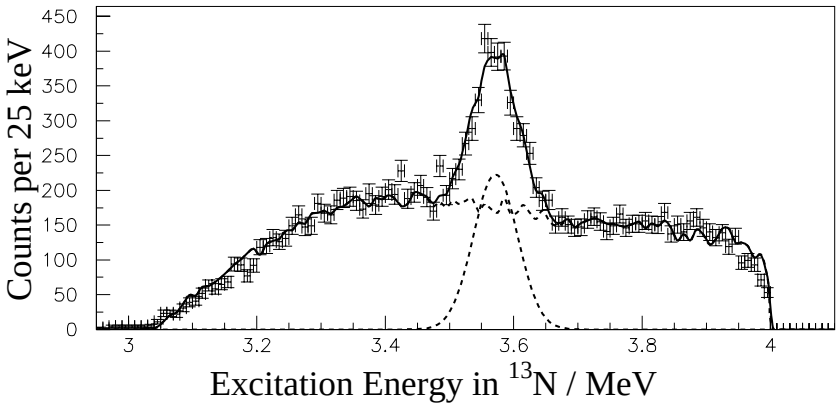

FIGURE 6.6: Excitation energy in ^{13}N from elastic scattering of protons on ^{12}C. The solid line shows a fit to the non-resonant Rutherford background and one gaussian. The dashed line shows the two components.

only the weight) and one gaussian peak, which are seen to describe the data very well. The center value of the gaussian is 3.566±0.002 MeV (σ=0.34 MeV) which is only 19 keV from the tabulated value 3.547±0.004 MeV for the third excited state in ^{13}N [Ajz91]. Another state exist in ^{13}N at 3.502±0.002 MeV, but it has neither been seen in this experiment nor in other elastic proton scattering experiments (best observed in [Sal93] where the excitation energy was scanned from 3.5-3.75 MeV). Furthermore a state close to the ^{12}C+p threshold, at 2.3649±0.0006 MeV excitation energy, should also have been seen but the trigger threshold in the Si-pad detector behind the DSSSD was very high (about 1.8 MeV) because of noise, thus cutting the low energy protons. It should be mentioned that the simulation of the Rutherford background in figure 6.6 exceeded the data points until the high threshold in the the Si-pad detectors was introduced.

The reasons for not observing the resonance at 3.547±0.004 MeV, but at 3.566±0.002 MeV (19 keV off), can be many. First of all it could be that the thickness of the target is different from 105 μm, which has been used to calculate the resonance energy. The uncertainty in target thickness is ±5 μm, which would give a shift in the resonance energy of about ±10 keV. Secondly it could arise from uncertainty in the calibration, where a 1% error would shift the resonance energy by approximatly 15 keV. Finally there is also the pulse height defect[1],

[1]The pulse hight defect describes the difference in accumulated charge in a Si detector from different nuclei with the exact same energy.

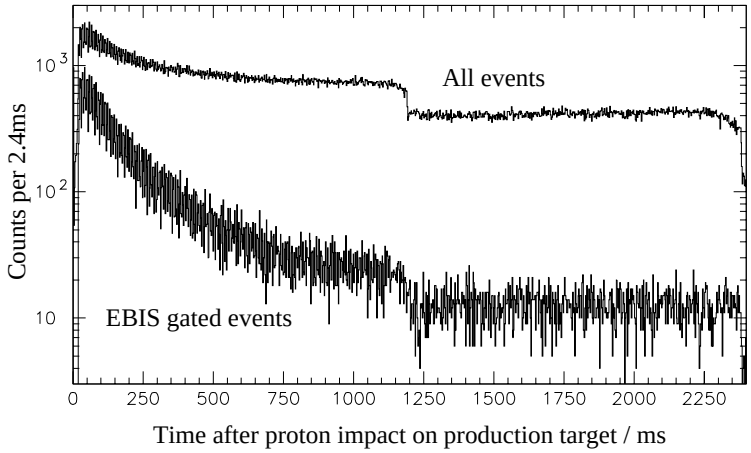

FIGURE 6.7: Time distribution for all and EBIS gated event from the ^{9}Li+^{1}H reaction.

which would give a $\sim$ 1% smaller signal from charge-one particles compared to ^{4}He particles [Mit76], which were used for calibration. Unfortunately this effect moves the resonance toward higher energy (+10-15 keV when adding 1% to all proton energies). Considering all these possibilities for this relatively small energy shift, I will not attempt to point out one of these effects nor will I correct for this shift.

6.3.1 Concluding remarks: ^{12}C+^{1}H

In conclusion of this ^{12}C+^{1}H test experiment it should be noted that the method seems to work very well with a resolution of about 35 keV (σ). In fact it could possibly lead to better precision on the third excited state in ^{13}N if an improved experiment would be performed. It has also shown that our simulations of Rutherford background are very precise and describes the data in the full range. Furthermore it will be interesting to re-measure the ^{12}C+^{1}H reaction to see if the low energy resonance is visible.

6.4 The experiment: ^{9}Li+^{1}H

From the 24 hours of ^{9}Li beam on the PE target only 16.5 hours were accepted for the preliminary data analysis, due to noise during some of the data files.

The time distribution of all and EBIS gated events from the ^{9}Li+^{1}H elastic scattering is shown in figure 6.7. The EBIS gated events look very resonable,

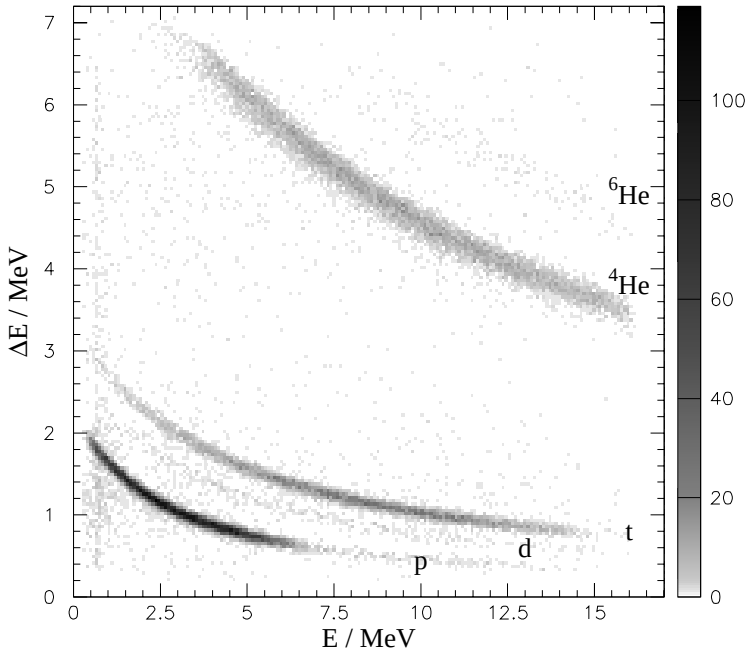

FIGURE 6.8: ΔE-Eplot for the products from the ^{9}Li+^{1}H resonant elastic scattering. Again both protons, deuterons, tritons, ^{4}He and ^{6}He are identified.

with a clear radioactive beam component, whereas the total time distribution shows an overwhelming backgroud. Due to this large background it has not been possible to extract half-life of the radioactive beam component as in the two transfer reaction experiments in the previous chapter. The background is presently not fully understood, but might be due to noise in the electronics which was a large problem during the entire beam time, and decay of ^{9}Li.

In figure 6.8 the ΔE-E plot for the EBIS gated events from the ^{9}Li+^{1}H is shown. Again, as for the transfer reactions, many different reaction products are observed, although the deuteron branch is very weak. This is in contrast with the ^{12}C+^{1}H case where only protons and ^{4}He were observed. The time distributions of the protons, deuterons, tritons and ^{4}He fragments identified in figure 6.8 are shown in figure 6.9 (^{6}He has been omitted due to low statistics). From figure 6.9 it is seen that only the proton channel has a flat background originating from ^{18}O, whereas the deuteron, triton and ^{4}He channels are very clean. This is very resonable, since elastically scattered protons from ^{18}O should be present. The absence of events from ^{18}O in the other channels is in agreement with smaller

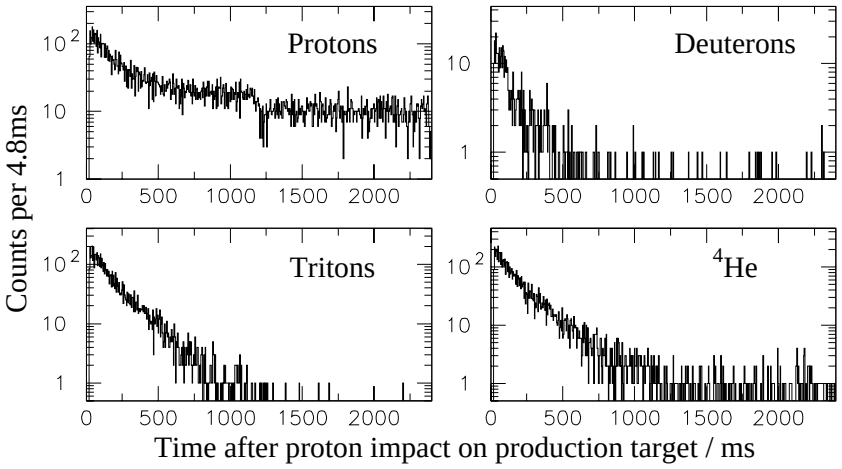

FIGURE 6.9: Time distribution for the products from the ^{9}Li+^{1}H resonant elastic scattering. Only for the proton branch a substantial background is present.

nuclear cross-section, due to larger nuclear charge, and Q-values (the deuteron and triton channels are closed for ^{18}O+^{1}H). From the proton time distribution it can be seen that almost half of the protons in the first 600 ms seem to originate from ^{18}O, which of course also has a larger Rutherford cross-section, due to its larger Z.

From simulations it can be shown, from the energy range, that the deuterons cannot originate from the ^{9}Li+^{1}H reaction (Q_{val}=-1.84 MeV), but instead from the ^{9}Li+^{12}C reaction (Q_{val}=8.48 MeV), whereas all of the protons, tritons and ^{4}He events fall within the their respective energy ranges. However a small part of the protons, above $\sim$ 6 MeV in figure 6.8, most likely comes from the ^{9}Li+^{12}C channel (Q_{val}=13.87 MeV).

Concentrating on the protons, which carry the information on the IAS in ^{10}Be, the first step is to look at the total energy vs laboratory angle plot for the protons identified in figure 6.8. This is shown in figure 6.10 where no clear structure is observed, although the same general structure as in the corresponding plot for the ^{12}C+^{1}H case is seen (figure 6.4). The overall structure in the total energy vs laboratory angle plot simply shows the general bonds arising from kinematical relations. The lack of clear structures in figure 6.10 indicates that no narrow and intense resonance is present, as were the case for ^{12}C. From the identified protons it is, as in the ^{12}C case, possible to extract the resonance energy of the elastic scattering unambiguously, since ^{9}Li has no excited state below the maximum resonance energy (E_{max}=2.025 MeV, first excited state at 2.69 MeV).

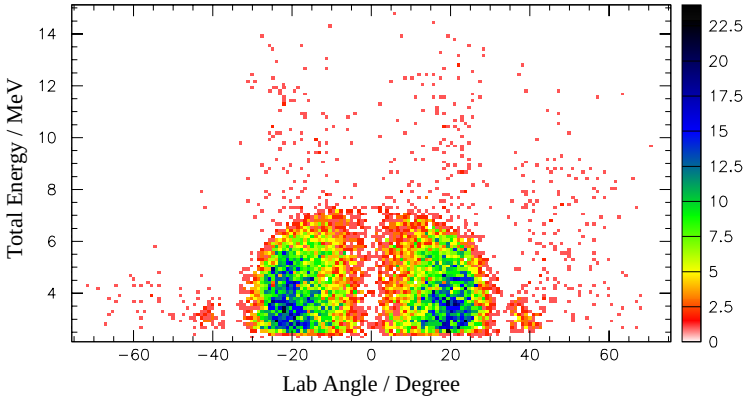

FIGURE 6.10: Total energy vs laboratory angle for protons from ^{9}Li+^{1}H elastic scattering.

The calculation performed to extract the resonance energy was similar to the one performed in the ^{12}C case. Adding the threshold of ^{9}Li+p in ^{10}Be to the resonance energy the excitation energy in ^{10}Be can be found. When subtracting the estimated ^{18}O background contribution, found from the excitation energy at *late time* (1200-2400 ms), the excitation energy spectrum originating from ^{9}Li+^{1}H, shown in figure 6.11, can be found. The excitation energy spectrum in figure 6.11 has been fitted with a simulation of the Rutherford component (only weight fitted) and three gausian peaks. The resulting total fit and components are shown on the figure in solid and dashed lines, respectivly. The value of the fitted parameters for the gaussian peaks are listed in table 6.1. The 20 keV shift seen in

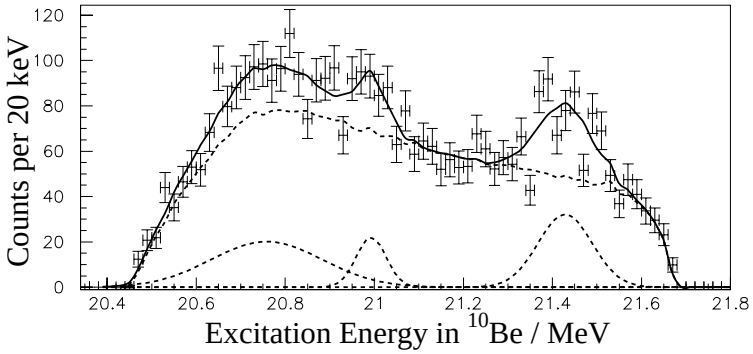

FIGURE 6.11: Excitation energy in ^{10}Be, extracted from ^{9}Li+^{1}H elastic scattering.

	Center / MeV	Sigma / MeV
Peak 1	20.75±0.06	0.12±0.09
Peak 2	20.98±0.01	0.03±0.01
Peak 3	21.418±0.009	0.06±0.01

TABLE 6.1: Parameters for gaussian fitted to ^{10}Be excitation energy.

the ^{12}C case for the center value should also be added to the fitted center values as a systematic error, but this has been omitted in this preliminary analysis. It should be noted that the widths of the fitted gaussians are less reliable than the center values. A fit without and with two gasussians has also been performed (reduced log likelihood χ^2=2.7 and 1.96, respectively) but none of these gave a better result than the three gaussian fit (reduced log likelihood χ^2=1.6).

In a preliminary version of the compilation of energy levels in A=10 nuclei by D.R. Tilley *et al* [Til03] two levels in ^{10}Be are reported within the energy range covered in this experiment (20.5-21.7 MeV). The two levels are located at 20.8±0.1 MeV and 21.216±0.023 MeV, the latter suggested to be the IAS of the ground state of ^{10}Li. The first thing to note is that a state at 21.22 Mev is not seen in this experiment, which indicates that it is not the IAS of the ground state of ^{10}Li. Unfortunately the two papers reporting this state are very difficult to acces, so it has not been possible to investigate this further (the reaction and references are: ^{9}Be(n,γt)^{7}Li (E_n=12-200 MeV) [Nel02] and ^{7}Li(t,p)^{9}Li which further suggests a width of 0.08 MeV [Guz90]). An older paper [Abr79] also reports the 21.2 MeV, but has no firm conclusion about the isospin of the state. Concerning the level at 20.8 MeV it seems to coincide with the peak observed at 20.75±0.06 MeV. Again no extra information exists since values in [Til03] have been given via private communication, although it is mentioned that the state was observed through the ^{7}Li+^{7}Li reaction at 34 and 51 MeV. Assuming that the 20.8 MeV state is not an IAS of ^{10}Li, we are left with two possible states, which might be IAS of the ground state and an excited state in ^{10}Li.

To get closer to the origin of these levels seen in ^{10}Be, and maybe answer the question whether any of them are analogues to states in ^{10}Li, it would be appropriate to get an idea about where these possible IAS are situated in ^{10}Li. That is, the Coulomb displacement energy has to be found. The first step would be to simply calculate the difference in Coulomb energy if both ^{10}Be and ^{10}Li have a uniform spherical charge distribution. In this case the Coulomb energy

difference is given by:

$$\Delta E_C = \frac{3}{5}\frac{e^2}{4\pi\epsilon_0 R}(2Z-1) = 2.63 \text{ MeV}, \quad (6.1)$$

where Z is the largest of the two charges (ie 4) and the radius R is given by 2.3 fm. Next, the excitation of possible levels in ^{10}Li is found very easily from the formula:

$$E_{ex}(^{10}\text{Li}) = M(^{10}\text{Be}) - M(^{10}\text{Li}) + \Delta_{nH} - \Delta E_C + E_{ex}(^{10}\text{Be}), \quad (6.2)$$

where M and E_{ex} represents the mass and excitation of the respective nuclei and Δ_{nH} is the mass difference between neutron and the hydrogen atom. The masses and mass differences are listed below [Aud03]:

$M(^{10}\text{Be})$	12.6067(4) MeV
$M(^{10}\text{Li})$	33.051(15) MeV
Δ_{nH}	0.782354(3) MeV

Combining equation (6.2) and the values tabulated above the levels seen in ^{10}Be should correspond to levels at -1.32 MeV (20.98 MeV peak) and -0.87 MeV (21.418 MeV peak) in ^{10}Li. This result is not very promising, since negative energy states cannot exist, but it should also be kept in mind that this approach is very primitive. Another possibility would be to extrapolate fitted parameterizations of the Coulomb displacement energy for T=2 nuclei, as found in the compilation by Antony *et al* [Ant97].

$$\Delta E_C = 1.4067(6)\bar{Z}/A^{1/3} - 0.8728(32) = 1.412(3) \text{ MeV}, \quad (6.3)$$

were $\bar{Z}$ is the average charge of the two nuclei (ie 3.5) and A is the mass number. Equation (6.3) returns a smaller number than the uniform spherical charge distribution did, which makes sense because the added proton is not uniformly distributed but more concentrated at the surface of ^{10}Be since the extra proton is in a p-wave. Furthermore when scanning the Coulomb displacement energies in [Ant97] for lighter Li-Be pairs[2] values from 1.35-1.7 MeV are found, in nice agreement with the result from equation (6.3). Thus, it seems resonable to assume that the Coulomb displacement energy for ^{10}Li-^{10}Be is close to 1.4$\pm$0.1 MeV. It should be noted that the Coulomb displacement energy is not a fixed parameter for a corresponding pair of nuclei, but that it should be calculated for each pair of **corresponding levels** between the two nuclei. The shift in displacement energy between different levels within one corresponding pair, is for the Li-Be pairs, on the order of $\pm$0.1 MeV.

[2] From the parametrization of the Coulomb displacement energies found in [Ant97], which are very alike for T=1,3/2 and 2, it seems resonable to compare different Li-Be pairs.

	$E_{ex}(^{10}Be)$ / MeV	$E_{ex}(^{10}Li)$ MeV
Peak 2	20.98±0.01	-0.08±0.1
Peak 3	21.418±0.009	0.36±0.1

TABLE 6.2: Correspondence between IAS in ^{10}Be and ^{10}Li. Excitation energy in ^{10}Li calculated from equation (6.2) and (6.3).

Applying the Coulomb displacement energy calculated from [Ant97] on the two levels observed in ^{10}Be the resulting levels in ^{10}Li are shown in table 6.2. The calculated excitation energies are in good agreement with proposed states in ^{10}Li. Thus the preliminary interpretation of the elastic scattering data is that we see the IAS of the ground state and first excited state at $\sim$ 0.3 MeV in ^{10}Li.

6.4.1 Concluding remarks: ^{9}Li+^{1}H

Impressive data has been collected considering the problems during beam time. The preliminary analysis of the ^{9}Li+^{1}H elastic scattering indicates three states in ^{10}Be at 20.75 MeV, 20.98 MeV and 21.41 MeV. These states have been suggested to be a previously seen state at 20.8 MeV and two analogue states to the ground state and first excited state. If the parametrization of the Coulomb displacement energy from [Ant97] is applied the two proposed analogue states correspond to states at -0.08±0.1 MeV and 0.36±0.1 MeV in ^{10}Li. This is, although just a guess, in very good agreement with the general trend in experimental observed states in ^{10}Li (see table 4.1).

6.5 Conclusion on resonant elastic scattering

In spite of the limited beam time for the resonant elastic scattering experiment resonable results have been achived.

In general the Rutherford background has been simulated very accurately in both the ^{12}C and ^{9}Li case, which is of great importance for the interpretation of the data.

The data from the ^{12}C elastic scattering clearly shows the known resonance at 3.547 MeV in ^{13}N, whereas the state at 2.365 MeV has not been observed. This was due to a high trigger threshold in the Si-pad detector, which was set because of noise. This test experiment shows that we have a very fine resolution of the excitation energy ($\sigma \simeq$35 keV).

From the ^{9}Li elastic scattering the results are less clear, though still impressive considering the limited beam time. Here in the preliminary analysis three states are seen in ^{10}Be, of which two are suggested to be analogues of states in ^{10}Li. Apart from the proton channel also tritons and ^{4}He particles are observed from the ^{9}Li+^{1}H reaction. Especially the triton channel might also contain interesting information about ^{10}Li.

The continuation of this experiment will be exciting to follow, both because the relative short beam time revealed interesting information, but also because the energy will be enhanced, thus allowing us to look for the analogue state of the second excited state in ^{10}Li situated around 500 keV.

In general this experiment seems to have been running very well and therefore no major changes seems necessary. Though it might make sense to remove the two off-center DSSSD telescopes, since they do not play any role in the analysis.

It should be noted that a better overall resolution can be achieved by limiting the angular acceptance, as shown in the next chapter on Outlook and Improvements. This has however not been applied in this analysis due to the limited statistics in this case.

CHAPTER 7

Outlook and improvements

In this chapter I will try to outline the future perspectives for nuclear reactions at REX-ISOLDE and via simulations indicate which directions improved detector setup and higher beam energy will lead.

7.1 Introduction

In this chapter I will indicate which improvements could, and maybe should, be done before the next beam time at REX-ISOLDE. Firstly, I will investigate what impact the REX-ISOLDE beam energy upgrade, which has been completed (up to 3.1 MeV/u), will have, and if it will improve on all experiments. Secondly, I will discuss how the detector setup could be improved.

7.2 Higher REX-ISOLDE beam energy

With the energy upgrade of REX-ISOLDE, completed in the spring of 2004, the beam energy available is now either 0.8-2.3 MeV/u or 3.1 MeV/u, thus allowing to make reactions with more energy available for excitations in the produced nuclei. Even though this might not always be an advantage, since the possibility of excitations in both nuclei created in a binary reaction will lead to more complications, it will be crucial in the ^{9}Li+^{2}H$\rightarrow^{10}$Li+p experiment. In the following I will, via simulations, investigate the new possibilities offered by higher beam energy.

First of all, calculations by Lenske and Schrider [Len98] show that the integrated cross-section for (d,p) reactions with exotic nuclei should reach its maximum around $E_{lab}\simeq$3-5 MeV/u, thus giving a larger reaction yield at the new REX-ISOLDE beam energy. Furthermore, a higher beam energy focuses the reaction products more in a forward direction (beam direction), which makes the detection easier, although it requires better angular resolution.

In figure 7.1 simulations of total energy vs laboratory or CM scattering angle for different reaction channels and beam energies for the^{9}Li+^{2}H reaction is shown. The laboratory angles are shown in black lines and the CM angles in red lines, whereas the solid lines are for simulations at 2.36 MeV/u and the dashed line are for 3.1 MeV/u. In all plots the minimum energy required for particle identification in the DSSSD-telescopes, for the different channels, are indicated by dotted horizontal lines, where the upper is for our present $\sim$ 65 μm DSSSDs and the lower for possible 40 μm DSSSDs. For comparison is should be noted that the acceptance in laboratory angles for our previous transfer experiment was 18-80 $^{\circ}$.

In the upper panel in figure 7.1 the prospects for the proton channel is shown, and it is seen that especially the energy acceptance will greatly improve with higher beam energy, whereas the CM angular acceptance will only improve about 10°. In the middle panel the same trends are seen for the deuterons, although the CM angular resolution is almost unchanged. The lower panel in

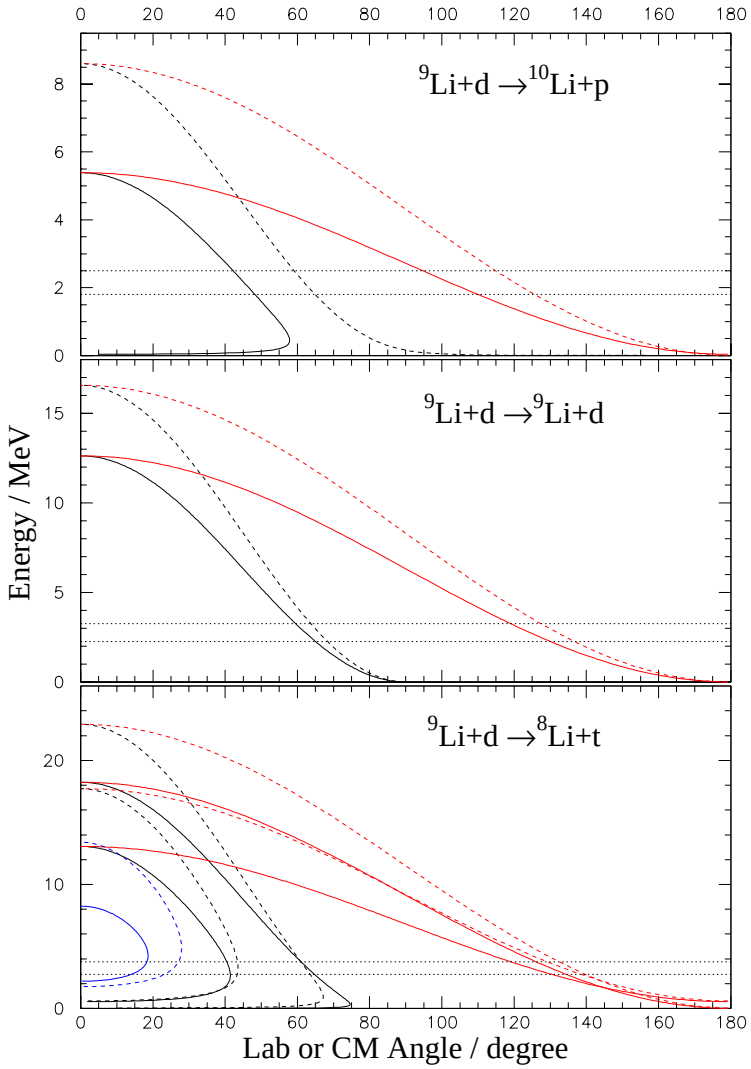

FIGURE 7.1: Simulations of effect of higher REX-ISOLDE beam energy (2.36 MeV/u to 3.1 MeV/u). Solid lines are for 2.36 MeV and dashed lines are for 3.1 MeV/u. Black are for laboratory angles and red are CM angles.

figure 7.1 show the same general trends for the tritons (simulation of ground state and 3rd excited for simplicity). Interestingly the 4th excited state in ^{8}Li at 5.4 MeV (shown in solid blue for 2.36 MeV/u and in dashed blue for 3.1 MeV/u in laboratory angles only) will be observable at the higher REX-ISOLDE energy.

This would also help to clarify the question on a second 2^+ states in ^{8}Li around 4 MeV.

The general feature is that access to higher excitation energy is achived but only limited, if any, enlargement of angular acceptance (CM) is gained. Furthermore it is seen that the curves have steeper slopes which means that an improved angular resolution is needed.

For the transfer experiment on ^{9}Be target the energy upgrade will not play any significant role, since the accessible excitation energy in ^{10}Li is already about 0-7 MeV at 2.36 MeV/u, because the ^{4}He-^{4}He coincidence does not require single particle identification but just two simultaneous events.

In the resonant elastic scattering case a beam energy of 3.1 MeV/u could introduce difficulties, since the first excited state in ^{9}Li situated at 2.69 MeV/u, could be excited (E_{CM}=2.79 MeV/u). From simulations it can, however, be shown that if excitation of the first excited state in ^{9}Li would occur, the scattered proton would not have enough energy to be identified in the DSSSD telescope (max energy 1 MeV). The target thickness for the 3.1 MeV/u case would have to be increased to 180 μm, to be able to stop the beam.

A higher beam energy might also help the interpretation of the transfer data since less compound contribution is expected at higher beam energy.

7.3 Improvement of the setup

An obvious improvement of the setup would be to develop thinner DSSSD (eg 40 μm), although it would not change the experiment significantly, as shown in figure 7.1. Other methods for low energy particle identification could also be developed, such as time-of-flight methods, but at the present time it is not feasible at REX-ISOLDE.

The best possibility to achieve an improved angular resolution would be to obtain DSSSDs with 32$\times$32 strips (still 5$\times$5 cm active area), but at the present time we do not posses such detectors. They are however avaliable from Micron Semiconductors, down to 65 μm thickness.

The easy way to get an improved angular resolution is simply to move the detector further away from the reaction target, thus creating a smaller solid angle for each pixel. In the setup used for the transfer experiments the DSSSD telescope was situated 40.5 mm from the target, covering 18-80°. In figure 7.2 is shown the fit to the experimental ^{8}Li excitation energy spectrum (from figure 5.19), and a simulation where the DSSSD telescope is 81 mm away from the reaction target, covering from 13-43°. The fit and simulation are shown in solid and dashed line, respectivly. The discrepancy at high energy is due to the cover-

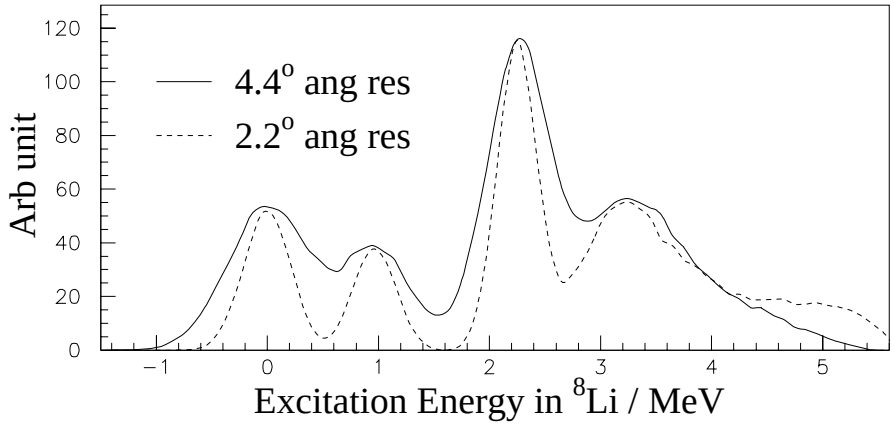

FIGURE 7.2: Simulation of the effect of angular resolution on ^{8}Li excitation energy spectrum. Solid line is with 4.4° resolution and dashed is with 2.2° resolution.

age of smaller scattering angles in the simulation. In the figure it is seen that the overall resolution in excitation energy is greatly improved when enhancing the angular resolution, which was also what one should expect since the excitation energy depends very much on the scattering angle (see eg total energy vs laboratory angle for experimental data in chapter 5). It seems therefore profitable to move the DSSSD telescope further away to enhance the angular resolution although this will of course also decrease the total solid angle. If the same solid angle is required, when doubling the distance between target and detector, four detectors are needed, which in total requires 128 electronic channels. Therefore it could be valuable if 32×32 strip detectors could be purchased, since they would only use 64 electronic channels for the same angular resolution and solid angle.

For the resonant elastic scattering it would also be interesting to see how the beam energy upgrade and an improved angular resolution will change the experimental resolution. In figure 7.3 simulations of the 3.546 MeV state in ^{13}N (Γ=0.047 MeV), which was observed in the ^{12}C+^{1}H reaction (see figure 6.6), are shown. The black line is for 2.21 MeV/u and an angular resolution of 3.4° (same as in experiment with 52.6 mm to the DSSSD), whereas the red is for the same angular resolution but with higher beam energy 3.1 MeV/u (again the target thickness is changed to 180 μm). The black and red line shown no significant difference (σ=34 and 35 keV for the black and red, respectively) between the two beam energies. It might be noted that the width of black peak is in very good agreement with the experimental data in figure 6.6. The blue line in figure 7.3 is

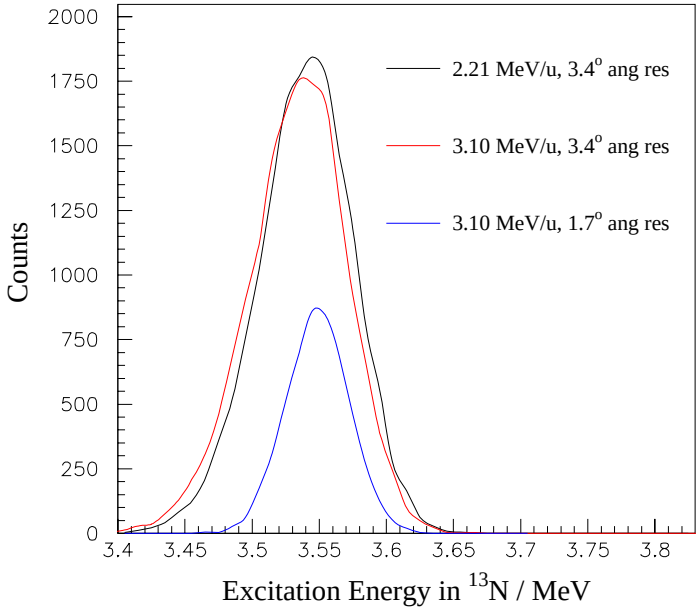

FIGURE 7.3: Simulation of effect of beam energy upgrade and angular resolution on ^{13}N excitation energy spectrum. See figure for specifications.

a simulation of the same state with 1.7° angular resolution, achived by moving the DSSSD telescope from 52.6 mm to 105.2 mm. From the figure it is seen that the energy resolution is improved (σ=24 keV) when increasing the angular resolution, but that the number of counts detected is reduced by a factor of 1/3.

Interestingly, it can be shown that the improved resolution, which at first glance arises from the improved angular resolution, originate almost solely from the fact that the angular acceptance is reduced when moving the DSSSD further away from the reaction target. Figure 7.4 illustrates this fact, where the simulation of a 3.1 MeV/u ^{12}C beam with 3.4° angular resolution (red curve in figure 7.3) is shown for all events (black curve) and for events hitting the DSSSD only in the area which correspond to the solid angle of a DSSSD at 105.2 mm (red curve). It is seen that the peak of the restricted data (laboratory angles less than $\sim 15°$) is almost as narrow as the simulation of 1.7° angular resolution (σ=27 and 24 keV, respectivly). Thus, moving the DSSSD in the resonant elastic scattering experiment will not improve the data significantly, but instead eliminates the possibility for simultaneously having data with less resolution but 3 times better statistics.

It is also relevant to investigate what consequences a thicker target has on

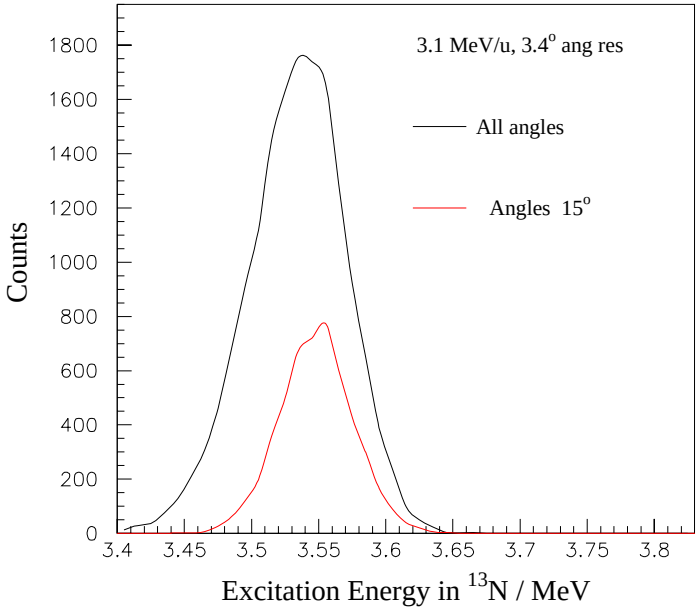

FIGURE 7.4: Simulation showing the effect restrictions on the angular acceptance. Black line is events with no restriction, red line is events within 1/4 of the total solid angle (see text).

the energy resolution for transfer reactions, since a thicker target has the obvious advantage of increasing the yield.

Figure 7.5 shows the effect of varying the target thicknes on the energy resolution of the ^{8}Li excitation energy (only second excited state for simplicity). The simulation is based on a 3.1 MeV/u ^{9}Li beam and 2.2° angular resolution of the detector. In the figure three target thicknesses have been simulated; 5 μm, 15 μm and 25 μm, which give experimental resolutions (σ) of 219, 240 and 283 keV, respectively, for the second excited state in ^{8}Li. So only a 10% increase in the width is expected if a 15 μm target is used instead of a 5 μm target (the one used in the transfer experiment was 6.3 μm), whereas a 30% increase is seen if a 25 μm target is chosen, thus it seem resonable to use a CD target around 15 μm for the upcoming experiment.

7.4 Conclusion

The first conclusion would be that all experiments would benefit greatly from the higher REX-ISOLDE beam energy, except the ^{9}Li on ^{9}Be target which would

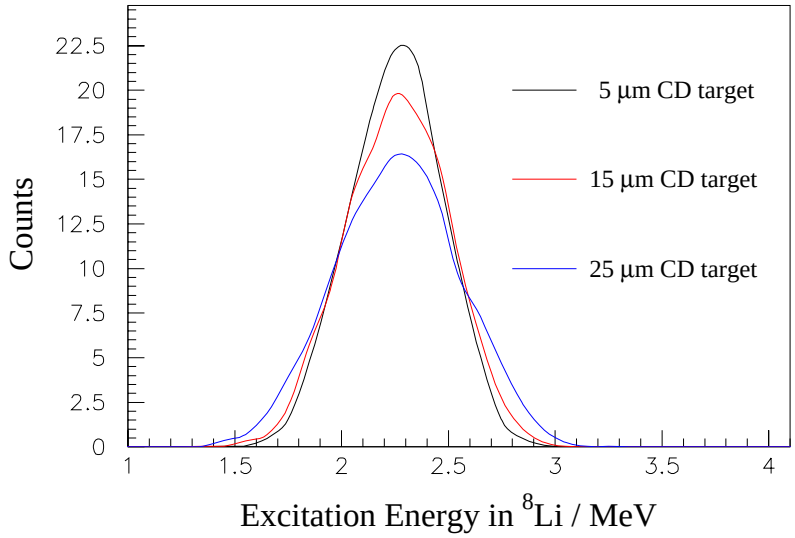

FIGURE 7.5: Simulation of the influence of the target thickness on energy resolution. All simulations are on 3.1 MeV/u ^{9}Li beam and 2.2° angular resolution.

not be affected very much. It is also clear that a thinner DSSSD telescope would be appreciated, although it would not change the quality of the data significantly. Concerning the angular resolution the best choice would be a 32×32 strip DSSSD of same active area as the old 16×16 strip DSSSDs. Unfortunately we do not posses such a detector at the present time.

Transfer reactions: Here it would be very useful to enhance the angular resolution from $\sim 4^{\circ}$ to about $\sim 2^{\circ}$. This would most likely be done by doubling the distance from the reaction target to the DSSSD telsecope from 40 mm to 80 mm. Further it seems resonable to use a thicker CD target (up to 15 μm) since the resolution is only changed slightly (σ grows with $\sim$ 10%). Concerning the CD target, a higher deuterium purity and a more homogeneous target would also be very appreciated.

Elastic resonance scattering: Here the beam energy upgrade would also be a benefit since protons exciting ^{9}Li to its first excited state (2.69 MeV), which can just be excited when using 3.1 MeV/u, will not penetrate the DSSSD telescope and will therefore not complicate the data. Concerning the angular resolution there is no reason for an enhancement (if it implies moving the detectores further away), since almost the same improvement in experimental excitation energy resolution can be gained by requiring the protons to have a smaller laboratory scattering angle.

CHAPTER 8

Summary and conclusion

In this chapter I will summarize and conclude my work on low energy reactions with the radioactive nucleus ^{9}Li.

8.1 Summary

In this thesis three reaction experiment, performed at the newly constructed REX-ISOLDE post-accelerator at ISOLDE/CERN, have been described and analysed. All the experiments described were performed with the radioactive isotope ^{9}Li ($t_{1/2}$=178.3 ms) at energies just over 2 MeV/u. The aim of all three experiments was to extract spectroscopic information on the particle unbound nucleus ^{10}Li.

Much of my work during the last two years have been aimed at getting acquainted with the new instrument, REX-ISOLDE, and the type of data which it produces. It has been very rewarding to work with this new instrument, since everything have had to be done all from the beginning.

The first two experiments were transfer reactions where a neutron was transfered to ^{9}Li, thus directly forming ^{10}Li, whereas the third was a resonant elastic scattering experiment where the isobar analogue states of ^{10}Li in ^{10}Be were probed. For the transfer experiments a small telescope and a single DSSSD telescope was used which covered laboratory angles from 18-80 $^{\circ}$. In the elastic scattering experiment three DSSSD telescopes was applied, one centered and one on each side of the beam direction. In total the three telescopes covered almost all laboratory angles from roughly -70 $^{\circ}$ to 70 $^{\circ}$.

The first of the transfer experiments was the ^{9}Li+^{2}H reaction, designed to transfer an s-wave neutron to ^{9}Li. The reaction was performed with a 2.36 MeV/u ^{9}Li beam incident on a 6.4 μm deuterated polypropylene target with only a few percent ^{1}H contamination. The reaction products emitted in this reaction contained both protons, deuterons, tritons, ^{4}He and ^{6}He. The proton channel attracted the main attention since this is the channel probing ^{10}Li. In the data a peak was observed 350 keV over the ^{9}Li+n threshold with a width of roughly 300 keV, in agreement with the first excited state in ^{10}Li. The differential cross-section for this state has been extracted (CM angles from 45-85°). The deuteron channel was primarily used to normalize the amount of ^{9}Li incident on target during the entire experiment via optical model calculations of the elastic cross-section relative to Rutherford cross-section. The number of ^{9}Li was found to be 1.8×10^{9}, corresponding to 7×10^{4} per 2.4 s (the time between production of ^{9}Li). From the triton channel a very beautiful excitation energy spectrum for ^{8}Li was extracted, showing all experimentally known states below 4 MeV. Here differential cross-sections were also extracted for all four states, further they were compared with optical model calculations. The two helium channels proved less interesting since all channels end up in a 3-body or 5-body final state, which complicates the analysis considerably. It was nevertheless shown, via coinci-

dences, that most events ends in a 5-body channel before detection, that is two ^{4}He nuclei and three neutrons.

The second transfer experiment was ^{9}Li incident on a 5.2 μm ^{9}Be target, where the intention was to transfer p-wave neutrons to the ^{9}Li beam. Again a 2.36 MeV/u ^{9}Li beam was used. Also in this experiment protons, deuterons, tritons, ^{4}He and ^{6}He was emitted from the reaction. None of these fragments seemed, in a rough analysis, to hold much information. It turned out that the information was in the ^{4}He coincidences, both between the *small telescope* and the DSSSD and between double hits in the DSSSD. It was found that the break-up of ^{8}Be, after neutron pick-up from ^{9}Be, could proceed via either the 0^{+} ground state or 2^{+} first excited state in ^{8}Be, and that these two channels could be separated. Gating on one of the channels the excitation energy in ^{9}Li+n could be extracted, but due to very low statistics and limited angular resolution no interesting information could be extracted.

The resonant elastic scattering experiment of ^{9}Li on ^{1}H was performed by stopping the beam in a 105 μm polyethylene target, thus scanning the resonance energy while the beam was stopped in the target. Furthermore, in this beam time a test experiment was performed with a ^{12}C beam in order to have data where known resonances were present. This data was in good agreement with literature, and showed that the setup/method was functioning. For the ^{9}Li case reasonable data was collected which, after a preliminary analysis, indicated three states in ^{10}Be at 20.75$\pm$0.06 MeV, 20.98$\pm$0.01 MeV and 21.148$\pm$0.009 MeV. The tentative interpretation is, that the first state corresponds to a known state at 20.8$\pm$0.1 MeV in ^{10}Be, whereas the two other states are analogues to states in ^{10}Li. If this interpretation is correct the analogue states in ^{10}Li are situated at -0.08$\pm$0.1 MeV and 0.36$\pm$0.1 MeV, if the Coulomb displacement energy is calculated by a parametrization [Ant97]. A triton branch is also present from the ^{9}Li+^{1}H reaction which could also contain information about ^{10}Li, but it has so far not been analysed.

8.2 Conclusion

It has been shown that the two nucleon transfer experiments are functioning and that preliminary data from both show promising results. The primary goal of extracting knowledge on ^{10}Li, is well under way (the present data are not conclusive). Furthermore the triton channel, from the ^{9}Li+^{2}H reaction, has also shown to be very interesting, due to inconsistencies between experimental data and theoretical predictions.

The analysis of the ^{9}Li+^{9}Be reaction has shown that the one-neutron pick-up

reaction does occur, and that it should be possible to extract information on ^{10}Li in this way. Although it should be noted that the reaction yield from this reaction was low, which might be due to a limited acceptance for coincidence data in the used setup.

The data from the resonant elastic scattering experiment, which was very short due to technical problems, has shown that this type of experiment can be performed at REX-ISOLDE when using thick solid targets. In the test case, ^{12}C+^{1}H, very nice data was collected showing that an overall resolution of about 30 keV (σ) could be achieved. In the ^{9}Li+^{1}H case the data have only been analysed preliminarily, but indicate that this way of gaining knowledge on exotic nuclei is very promising. Furthermore the comparison between data and simulations showed that we could describe the Rutherford background very well.

All the experiences collected on low energy reactions at REX-ISOLDE should also be mentioned, since they are also very relevant and valuable for the collaboration. The work with radioactive beams has proved to be more delicate than expected, since beam intensities have not been as high as expected and because relatively large contaminant beams were present. In all experiments the ^{9}Li intensity has been a few times 10^4/s which is very low compared to stable beam experiments. Furthermore, our first attempt to perform transfer reactions with ^{9}Li turned out to be impossible due to a $^{12}C^{4+}$ contamination of about 10^6/s (in this first test we were running with $^{9}Li^{3+}$). This taught us to run with $^{9}Li^{2+}$, which has $^{18}O^{4+}$ as a contaminant beam. This could be tolerated, since the ^{18}O beam had an intensity less than 10^4/s.

In general it should always be considered which contaminant beams might be accelerated for different charge states of the wanted nucleus. Future developments to improve the beam purity could be very interesting and necessary in some cases. Especially if helium isotopes are to be accelerated, which will always have ^{12}C contamination. With the fact, that all contaminant beams are stable, in mind it seems clear that clean beams of light proton rich nuclei should be easier to produce without background, since stable nuclei cannot be produced with the same high charge states.

This work has also shown that the ”old” methods of DWBA must be revived, since it is the best way to describe transfer reactions at low energy. It still remains to be clarified whether the old descriptions are adequate or new ones are needed, to be able to describe the more dilute structure of loosely bound nuclei. Progress on this subject is presently undergoing in collaboration with A.M. Moro and J. Gómez-Camacho from Sevilla.

APPENDIX A

Simulations

In this appendix I will describe the general concept in our simulations which are used extensively to interpret our data.

A.1 Introduction

In most case simulations are the basis of our analysis, and are crucial for understanding detector acceptance and cut-offs when such complicated detectors as DSSSDs are employed. In the case of a simple gas-telescope simulations are normally not needed, since most threshold behaviors can be understood analytically. But, as mentioned, in the case where a DSSSD (or several DSSSDs) are used in a setup it can prove invaluable to have the ability to simulate which kinematic properties, cut-offs and acceptances specific particles would have when proceeding via specific channels.

A.2 The basic simulation concept

I will in this section try to shortly describe the ideas and concepts that we use in our simulations. In the following I will use binary reactions as the example, since this is what have been used in most cases. In the few simulations performed with more than two particles in the final state sequential models have been applied, ie first a binary reaction followed by the break-up of one or both of the particles.

The general concept in our simulations is that we first simulate the physical events based on pure kinematics, that is we simulate the energy and angle of one of the involved particles and calculate energy and angle for the other particle in the CM frame. Then a transformation to the laboratory system is performed. In the laboratory system different energy-losses are calculated, such as energy-loss in the target, where a random reaction position normally is applied (for thin targets), and energy-loss in the deadlayer of the detector(s). The different angles at which the particle passes through the target and deadlayer are found by simple rotations from the known positions of the target and detector(s). All energy-losses are calculated based on tables of ion ranges at different ion energies calculated with SRIM 2003 [SRIM]. Then a simulation of the detection and data acquisition is performed by calculating where the particle would hit a given detector and subsequently transforming the energy of the particle into the channel number which correspond to this energy in the data acquisition. This is done by using the detector calibration backwards and adding the experimental resolution via a simulated uncertainty. This data, which now is as our data acquisition would see it, is now put into n-tuples exactly as the real data. Now the n-tuples can be processed as the real data files and the same histogram files containing all the histograms are created. With these sets of simulated and real histograms a comparison between theory and data can easily be performed. A diagram sketching the basic concepts in our simulations is shown in figure A.1.

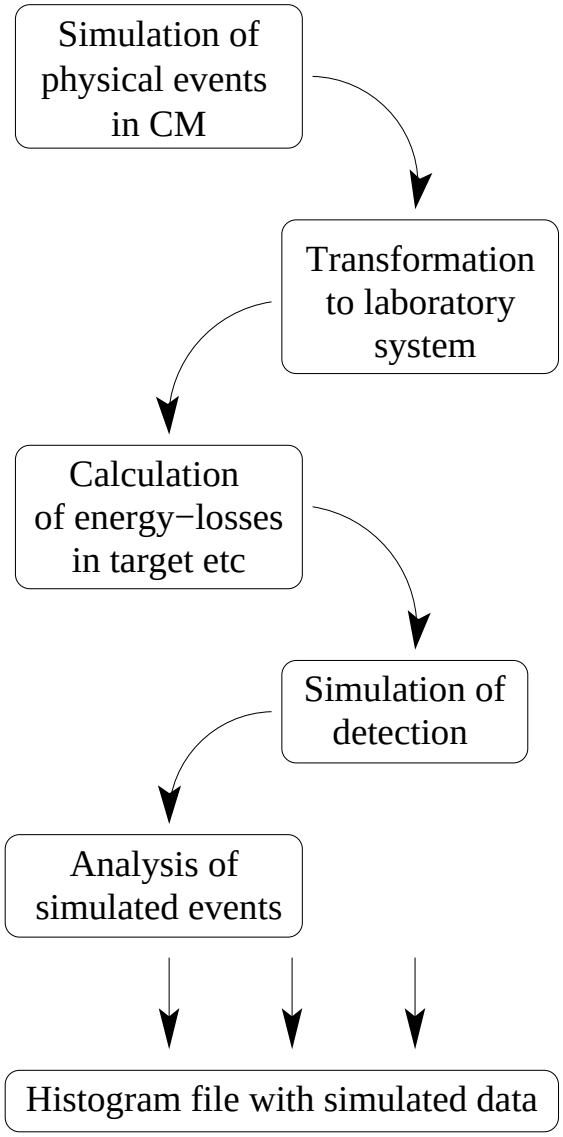

FIGURE A.1: Diagram showing the concept of our simulations. See text for details.

With this type of simulation it is very easy to include specific angluar distributions and energy dependencies, since such effects simply have to be applied in the first stage of the simulation (the physics part). Further simulations of improved setups are also easily feasible since one just have to change the position or specifications of the detector(s). As a final bonus the simulation, due to knowledge of the detector position and design, also returns the acceptance and cut-offs of the detector setup. Of course this requires an exhaustive knowledge of the detector(s), eg one needs to know experimental resolution, thresholds etc to be able to performe precise simulations.

Acknowledgement

First of all I would like to extend my gratitude to my supervisor Karsten Riisager, who has always been supportive throughout my years as a PhD here in Århus, both professional and personal. Especially I would like to acknowledge his enormous knowledge in all fields of physics and his ability to always extract the critical information/parameter in a physics debate - although it has some times annoyed me that he always knows everything ☺ .

I would also like to thank Uffe Bergmann and Hans Fynbo very much for helping me with PAW, Fortran, showing me around CERN and for many nice hours drinking beers. Especially I would like to thank Hans for proof-reading my thesis and his everlasting tolerence these last two years where we have been sharing office - I hope that you enjoyed it to! On top of this I would also thank Hans for good company on all the interesting trips around the world.

Our collaboration should also receive a great applause from me for recieving me so openly in the group and always showing interest in my work. It have always been plesant meeting you all, Björn, Göran, Thomas, Maria, Olof, Luis and many others, at experiments, conferences and meetings. Especilly I would like to thank Olof Tengblad for trying to teach me about electronics and data acquisition and many interesting evening hours at CERN.

I would like to thank Isao Tanihata for inviting me to RIKEN in Tokyo in the autumn of 2002. During the stay Rituparna Kanungo was my supervisor, and I would like to express my appreciation for her time and many explanations about RIKEN and reactions at intermediate energies.

During my many years her at the University of Aarhus I have meet many people who has changed and coloured my life and made these 8 years the very best - so far. Specially I would like to thank Jacob and Allan for many nice hours, and *one single beer*, at Hejredals Kollegiet and later on. Further a big thank to the people from Fysikshow for loads of inspiration and fun, especially

Klaus, Janus, Mikkel and lille Lars. Finally I would like to thank Kristian for proof-reading my thesis, many good hikes and general good friendship.

A thank also go out to my mathematics and physics teacher from elemantary school, Flemming Olesen, who has been one of the inspirations in my early years, which lead my to become a scientist.

Furthermore I[1] would like to thank Jytte for supplying the office with a television for the hard working days during Tour de France ♡. Thanks honey for always being there for me - love you (both).

Finally I would like to thank my parents, Hanne and Poul, for always supporting me and letting me do things my own way.

[1] Both Hans and I were very happy about this.

Bibliography

[Abr79] S.M. Abramovich, B.Ya. Guzhovskiĭ, A.G. Zvenigorodskiĭ and S.V. Trusillo, *Near-threshold anomaly in the reaction* $^{7}Li(t,^{9}Li)^{1}H$, Sov. J. Nucl. Phys. **30** (1979) 665.

[Ajz88] F. Ajzenberg-Selove, *Energy levels of light nuclei A=5-10*, Nucl. Phys. **A490** (1988) 1.

[Ajz91] F. Ajzenberg-Selove, *Energy levels of light nuclei A=13*, Nucl. Phys. **A523** (1991) 1.

[Ame90] A.I. Amelin *et al*, *Production of* ^{10}Li *in absorption of stopped* π^- *mesons by* ^{11}B *nuclei*, Sov. J. Nucl. Phys. **52** (1990) 782.

[Ant97] M.S. Antony, A. Pape and J. Britz, *Coulomb displacement energies between analog levels for* $3 \leq A \leq 239$, Atomic Data and Nuclear Data Tables **66** (1997) 1.

[Aud03] G. Audi, O. Bersillon, J. Blachot and A.H. Wapstra, *The NUBASE evaluation of nuclear and decay properties*, Nucl. Phys. **A729** (2003) 3.

[Ber00] U.C. Bergmann, *Exotic decays of nuclei at the limits of existence*, PhD thesis, University of Aarhus (2000) unpublished (www.phys.au.dk/ ucb/papers/thesis.gz).

[Ber03a] U.C. Bergmann *et al*, *Beta-decay properties of the neutron-rich* $^{94-99}Kr$ *and* $^{142-147}Xe$ *isotopes*, Nucl Phys. **A714** (2003) 21.

[Ber03b] U.C. Bergmann, H.O.U. Fynbo and O. Tengblad, *Use of Si strip detectors for low-energy particle in compact geometry*, Nucl. Inst. Meth. **B515** (2003) 657.

[Bet99] H.A. Bethe, *Nuclear Physics*, Rev. Mod. Phys. **71** (1999) S6.

[Bey00] G.J. Beyer, *Radioactive ion beams for biomedical research and nuclear medical application*, Hyp. Int. **129** (2000) 529.

[Boh36] N. Bohr, *Neutron capture and nuclear constitution*, Nature **137** (1936) 344.

[Boh37] N. Bohr and F. Kalckar, *On the transmutation of atomic nuclei by impact of material particles*, K. Dan. Vid. Sel. mat.-fys. Medd. **14** iss. 10 (1937) 1.

[Boh69] Aa. Bohr and B.R. Mottelson, *Nuclear structure I*, W.A. Benjamin, New York (1969).

[Boh99] H.G. Bohlen *et al*, *Spectroscopy of exotic nuclei with multi-nucleon transfer reactions*, Prog. Part. Nucl. Phys. **42** (1999) 17.

[Bre36] G. Breit and E. Wigner, *Capture of slow neutrons*, Phys. Rev. **49** (1936) 519.

[Bra83] B.H. Bransden and C.J. Joachain, *Physics of atoms and molecules*, Longman, Malaysia (1983).

[But50] S.T. Butler, *On angular distributions from (d,p) and (n,p) nuclear reactions*, Phys. Rev. **80** (1950) 1095.

[But58] S.T. Butler, N. Austern and C. Pearson, *Semiclassical treatment of direct nuclear reactions*, Phys. Rev. **112** (1958) 1227.

[Cag99] J.A. Caggiano *et al*, *Spectroscopy of the* ^{10}*Li nucleus*, Phys. Rev. **C60** (1999) 064322.

[Cau04] E. Caurier *et al*, *The shell model as unified view of nuclear structure*, arXiv: nucl-th/0402046.

[Coh65] S. Cohen and D. Kurath, *Effective interactions for the 1p shell*, Nucl. Phys. **73** (1965) 1.

[Coh67] S. Cohen and D. Kurath, *Spectroscopic factors for the 1p shell*, Nucl. Phys. **A101** (1967) 1.

[Ehr51] J.B. Ehrman, *On the displacement of corresponding energy levels of* ^{13}*C and* ^{13}*N*, Phys. Rev. **81** (1951) 412.

[Eur03] *The Eurisol report*, Ganil, Caen, France (2003) or http://www.ganil.fr/eurisol/Final_Report.html.

[Fed00] V.N. Fedoseyev *et al The ISOLDE laser ion source for exotic nuclei*, Hyp. Int. **127** (2000) 409.

[Fyn03] H.O.U. Fynbo *et al*, *Clarification of the threebody decay of* ^{12}*C(12.71 MeV)*, Phys. Rev. **91** (2003) 82502-1.

[Gar02] E. Garrido, D.V. Fedorov and A.S. Jensen, *The* ^{10}*Li spectrum and the* ^{11}*Li properties*, Nucl. Phys. **A700** (2002) 117.

[Gei95] H. Geissel, G. Münzenberg and K. Riisager, *Secondary exotic nuclear beams*, Annu. Rev. Part. Sci. **45** (1995) 163.

[Gol51] G. Goldhaber and R.M. Williamson, *Elastically scattered protons from carbon*, Phys. Rev. **82** (1951) 495.

[Gun01] C. Gund *et al*, *Potential and limitations of nucleon transfer experiments with radioactive beams at REX-ISOLDE*, Eur. Phys. J. **A10** (2001) 85.

[Gur98] A.F. Gurbich, *Evaluation of non-Rutherford proton elastic scattering cross section for carbon*, Nucl. Inst. Meth. **B136** (1998) 136.

[Guz90] B.Ya. Guzhovskiĭ and L.M. Lazarev, Bull. Acad. Sci. USSR, Phys. Ser. **54** (1990) 156.

[Hab00] D. Habs *et al*, *The REX-ISOLDE project*, Hyp. Int. **129** (2000) 43.

[Han87] P.G. Hansen and B. Jonson, *The neutron halo of extreme neutron-rich nuclei*, Eur. Phys. Lett. **4** (1987) 409.

[Hax49] O. Haxel, J.H.D. Jensen and H.E. Suess, *On the "magic numbers" in nuclear structure*, Phys. Rev. **75** (1949) 1766.

[Hey94] K. Heyde, *Basic ideas and concepts in nuclear physics*, Institute of Physics Publishing, London (1994).

[Hod71] P.E. Hodgson, *Nuclear reactions and nuclear structure*, Clarendon Press (1971) Oxford.

[Hod97] P.E. Hodgeson, E. Gadioli and E. Gadioli Erba, *Introductory nuclear physics*, Clarendon Press (1997) Oxford.

[IS367] http://doc.cern.ch/tmp/convert_SC00000914.pdf

[IS371] http://doc.cern.ch/tmp/convert_sc00000991.pdf

[ISOLDE] http://isolde.web.cern.ch/ISOLDE/

[ITER] http://www.iter.org

[Jep02] H. Jeppesen *et al*, *Search for beta-delayed charged particles from the halo nuclei* ^{14}Be, Nucl. Phys. **A709** (2002) 119.

[Jep04] H. Jeppesen *et al*, *One- and two-proton removal from* ^{15}O, Nucl. Phys **A739** (2004) 57.

[Jon96] B. Jonson and G. Nyman, *Beta-delayed particle emission*, in *Nuclear decay modes*, ed. D.N. Poenaru, IOP publishing (1996) 102.

[Jon00] B. Jonson and A. Richter, *More than three decades of ISOLDE physics*, Hyp. Int. **129** (2000) 1.

[Jon01] B. Jonson and K. Riisager, *Beta-decay of exotic nuclei*, Nucl. Phys. **A693** (2001) 77.

[Jon04] B. Jonson, *Light dripline nuclei*, Phys. Rep. **389** (2004) 1.

[Kan02] R. Kanungo, I. Tanihata and A. Ozawa, *Observation of new neutron and proton magic numbers*, Phys. Lett. **B528** (2002) 58.

[Kes03] O. Kester *et al*, *Accelerated radioactive beams from REX-ISOLDE*, Nucl. Inst. Meth. **B204** (2003) 20.

[Kof51] O. Kofoed-Hansen and K.O. Nielsen, *Measurements on shortlived radioactive krypton isotopes from fission after isotope separation*, Kgl. Dan. Vid. Sel. Mat.-Fys. Medd. **26** no. 7 (1951) 1.

[Kra88] K.S. Krane, *Introductory Nuclear Physics*, John Wiley & Sons, New York (1988).

[Kra00] G. Kraft, *Tumor therapy with heavy charged ions*, Prog. Part. Nucl. Phys. **45** (2000) 473.

[Kry93] R.A. Kryger *et al*, *Neutron decay of* ^{10}Li *produced by fragmentation*, Phys. Rev. **C47** (1993) R2439.

[Kug92] E. Kugler *et al*, *The new CERN-ISOLDE on-line mass-separator facility at the PS-Booster*, Nucl. Inst. Met. **B70** (1992) 41.

[Kug00] E. Kugler, *The ISOLDE facility*, Hyp. Int. **129** (2000) 23.

[Kur04] D. Kurath, (private communication via A. Richter).

[Lan58] A.M. Lane and R.G. Thomas, *R-matrix theory of nuclear reactions*, Rev. Mod. Phys. **30** (1958) 257.

[Len98] H. Lenske and G. Schrider, *Probing the structure of exotic nuclei by transfer reactions*, Eur. Phys. **A2** (1998) 41.

[Let97] J. Lettry *et al*, *Pulse shape of the ISOLDE radioactive ion beam*, Nucl. Inst. Meth. **B126** (1997) 130.

[May49] M.G. Mayer, *On closed shells in nuclei. II*, Phys. Rev. **75** (1949) 1969.

[May55] M.G. Mayer and J.H.D. Jensen, *Elementary theory of nuclear shell structure*, John Wiley & Sons, New York (1955).

[May63] M.G. Mayer, *The shell model*, Nobel lectures Physics 1963-1970, Elsevier, Amsterdam (1972) 20 or http://www.nobel.se/physics/laureates/1963/mayer-lecture.pdf.

[McV94] K.W. McVoy and P. van Isacker, *Does the ground-state resonance of ^{10}Li overlap neutron threshold?*, Nucl. Phys. **A576** (1994) 157.

[Mei02] M. Meister *et al*, *Evidence of new low-lying resonance state in ^{7}He*, Phys. Rev. Lett. **88** (2002) 102501.

[Mit76] J.B. Mitchell, S. Agami and J.A. Davies, *The use of Si surface barrier detectors for energy calibrations of MeV ion accelerators*, Rad. Eff. **28** (1976) 133.

[Mor04] A.M. Moro and J. Gómez-Camacho, (private comunication).

[Nel02] R.O. Nelson and A. Michaudon, Nucl. Sci. Eng. **140** (2002) 195.

[Nil00] T. Nilsson, G. Nyman and K. Riisager, *Halo-nuclei at ISOLDE*, Hyp. Int. **129** (2000) 67.

[NuP02] NuPECC report, *Nuclear science in Europe: Impact, Application, Interaction*, (2002).

[Oga04] Y.T. Oganessian *et al*, *Experiments on the synthesis of element 115 in the reaction ^{243}Am(^{48}Ca,xn)$^{291-x}$115*, Phys. Rev. **C69** (2004) 021601.

[Oza01] A. Ozawa, T. Suzuki and I. Tanihata, *Nuclear size and related topics*, Nucl. Phys. **A693** (2001) 32.

[Pie01] S.C. Piepers and R.B. Wiringa, *Quantum monte carlo calculations of light nuclei*, Annu. Rev. Nucl. Part. Sci. **51** (2001) 53.

[Pie02] S.C. Piepers, K. Varga and R.B. Wiringa, *Quantum monte carlo calculations of A=9,10 nuclei*, Phys. Rev. **C66** (2002) 044310.

[Pod02] H. Podlech, R. von Hahn, R. Repnow and D. Schwalm, *The 7-gap resonator accelerator for the REX-ISOLDE project at CERN*, Nucl. Phys. **A701** (2002) 651c.

[Pow70] D.L. Powell, G.M. Crawley, B.V.N. Rao and B.A. Robson, *Deuteron-induced reactions in ^{6}Li, ^{9}Be and ^{10}B at bombarding energies of 4.5 to 6.0 MeV*, Nucl. Phys. **A147** (1970) 65.

[REXweb] http://www.ha.physik.uni-muenchen.de/okester/rex/rex.html and http://fy.chalmers.se/subatom/f2bfw/rexposter.html.

[Sal93] R. Salomonovič, *Angular distribution of proton non-Rutherford elastic scattering cross section of carbon and silicon*, Nucl. Inst. Meth. **B82** (1993) 1.

[San03] P. Santi *et al*, *Structure of the ^{10}Li nucleus investigated via the ^{9}Li(d,p)^{10}Li reaction*, Phys. Rev. **C67** (2003) 024606.

[Sat83] G.R. Satchler, *Direct nuclear reactions*, Clarendon press (1983) Oxford.

[Sat90] G.R. Satchler, *Introduction to nuclear reactions*, Macmillan Education LTD, second ed. (1990).

[Sch02] P. Schmidt *et al*, *Bunching and cooling of radioactive ions with REX-TRAP*, Nucl. Phys. **A701** (2002) 550c.

[Sie87] P.J. Siemens and A.S. Jensen, *Elements of nuclei*, Addison Wesley (1987).

[Sie02] T. Sieber *et al*, *Design and status of the front end part of the REX-ISOLDE linac*, Nucl. Phys. **A701** (2002) 656c.

[SRIM] http:/www.srim.org (where the program can be downloaded).

[Ste79] E.J. Stephenson, B.P. Hichwa and J.D. Hutton, *Compound nucleus contribution to the ^{18}O(d,p)^{19}O reaction*, Nucl. Phys. **A331** (1979) 269.

[Szc89] A. Szczurek *et al*, *Mechanism of reactions induced by 7 MeV deuterons on ^{9}Be [(d,p),(d,d),(d,t),(d,^{4}He)]*, Z. Phys. **A333** (1989) 271.

[Tan85a] I. Tanihata *et al*, *Measurements of interaction cross sections and radii of He isotopes*, Phys. Lett. **B160** (1985) 380.

[Tan85b] I. Tanihata *et al*, *Measurements of interaction cross sections and nuclear radii in the light p-shell region*, Phys. Rev. Lett. **55** (1985) 2676.

[Ten04] O. Tengblad *et al*, *Novel thin window design for a large area Silicon strip detector*¸ Nucl. Inst. Meth. **A525** (2004) 458.

[Tho50] R.G. Thomas, *Excited states of ^{13}N and ^{13}C*, Phys. Rev. **80** (1950) 136.

[Tho99] M. Thoennessen *et al*, *Population of ^{10}Li by fragmentation*, Phys. Rev. **C59** (1999) 111.

[Til03] D.R. Tilley *et al*, *Energy levels of light nuclei A=10*, Preliminary version available from the web:
http://www.tunl.duke.edu/nucldata/publications.shtml

[Wen01] F. Wenander *et al*, *REXEBIS, design and initial commissioning results*, AIP Conf. Proc. **572** (2001) 59.

[Wic63] G. Wickenberg, S. Hjorth, N.G.E. Johansson and B. Sjögren, *Proton angular distributions from $^{18}O(d,p)^{19}O$ at E_d=7.0 MeV*, Arkiv för Fysik **25** (1963) 191.

[Wil75] K.H. Wilcox *et al*, *The (^{9}Be,^{8}B) reaction and the unbound nuclide ^{10}Li*, Phys. Lett. 59B (1975) 142.

[Wir00] R.B. Wiringa, S.V. Pieper, J. Carlson and V.R. Panharipande, *Quantum monte carlo calculations of A=8 nuclei*, Phys. Rev. **C62** (2000) 014001.

[Wir04] R.B. Wiringa, (private communication via A. Richter).

[Wmap] http://map.gsfc.nasa.gov/m_mm/mr_firststar.html.

[You94] B.M. Young *et al*, *Low-lying structure of ^{10}Li in the reaction $^{11}B(^{7}Li,^{8}B)^{10}Li$*, Phys. Rev. **C49** (1994) 279.

[Zin95] M. Zinser *et al*, *Study of the unstable nucleus ^{10}Li in stripping reactions of the radioactive projectiles ^{11}Be and ^{11}Li*, Phys. Rev. Lett. **75** (1995) 1719.

[Zin97] M. Zinser *et al*, *Invariant-mass spectroscopy og* ^{10}*Li and* ^{11}*Li*, Nucl. Phys. **A619** (1997) 151.